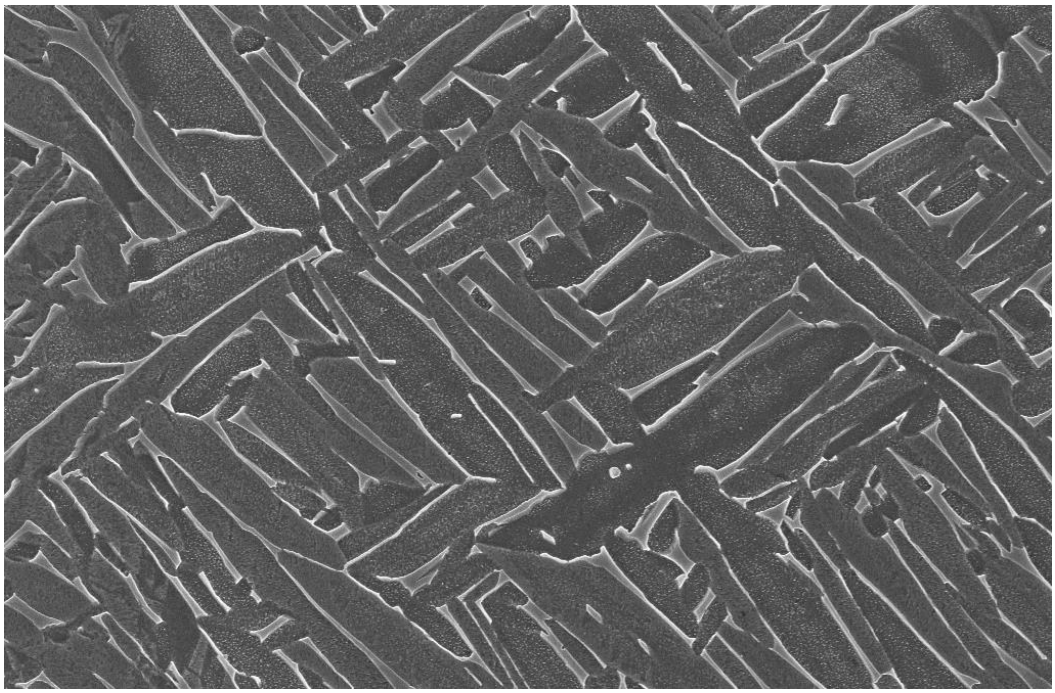


Microstructural changes in LMD-p Ti-6Al-4V: influence of cooling rates during heat treatment

In collaboration with GKN Aerospace AB

Master's thesis in MSc. Materials Engineering

Sachin Subramanian

DEPARTMENT OF INDUSTRIAL AND MATERIAL SCIENCE

CHALMERS UNIVERSITY OF TECHNOLOGY
Gothenburg, Sweden 2021
www.chalmers.se

Microstructural changes in LMD-p Ti-6Al-4V: influence of cooling rates during heat treatment
In collaboration with GKN Aerospace AB
SACHIN SUBRAMANIAN

© SACHIN SUBRAMANIAN, 2021.

Supervisors: Dr. Ceena Joseph, GKN Aerospace AB
Fang Liu, IMS Department, Chalmers University of Technology
Examiner: Fang Liu, IMS Department

Master's Thesis 2021
Industrial and Materials Science
Chalmers University of Technology
SE – 412 96 Gothenburg
Telephone: +46 772 1000

Cover: SEM image of LMD-p Ti-6Al-4V microstructure.

Printed by Chalmers Reproservice
Gothenburg, Sweden 2021

ABSTRACT

Laser Metal Deposition (LMD) is an additive manufacturing technique being developed for several aerospace applications including the repair of aerospace engine components. Mechanical and microstructural properties of LMD Ti-6Al-4V vary from those obtained from conventionally processed routes, with the main influences being the process parameters and post processing heat treatment parameters such as temperature, holding time and cooling rate. This thesis work aimed at understanding the effect of varying the cooling rates during heat treatment on the microstructure of LMD (powder) Ti-6Al-4V.

Local heat treatments were performed, and the resulting microstructures were analysed using Light Optical Microscope (LOM), Scanning Electron Microscope (SEM) and Hardness testing. In order to understand the influence of cooling rates on microstructural changes, key features such as alpha lath thickness, alpha-phase fraction, alpha-case formation and beta grain size were measured and characterized using appropriate image analysis software. The volume fraction of phases after heat treatments were simulated using simulation tools such as ThermoCalc and JMatPro, and a comparison was made between simulation and experimental results.

Cooling rates during heat treatments were found to have no influence on the beta grain size and alpha-case thickness and less influence on the build hardness. Influence of cooling rates on alpha lath thickness and alpha-phase fraction was higher for heat treatments at temperatures close to beta-transus, with an increase in cooling rate leading to decreases in alpha-lath thickness and alpha-phase fraction. Simulation tools predicted trends of cooling rate influence on alpha-phase fraction similar to those experimentally observed but gaps were found between the two in the exact simulated and measured values.

Keywords: Titanium alloys, Ti-6Al-4V, Additive Manufacturing, Laser Metal Deposition, heat treatment, cooling rate, phase transformations, microstructure, hardness, alpha case, alpha phase, beta phase, beta grain size, alpha lath, JMatPro, ThermoCalc.

ACKNOWLEDGEMENTS

I would first like to thank my industrial supervisor Dr. Ceena Joseph for all her support and guidance throughout this thesis work. The time I have spent with her, albeit mostly online, has taught me so much and made me grow both professionally and personally. The takeaways from my many interactions with her will surely serve me well in my future in the field of materials science.

I wish to thank my university supervisor and examiner Fang Liu for her support and guidance throughout and for always being there when needed. I was always left with a feeling of positivity and inspiration after our meetings which kept me ticking.

I wish to also thank my former colleague Iu-Aran Fernández Perucho with whom I have worked closely and collaborated on many occasions during this thesis and wish him the very best in his career as a researcher. The time I spent with him, both during and after work hours, has been nothing less than an absolute pleasure.

Special thanks to Stefan Nordgren and Per-Olof Larsson at the local heat treatment facility at GKN for their support and patience in carrying out all the experiments smoothly.

Thanks also to everyone at GKN from the staff in the materials lab who helped in training me with the equipment usage to former colleagues in the MIT department for the fun 'fika's and lunches.

Special mention to my colleagues at Chalmers' Industrial and Materials Science department for sharing their knowledge on subjects like defect analysis and using the ThermoCalc software. Thanks to Dr. Zhanli Guo from JMatPro and Andreas Markstrom from ThermoCalc for extending support with the respective software usage.

Lastly, to my family and friends for their undying love, support, and care, throughout my master program, which I feel blessed for and cannot thank enough.

TABLE OF CONTENTS

ABSTRACT 3

ACKNOWLEDGEMENTS 4

TABLE OF CONTENTS 5

1 INTRODUCTION 8

1.1 Background 8

1.2 Aim 8

1.3 Scope 8

2 LITERATURE REVIEW 9

2.1 The Aerospace industry 9

2.2 Additive Manufacturing in the Aerospace industry 10

2.2.1 AM in Aerospace engines 10

2.2.2 Materials used in aerospace engines 11

2.3 Titanium and its alloys 12

2.3.1 Titanium extraction 13

2.3.2 Titanium crystal structure 13

2.3.3 Phase transformations in titanium alloys 14

2.3.3.1 Diffusion-less martensitic transformation 14

2.3.3.2 Diffusion-controlled nucleation and growth 14

2.3.4 Titanium alloys 15

2.4 Ti-6Al-4V 16

2.4.1 Ti-6Al-4V phases and microstructure morphologies 17

2.4.2 Ti-6Al-4V oxidation and α-case 18

2.4.3 Ti-6Al-4V applications 18

2.5 Ti-6Al-4V processing and thermal treatments 18

2.5.1 Conventional shaping techniques 18

2.5.2 Additive Manufacturing (AM) 21

2.6 Laser Metal Deposition (LMD) of Ti-6Al-4V 22

2.6.1 Defects in LMD Ti-6Al-4V 23

2.6.2 Thermal history during the LMD process 24

2.6.3 Microstructural features of LMD-p Ti-6Al-4V 25

2.6.4 Mechanical Properties of LMD Ti-6Al-4V 25

2.7 Heat Treatment of LMD-p Ti-6Al-4V 26

2.7.1 Influence of heat treatment temperature and holding time 27

2.7.2 Influence of cooling rate during heat treatment 28

2.8 Simulation tools for heat treatment design 29

2.8.1 JMatPro 29

2.8.2 ThermoCalc 30

3 METHODS 31
3.1 Simulations 31
3.1.1 JMatPro 31
3.1.2 ThermoCalc 31
3.2 Experimental samples 32
3.3 Heat treatment 33
3.3.1 Local heat treatment setup 33
3.3.2 Heat treatment design 33
3.4 Sample preparation 36
3.4.1 Cutting and mounting 36
3.4.2 Grinding, polishing and etching 36
3.5 Material Characterisation 37
3.5.1 Microscopy 37
3.5.2 Hardness measurement 38
3.6 Microstructural image processing 39
3.6.1 MIPAR 39
3.6.2 NIS-Elements 40
4 RESULTS AND DISCUSSION 42
4.1 Simulations 42
4.1.1 JMatPro 42
4.1.2 ThermoCalc 44
4.1.3 JMatPro vs ThermoCalc 46
4.2 Defects and As-built condition 47
4.2.1 Defects 47
4.2.2 Prior β grain size 47
4.2.3 Microstructure 47
4.2.4 Hardness 48
4.3 Heat treatments: HT Groups 1 – 4 49
4.3.1 Chemical composition 50
4.3.2 α-case 50
4.3.3 Influence of cooling rate on β grain size 50
4.3.4 Influence of cooling rates on build microstructure 52
4.3.5 Influence of cooling rates on build hardness 53
4.3.6 Influence of cooling rates on α-lath thickness 54
4.3.7 Influence of cooling rates on α and β phase fractions 56
4.4 β-solutionized heat treatments: HT Groups 5 and 6 57
4.4.1 β-solutionized α-case 57
4.4.2 β-solutionized β grain size 59
4.4.3 β-solutionized microstructure 59

4.4.4 Influence of cooling rate on β-solutionized β grain size 60
4.4.5 Influence of cooling rate on β-solutionized microstructure 61
4.4.6 Influence of cooling rate on β-solutionized build hardness 64
4.4.7 Influence of cooling rate on β-solutionized α-lath thickness 65
4.4.8 Influence of CR on β-solutionized α phase fraction 66
4.5 Simulations vs Experimental results 67
5 CONCLUSIONS 70
6 FUTURE WORK 71
7 REFERENCES 72
8 LIST OF ABBREVIATIONS AND SYMBOLS 75
9 LIST OF FIGURES 76
10 LIST OF TABLES 79
11 LIST OF APPENDICES 80
APPENDIX A 81
APPENDIX B 82

1 INTRODUCTION

1.1 Background

GKN Aerospace AB in Trollhättan, Sweden, is a company which is into manufacturing and product support of commercial, space and military jet engines. Over the last few years, it has been investing in, developing, and incorporating additive manufacturing (AM) technologies for producing aerospace engine components. Apart from manufacturing stand-alone engine components by various AM technologies, the company is also developing AM-based repair technologies.

The Aerospace industry has a complex structure involving a lot of intricate flows of information and material between the various entities involved. Aerospace component manufacturers are exploring new ways of designing and producing parts that reduce lead times and material wastage. AM is one such technology which is seeing an increasing use for this purpose. Owing to AM's more 'additive' means of manufacturing, compared to the 'subtractive' means with conventional manufacturing techniques, the advantages have been proven to be significant enough to achieve the purpose to a large extent.

Titanium alloys, due to their advantages like high specific strength at reasonably high service temperatures, good corrosion resistance and compatibility to composites, are widely used in some sections of the aerospace engine. Ti-6Al-4V (Ti64) is one such titanium alloy which is one of the most widely used titanium alloys in aerospace engines and in general.

Ti64 manufactured and processed by conventional methods show mechanical and microstructural properties which differ from those manufactured and processed additively. To ensure additively manufactured Ti-64 can be tailored to suit the service conditions, appropriate heat treatment is necessary to alter the microstructure which then has impact on the resulting mechanical properties.

1.2 Aim

The primary aim of this thesis work is to study the microstructural changes caused by varying the cooling rates during heat treatments carried out on Laser Metal Deposited (powder) Ti-6Al-4V alloy using simulation tools such as JMatPro and ThermoCalc and comparing the results with experimental findings.

1.3 Scope

The scope of this thesis is limited to the analysis of microstructural features and hardness measurements of locally heat-treated samples. The LMD process parameters and the powder characteristics will not be discussed due to confidentiality agreements with GKN. Further, owing to this confidentiality, experimental heat treatment parameters such as temperature and cooling rates will also not be revealed.

2 LITERATURE REVIEW

2.1 The Aerospace industry

The aerospace or aircraft industry has three main entities: Original Equipment Manufacturers (OEMs); Maintenance, Repair and Overhaul (MRO) organizations; and the Customers. The OEMs are the ones that manufacture and assemble the parts of the aircraft and include companies like Boeing and Airbus. MRO organisations are the ones in-charge of the servicing of the aircraft. Finally, the customers are either the airline operators like Air France, Emirates, etc. or the military. Sometimes the customers can be the super-rich who can afford to own private aircrafts, but they are fewer.

When it comes to the overall structure of the aerospace industry which includes the relations, information and workflow interactions between the OEMs, MRO companies and the aerospace supply chain, it can be schematically represented by Figure 1.

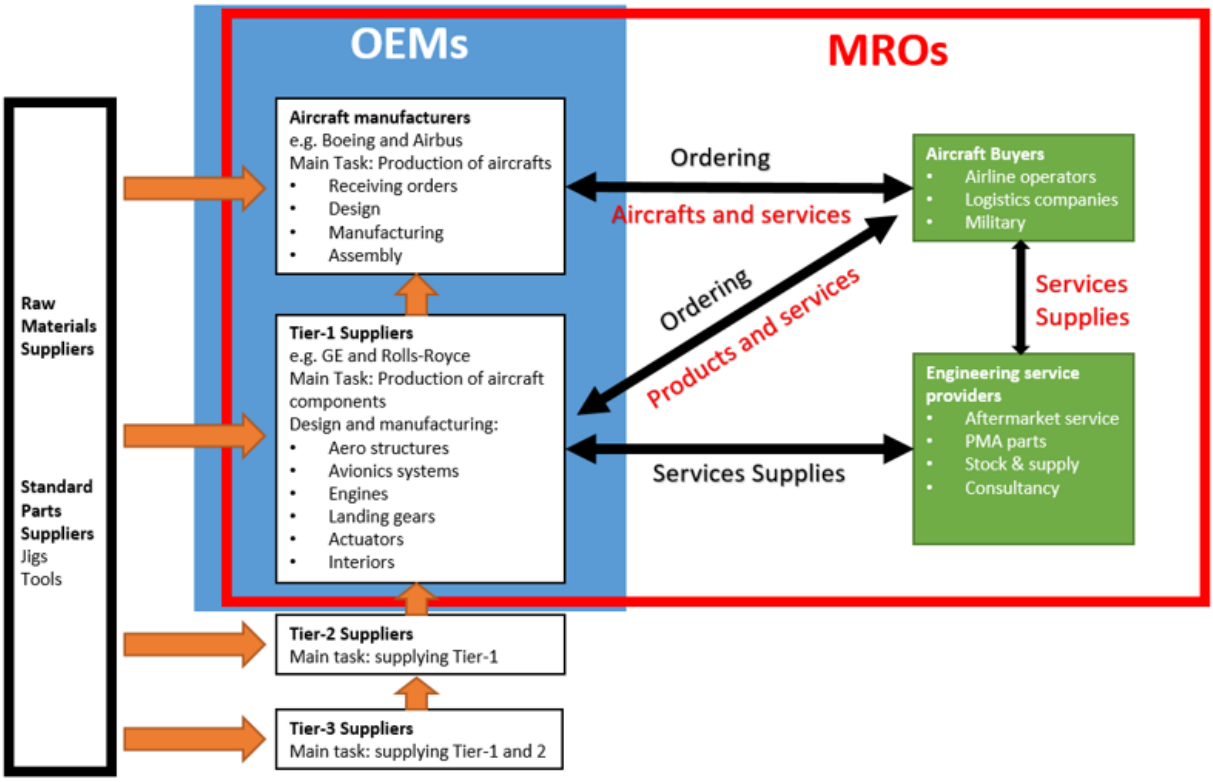


Figure 1. Schematic representation of the roles of critical entities in the aerospace industry and the typical interactions between them [1]

Manufacturers of aerospace components in this complex structure are constantly striving towards the optimization of both design and production techniques with the goal of reducing material wastage and manufacturing lead times by means of applying more lean manufacturing methods. Techniques such as Computer-Aided Design (CAD) and manufacturing and advanced automation have been developed, leading to the increasing attention to additive manufacturing (AM) technologies [1].

2.2 Additive Manufacturing in the Aerospace industry

The use of additive manufacturing (AM) in aerospace applications can be traced back to the late 1980s with the invention of the first rapid prototyping machine for commercial use by 3D Systems and Pratt & Whitney being one of their early customers [2]. Some of the key features of AM that make it attractive for use in aerospace applications are ease of fabricating parts with complex geometries, economically more feasible for small production runs, reduced turnaround times for parts needing repair and the capability of AM to produce high performance parts intended to withstand extreme temperature conditions based on their location in the aircraft [2]. As on 2017, the aerospace industry generated about 18.2% of the total revenue in the global AM industry, with it also being the most rapidly growing sector for AM, witnessing an annual growth of 1.6% in 2016 compared to the 1% annual growth clocked by the automobile sector [3]. According to a survey [4], the global market size for 3D printing products and services is projected to grow from the current 13 billion USD in 2020 to 25.5 billion USD in 2022, and to 40.8 billion USD by 2024. This growth is only bound to be accompanied by the growth in the use of AM products and services in the aerospace applications as well, making it a very relevant and important field of manufacturing in the aerospace industry. The various techniques of AM, its features and advantages will be discussed further in section 2.5.2.

2.2.1 AM in Aerospace engines

Figure 2 shows the schematic of a simple aerospace engine. The main parts of an aerospace engine used in most commercial aircrafts today, known as the 'Turbofan' engine, are the inlet fan, compressor, combustor, turbine, and nozzle. A simple working operation would be the sucking in of the air by the large fan in the front, which is then made to pass through a high-pressure compressor which compresses this air, which then enters the combustion chamber where the fuel is added in order to burn the air, and this hot air is passed through the turbine which in-turn drives the compressor [6]. The final thrust is provided by the pressure from the turbine discharge acting on the nozzle, producing a gas stream of high velocity [6].

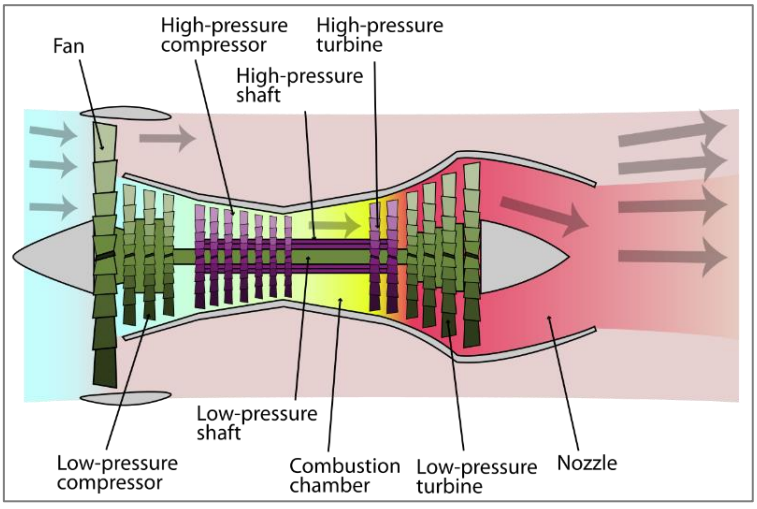


Figure 2. Schematic of a Turbofan engine [5].

Currently, most of these engine components which are geometrically special are manufactured by conventional 'subtractive' machining techniques such as turning, milling, grinding, after the traditional methods of forging and casting [7]. Research done by Han [7] estimates that over 75% of engine components, like fuel nozzles, high pressure turbine nozzles and turbine blades, are suitable to be manufactured by AM owing to their complex shapes and structures. As seen in Figure 3, this growing potential for the use of AM in aerospace engines, and in the aerospace industry as a whole, has led to an increasing trend in research publications in this subject in recent years [1].

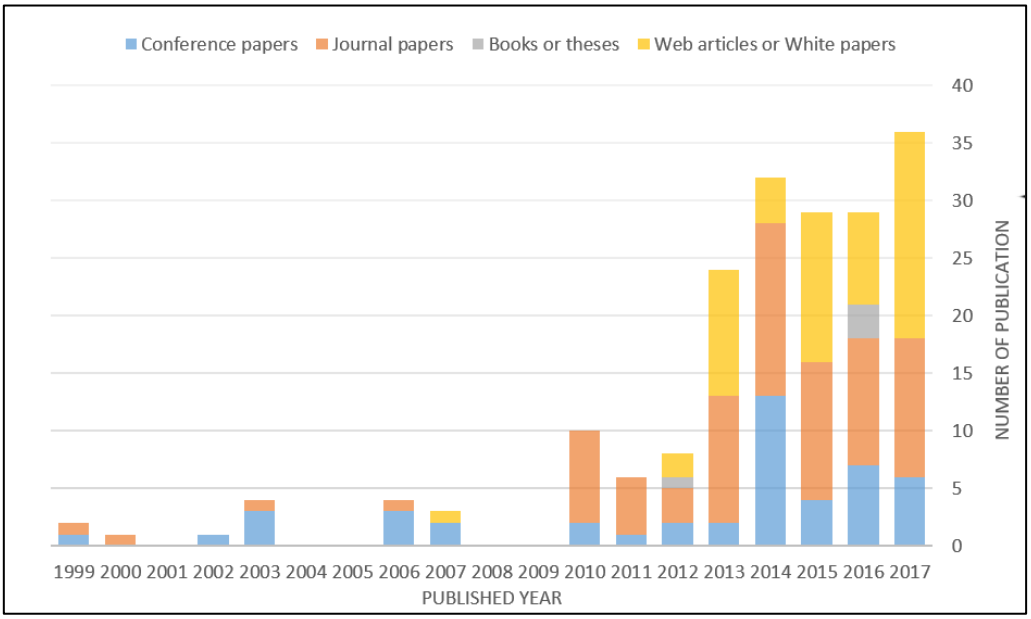


Figure 3. Publication trends related to AM in aerospace industry [1]

2.2.2 Materials used in aerospace engines

The materials used in commercial aerospace engines are required to withstand extreme temperatures; from as low -80°C, at an altitude of 11000 m, to over 50°C at ground level, outside the engine [8]. On the inside, temperatures in the hottest section, the combustion chamber, can reach up to 1500°C [9]. These materials are also required to perform over long periods of flying time when subjected to these temperatures and the accompanying mechanical stresses while being in contact with hot oxidising and corrosive gases being generated by the burnt fuel. Some of the typical properties engine components must possess are high fatigue strength, toughness, tensile strength and creep resistance and the sufficient resistance to the aforementioned oxidation and corrosion at high temperatures [9].

Another key factor that defines what material is used in which part of the engine, hot or cold, is its specific strength, also known as the strength-to-weight ratio, at elevated temperatures. Figure 4 schematically shows the specific strength of some common metallic alloys used in aircrafts as a function of service temperature. It can be seen that at low temperatures, titanium alloys have a high specific strength, and around ~600°C and higher, this specific strength drops to below that of nickel alloys and steel.

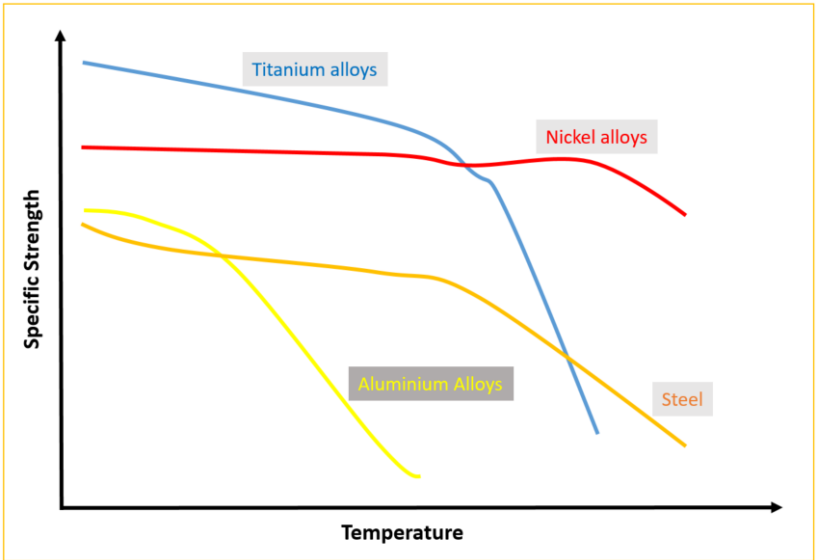


Figure 4. Schematic plot of specific strength as a function of service temperature for titanium, nickel, steel and aluminium alloys. Adapted from [10].

The combustion chamber, turbines and the exhaust zones are generally referred to as the 'hot section' of the engine owing to the high operating temperatures compared to the relatively cooler parts of the engine such as the inlet fan and low-pressure compressor. Some of the most commonly used materials in the hot section of the engine are cobalt-based, nickel-based and iron-nickel alloys, which belong to a class of materials called 'Superalloys'. These superalloys are sometimes coated with ceramics for increased insulation to the extreme heat conditions [9]. The focus of this thesis work is on titanium alloys which, owing to their high specific strength at lower temperatures, are limited to their use only in the cooler sections of the engine.

2.3 Titanium and its alloys

Titanium, 'titan' in Swedish, is a metal named after Titans, the mighty sons of the earth, according to Greek mythology. In terms of its availability, it is the fourth most abundant structural metal in the earth's crust behind aluminium, iron, and magnesium, at a level of around 0.6% [11]. Some of the key properties which make titanium extremely attractive for various applications like aerospace engine components, biomedical devices and chemical equipment are high strength-to-weight ratio, good performance at temperatures up to 550^{o}C and good corrosion resistance.

In the aerospace industry, a huge advantage titanium holds over its closest competitor aluminium, for light-weight structural applications, is that it has a significantly higher melting temperature; around 1670^{o}C compared to aluminium's 660^{o}C. Another advantage is, as seen in Figure 4, the specific strength of aluminium drops significantly at temperatures above ~200^{o}C, hence limiting its use to that temperature whereas titanium alloys can be used up to ~600^{o}C. One of the major drawbacks of titanium which limits its wide use and application is its high reactivity to oxygen around 600^{o}C to form a brittle Titanium Oxide (TiO_2) layer which is undesirable in engineering applications. This not only limits its operating temperature but also means the processing of titanium will require inert gas atmospheres, making it an expensive metal for many engineering applications.

2.3.1 Titanium extraction

The main sources of and starting forms for titanium production are either Rutile (TiO_2) or Ilmenite ($FeTiO_3$). Titanium present in these sources, or ores, is called 'Sponge' due to its porous and sponge-like structure. The typical steps in the extraction of pure titanium from these ores can be summarised briefly as below [11]:

- Chlorination or Electro-melting: $TiCl_4$ formation by the addition of chlorine if the source is Rutile; TiO_2 formation by electro-melting with carbon if the source is Ilmenite.
- Distillation: $TiCl_4$ purification by fractional distillation in two steps. Impurities with low boiling points like CO and CO_2 are removed in the first step. Impurities with high boiling points such as $SnCl_4$ and $SiCl_4$ are removed in the second step.
- Reduction or Kroll process: $TiCl_4$ reduction in an inert atmosphere containing Mg at temperatures around 800 – T3 which gives rise to the following reduction reaction:
  $TiCl_4 + 2Mg \rightarrow Ti + 2MgCl_2$
  The product of the Kroll process is an intermingled solid mixture of metallic titanium and magnesium chloride called as "sponge cake".
- Purification: Removal of Kroll process by-product $MgCl_2$ and extraction of pure titanium from the sponge cake by methods such as inter gas sweeping, vacuum distillation, or acid leaching.
- Crushing and Sizing: Crushing and resizing of the pure titanium sponge from the previous step carefully in air to form small granules of metallic titanium, to be used in subsequent processing techniques such as forging or casting to titanium alloys.

2.3.2 Titanium crystal structure

Titanium exists in two main forms or phases: α (alpha) phase with a hexagonal close packed (HCP) crystal structure at low or room temperatures and, β (beta) phase with a body-centred cubic (BCC) structure at temperatures above a certain point known as the $\beta_{transus}$ temperature. This $\beta_{transus}$ temperature depends on the number of alloying elements present and whether they are α-stabilizers or β-stabilizers, which will be discussed more in detail in the following section.

The two Ti phases and their crystallographic structure along with the most densely packed lattice planes are illustrated in Figure 5. A unit cell of the α-phase, Figure 5(a) has three types of densely packed planes, namely the basal plane (0002), the prismatic plane $(10\bar{1}0)$ and the pyramidal plane $(10\bar{1}\bar{1})$; with the axes a_1, a_2 and a_3 being the three close-packed directions with $<11\bar{2}0>$ as indices. A unit cell of the β-phase has six densely packed lattice planes, with one of the variants (110) indicated in Figure 5(b).

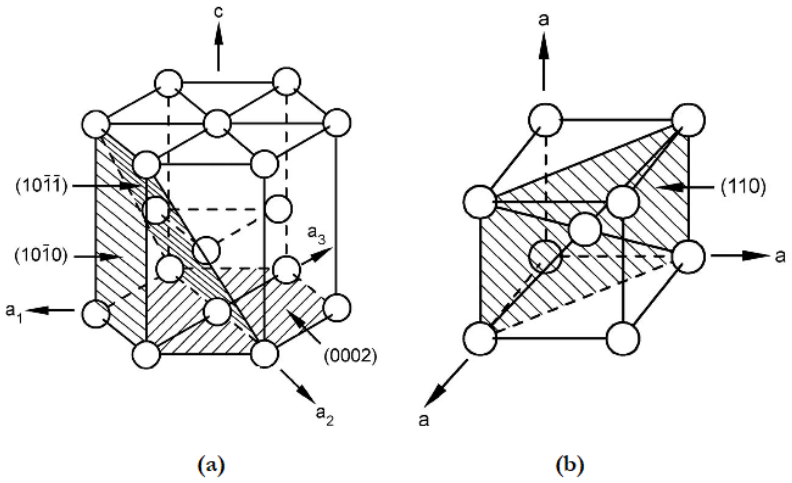


Figure 5. Schematic crystal structure of titanium (a) α-phase and (b) β-phase [11]

2.3.3 Phase transformations in titanium alloys

There are two main mechanisms of phase transformations present in Commercially Pure (CP) titanium and titanium alloys: nucleation and growth, which is a diffusion-controlled process; and martensitic transformation, which is a diffusion-less process. These transformations depend mainly on the cooling rates during processing or thermal treatments and the composition of the alloy and governs how the BCC β-phase transforms to the HCP α-phase.

2.3.3.1 Diffusion-less martensitic transformation

The martensitic phase transformation occurs when titanium alloys are heated to temperatures above the $\beta_{transus}$ temperature, called the β phase field, and cooled at sufficiently high cooling rates. This type of transformation is governed by a non-diffusional, shear type transformation wherein movement of atoms occur cooperatively and results in a homogenous transformation of the BCC crystal into an HCP crystal over a certain volume. This HCP crystal, called 'martensite' in titanium alloys and denoted as α', is usually found to be plate or disk shaped. There are two morphologies of α' observed and they are called massive (also called lath or packet) martensite and acicular (needle-like) martensite [11].

Massive martensite is observed only in CP titanium and in alloys where the martensite start temperature is high. A characteristic visual description of this morphology would be the presence of large non-uniform regions with no distinct internal features, containing small packets of parallel α laths of the same Burgers relationship variant, when viewed under a light optical microscope. Acicular martensite on the other hand can be seen having a mix of thin individual α laths having different Burger's relationship variants [11].

2.3.3.2 Diffusion-controlled nucleation and growth

During cooling of titanium alloys from the β phase field, if relatively slow cooling rates are maintained, upon reaching the α+β phase field, or temperatures below $\beta_{transus}$, the incoherent α phase starts to first nucleate at

the β grain boundaries since they act as preferential sites for nucleation, resulting in a continuous layer of α phase along the β grain boundaries. The different microstructural characteristics, phases and types of microstructure morphologies resulting from this type of diffusion-controlled phase transformation is discussed in section 2.4.1.

2.3.4 Titanium alloys

Based on the alloying elements added to pure titanium, its alloys can be mainly classified into α alloys, α+β alloys and β alloys. These alloying elements can further be classified into α-stabilizers and β-stabilizers, depending on its effect on the α to β transition, or $\beta_{transus}$ temperature, as illustrated in the schematic phase diagrams in Figure 6. Addition of α-stabilizers will lead to an increase in the $\beta_{transus}$ temperature, thereby stabilizing the α-phase region, whereas the addition of β-stabilizers will reduce it, thereby stabilizing the β-phase region.

Among the α-stabilizers, Al is a substitutional solid solution element and is the most commonly used alloying element owing to its vast availability and high solution capabilities in both α and β phases. O, N and C are the other major α-stabilizers which are interstitial solid solution elements, with O being the most widely used in cases where high strength levels are desired.

β-stabilizers are divided into two types: β-isomorphous and β-eutectoid; based on their effect on the final binary phase diagram, both of which are shown in Figure 6. Among the β isomorphous alloying elements, V, Mo and Nb are the most frequently used, whereas Fe, Cr and Si are the most commonly used β eutectoid alloying elements [11].

There exists a third type of alloying elements like Zn and Sn which have a more 'neutral' effect on the $\beta_{transus}$ temperature, wherein the addition of these elements in low concentrations lowers the $\beta_{transus}$ temperature while it is increased with the addition of these elements in higher concentrations.

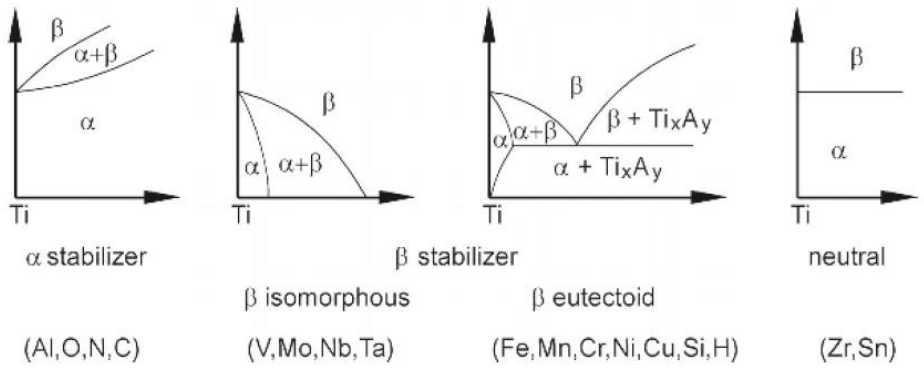


Figure 6. Schematic phase diagrams of titanium alloys showing the effect of different alloying elements. [11]

Another basis for the classification of commercial titanium alloys into α alloys, α + β alloys and β alloys is with the use of a pseudo-binary section of a β isomorphous phase diagram as illustrated in Figure 7.

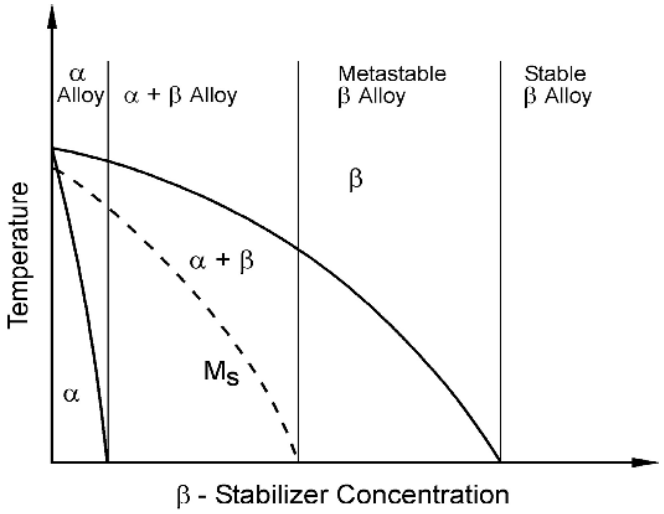


Figure 7. Titanium alloy classification based on a β isomorphous phase diagram [11]

2.4 Ti-6Al-4V

Among all titanium alloys, Ti-6Al-4V (Ti64) is commonly termed as the workhorse of the titanium industry, accounting for over 60% of the overall titanium production globally [12]. It is an α+β alloy which retains at room temperature, both the low temperature allotrope α and the high temperature allotrope β due to the alloying of 6% Al stabilizing the α phase and of 4% V stabilizing the β phase. The typical composition of Ti-6Al-4V is shown in Table 1.

Table 1. Chemical composition of Ti-6Al-4V [13]

Element wt.%	**Al**	**V**	**Fe**	**O**	**N**	**C**	**H**	**Ti**	**Others (Each)**	**Others (Total)**
Min.	5.50	3.50	0	0	0	0	0	balance	0	0
Max.	6.75	4.50	0.40	0.20	0.05	0.08	0.015	balance	0.10	0.40

The $\beta_{transus}$ temperature of Ti64 according to the ASM handbook [14] is 1000 ± 20 ºC, with the exact temperature dependant on the number of alloying elements.

What makes Ti64 an attractive material for use in engineering applications, especially in the aerospace industry, is its properties such as high strength-to-weight ratio, high fracture toughness, good corrosion resistance and compatibility to composites. Another feature of Ti64 that makes it an extremely popular titanium alloy is the possibility of obtaining balanced mechanical properties based on the application by altering its microstructure by performing tailored heat treatments [15].

2.4.1 Ti-6Al-4V phases and microstructure morphologies

Some of the most commonly found phases in Ti64 and the reasons behind their formation are listed in Table 2.

Table 2. Phases of Ti-6Al-4V and the reasons behind their formation.

Phases	Present/formed when
Primary α	At room temperature, stabilized by Al, O
Primary β	At room temperature, stabilized by V, Fe
Transformed β	Above βtransus; Transformed from primary α
Secondary α	Transformed from β during slow cooling from βtransus; Nucleation and growth controlled transformation.
α' (alpha prime – Hexagonal)	Transformed from β during fast cooling from βtransus; Diffusion-less transformation.
α" (alpha double prime – Orthorhombic)	Transformed from β during fast cooling from βtransus in Ti64 alloys rich in β-stabilizers [11]; Diffusion-less transformation.

The different microstructural morphologies the above listed phases are found to take are listed in Table 3.

Table 3. Typical Ti-6Al-4V microstructure morphologies, reasons behind their formation and their features. Adapted from [15].

Morphology	Formed when	Features
Widmanstätten / Lamellar	Slow or furnace cooling from β-phase field	- Coarse and complete prior β grains - Continuous α on prior β grain boundaries - α-colonies with parallel α-lamellae
Duplex / Bi-modal	Heat-treated and deformed in the α+β phase field	Less than 50% of transformed β matrix has equiaxed α-phase distributed
Basket-weave	Heat-treated and deformed high up in the α+β, near βtransus	Prior β grain boundaries broken, α-lamellae
Equiaxed	Heat-treated at or above βtransus, held for longer time periods and deformed heavily	Finely equiaxed α and β grains

2.4.2 Ti-6Al-4V oxidation and α-case

As mentioned in section 2.3, Ti64 and titanium alloys in general undergo titanium oxidation when exposed to air at temperatures around 600^{0}C or above to form TiO_2 which has a tetragonal crystal structure. Oxygen ions diffuse into the titanium base material via an oxide layer called scale, with the driving force for this rapid oxidation being titanium's high chemical affinity to oxygen. During this process, the scale formation is accompanied by the formation of an oxygen-rich layer in the titanium base metal. This oxygen-rich layer formed is a layer of oxygen-stabilized α phase called the α-case which is extremely brittle and can cause surface crack formations under tensile loading. Under fatigue loading conditions, this brittle α-case formed surfaces can reduce the overall ductility of the alloy or lead to early crack propagation [11].

2.4.3 Ti-6Al-4V applications

Ti64 finds its use in various aerospace applications ranging from structural parts such as landing gear beams to engine parts such as casings, frames, ducts and other rotating as well as non-rotating parts. In the power generation sector, Ti64 has been reported to be used as the material for steam turbine blades, whereas in the oil and gas sector, it is used as the preferred material to steel for tubular riser systems [11]. The alloy also has limited application in the military sector, being used for making armour components in military tanks [16]. Some of the other Ti64 applications can be found in the biomedical industry as bone implants, sporting goods industry as gold clubs, and automobile industry as exhaust systems and suspension springs.

2.5 Ti-6Al-4V processing and thermal treatments

The starting stage of obtaining Ti64 and other titanium alloys from pure titanium begins by melting, followed by alloy addition and subsequent re-solidification to produce ingots, which then serve as the starting material for milled products and as re-melt stocks for further casting products. Due to the high reactivity of molten titanium, special considerations are required to produce ingots of titanium alloys. The two main types of furnaces used for this melting process are Vacuum Arc Remelt (VAR) furnace and Cold Hearth Melting (CHM) furnace, both of which are designed to prevent the highly reactive titanium from being exposed to air.

2.5.1 Conventional shaping techniques

The produced Ti64 ingots are subjected to traditional shaping techniques such as forging followed by finishing operations such as milling, turning, or drilling; casting, powder metallurgy and sheet forming. In this section, only casting and forging will be reviewed in order to understand and compare these conventionally manufactured (CM) techniques to AM techniques.

2.5.1.1 Casting

Casting of titanium alloys, including Ti64 are, done using two main methods: conventional casting and investment casting. In conventional casting, rammed graphite is used as the mold material due to its low reactivity to molten titanium which gives castings with better surface finish when compared to sand molds used for casting of ferrous alloys. In investment casting, the pattern of the final shape is used to make a mold with wax, which is then given a nonreactive coating to reduce reactivity to molten titanium, giving castings with minimum further material removal compared to conventional castings. Extreme care and caution need to be taken during casting of Ti64 due to the high reactivity of molten titanium. Casting furnaces are maintained in vacuum during the whole process and nonreactive melting techniques such as the ones used in VAR with both consumable and non-consumable electrodes are necessary [11]. Most as-cast titanium alloys are subjected to a Hot Isostatic Pressing (HIP) operation to reduce the porosity and other shrinkage defects during the solidification stage, which are typically seen in cast products. This HIP treatment after casting has been reported to increase the fatigue properties by twofold. Other post casting operations typically involve chemical milling and a stress relief heat treatment before the products can be used [11].

Compared to the forging technique, castings have an advantage of producing near-net-shapes with minimum material wastage, leading to a reduction in overall production cost. In terms of drawbacks, castings are known to produce more defects such as gas-entrapped pores in the bulk material, surface connected defects from shrinkage, shrinkage voids, hot tearing and non-continuous mold filling. Although most of these defects can be reduced or removed during the HIP operation, some need an additional weld repair which adds to the final production cost [11].

2.5.1.2 Forging

Titanium alloys, including Ti64, are typically forged using drop or steam-driven hammers and large presses driven by hydraulic actuators or mechanical screws. Due to the higher flow stresses incurred during the forging of titanium alloys compared to aluminium or steel alloys, the forging pressures needed are much larger, which induces equipment-based limits on the ease of forging [11].

The two main methods used in titanium alloys forging are closed die forging where the work piece is constrained in the lateral direction, and open die forging where there are no such lateral constraints. Which method is preferred depends on the level of microstructural control required and the criticality of the product's application and other economic factors such as how many forgings are to be made. Titanium forgings used in aircrafts like airframe parts or aero engine parts require several forging steps starting from an initial roughing operation followed by non-uniform forging at sections where large cross-sections are desired and finally a finish-forging step to produce the final shape. The number of such forging steps needed is defined not only by the size and complexity of the part, but also by the workability of the alloy. In case of forging Ti64, forging operations are usually carried out in the $\alpha+\beta$ phase field but if higher

deformation resistant properties are desired in the final product, forgings in the β-phase field are also performed [11].

The main advantage of the forging technique is the ability to control the obtained final tailored microstructure based on the final properties desired by setting the appropriate thermomechanical parameters. Some of the main drawbacks of this technique are the higher cost incurred owing to the requirement of further mechanical machining to obtain the final shape and the loss of material during these finishing operations. In most cases, the key advantage of controlling the final microstructure and the resulting mechanical properties, outweighs the high cost incurred in making and machining forgings, making it the most commonly used CM technique [11].

2.5.1.3 Thermomechanical treatments

Conventionally shaped Ti64 by techniques like forging and casting are subjected to thermomechanical treatments in the respective processing routes to obtain final microstructures based on the mechanical properties desired in the final product. The three most distinct microstructure morphologies in Ti64 resulting from such treatments are: fully lamellar microstructures, bi-modal or duplex microstructures and fully equiaxed microstructures. The details on the thermomechanical routes followed to obtain the first two types of microstructures will not be presented in this review since only the third type, fully equiaxed microstructures, is of relevance and key to understand.

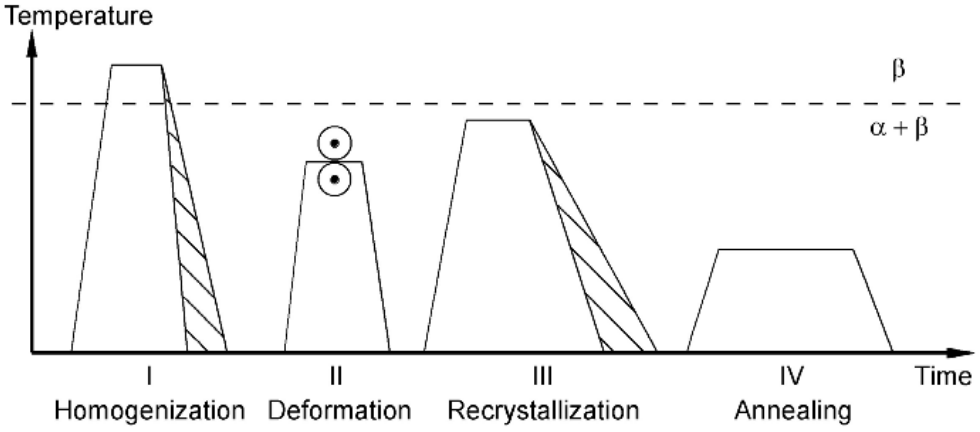


Figure 8. Thermomechanical processing route for obtaining equiaxed microstructures in Ti-6Al-4V [11]

There are two ways in which a fully equiaxed microstructure can be formed and the thermomechanical treatment of one such route is shown schematically in Figure 8. The alloy is subjected to steps I and II during the forging process itself and steps III and IV require further thermal processing. The recrystallization step III is done at temperatures close to $\beta_{transus}$ and cooled at sufficiently low cooling rates to ensure the growth of only the primary α grains from step II and prevent the growth of any secondary α lamellae within the β grains. This gives a fully equiaxed microstructure with the volume fraction of the β phase at the α grain triple-junction (point at which three α grains meet) reaching equilibrium.

2.5.2 Additive Manufacturing (AM)

In contrast to CM which is a subtractive manufacturing method which involves removal of material to produce the final products, AM is a method based on an incremental type of layer-by-layer forming of the final product. Owing to unique advantages such as forming of near-net-shaped parts, high buy-to-fly ratio, high design freedom and short lead times, AM has attracted a significant amount of attention in the last 15 years [17]. Most AM techniques use either wire or powder as feedstock which is melted selectively by a focused heat source and then subsequently fused during cooling to form the part.

The key features that form a comprehensive roadmap for AM covering all the essential considerations was published by Bourell et al. [18] and has been briefly listed below:

- Design
- Materials, processes, and machines
- Process modelling and control
- Biomedical applications
- Energy and sustainability applications

2.5.2.1 AM techniques

According to ISO 17296-2:2015, the classification of AM techniques into seven categories is shown schematically in Figure 9. AM is applicable to and can be used for classes of materials like polymers, ceramics, composites, apart from metals. Among all the seven AM categories, the techniques that are most relevant and developed for metals, including Ti64, are:

- Electron Beam Melting (EBM) – *Powder Bed Fusion (PBF) category*
- Laser Beam Melting (LBM) – *Powder Bed Fusion (PBF) category*
- Laser Metal Deposition (LMD) – *Directed Energy Deposition (DED) category*

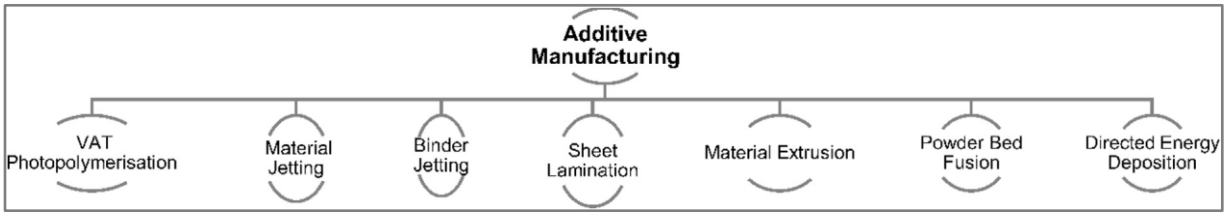


Figure 9. The classification of AM techniques according to ISO 17296e2:2015 [n18]

Among these AM techniques, the focus of this thesis work is on the LMD process which will be discussed in the following section.

2.6 Laser Metal Deposition (LMD) of Ti-6Al-4V

LMD-p, p being an abbreviation for powder, is an AM process which uses powder as the feedstock and belongs to the DED category of AM techniques. A schematic of the LMD-p process is shown in Figure 10. Energy from a laser beam with power in the range of 500 W to a few kW is used to melt Ti64 powder onto a substrate by forming layer-by-layer melt pools which then solidify subsequently to the final shape desired. The Ti64 powder is fed by a feeding system with a carrier gas and the whole process chamber is filled with an inert gas to avoid oxidation of the melt pool.

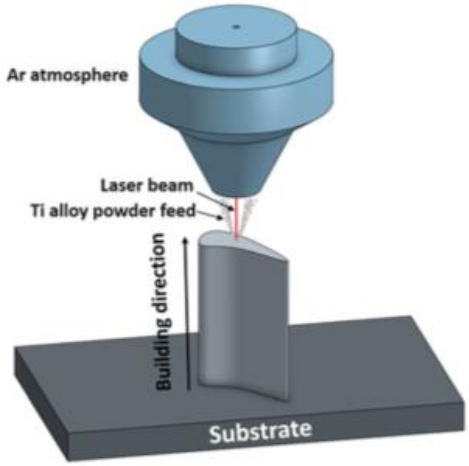


Figure 10. Schematic of the LMD-p processing of Ti64 [20]

Some advantages the LMD process hold over some other AM techniques are:

- Unlike in EBM process, LMD does not require a vacuum chamber for building parts, thereby not limiting the part size that can be built.
- LMD has lower heat input and smaller heat affected zones (HAZ) when compared to EBM, which reduces the influence of the build on the surface of the substrate.

Advantages the LMD process has over other AM techniques are:

- LMD is a free-form method of fabrication which allows to build parts directly from a 3-D CAD file without the need to design supports which are common for techniques in the PBF category.
- LMD has more dimensional flexibility and is ideal for near-net-shape fabrications when compared to other AM processes.
- LMD exhibits much high build rates when compared to other AM technique.

The above listed advantages give LMD the following unique aerospace applications:

- LMD can be used for repair and refurbishments of aero engine parts.
- Real-time adjustments to the powder composition can be made which gives the opportunity to build parts with site-specific compositional properties [20].

Some of the main drawbacks of the LMD process are the presence of defects in the as-build parts which will be discussed in the following section.

2.6.1 Defects in LMD Ti-6Al-4V

The process parameters and the attributes of the powder used in the LMD process are the two main factors that govern the formation of defects in the built parts. Defects can be simply defined as any features seen in the microstructure of parts that deviate from those that are desired based on the final application. What is characterised as defects based on this definition could be any structural deviation from an ideal uniform and fully dense build. This section and the thesis work will focus on only two such defects related to porosity commonly seen in parts built by LMD-p and other DED techniques:

- Gas porosity:
  Gas porosity defects are typically circular in shape and attributed to the entrapment of the shielding or inert gas used in the build chamber. There are three main sources of gas porosity in LMD-p. If the powder flow rate is too high, the melt pool specific energy drops which results in an increase in gas entrapments. The second source is when gas is entrapped in the initial powder particles itself which remains even after the build is complete [21]. The third source is due to Marangoni flow – a phenomenon based on the mass transfer across an interface of two fluids due to a difference in the surface tension, causing gas retention bubbles inside the melt pool leading to pores of large sizes [22]. A typical gas porosity is shown Figure 11(a).

- Porosity due to Lack of Fusion (LoF):
  LoF porosity defects are typically irregularly shaped and formed when the energy in the melt pool is insufficient to melt the powder particles, thereby causing incomplete fusion [21]. When the distance between the deposition nozzle and substrate varies, the laser beam gets defocussed, resulting in a drop in the energy density and eventually in LoF defects [22]. Another factor that could potentially cause LoF porosity is the substrate size and composition which controls the heat dissipation away from the melt pool – if the heat dissipation is too high, more is the tendency for LoF formation [21]. A typical LoF defect is shown Fig 11(b).

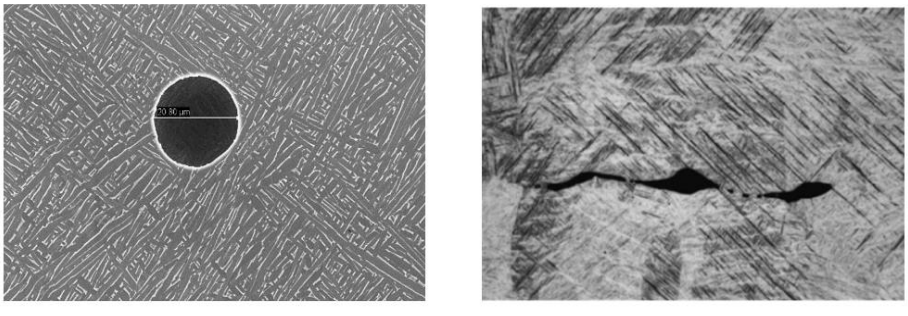


Figure 11. (a) Gas porosity seen under SEM; (b) Lack of Fusion seen under LOM [21]

2.6.2 Thermal history during the LMD process

During the LMD-p process, it is essential to understand the large number of heating and cooling cycles that each deposited layer experiences and the effect it has on the resulting microstructure. It is important to note here that the commonly reported cooling rate during the LMD process is reported to be around 3500°C/min, which is much higher than the minimum cooling rate needed for the formation of α' martensite which is around 1000°C/min [19]. A schematic of the thermal history for a single deposited layer is illustrated in Figure 12. It is seen that the peak temperature for the layer decreases continuously over time, despite the repeated heating and cooling cycles. Dividing this schematic into 3 regions namely A, B and C, we see that in:

- Region A: The peak temperature is above the $\beta_{transus}$ (T_β) and the primary α phase transforms completely to β phase. This β phase then transforms back to α phase during subsequent cooling along with the formation of some amount of α' martensite.
- Region B: After a certain amount of time and the deposition of a few layers on top of the layer being studied, the peak temperature drops below T_β, some of the partial transformed α phase and α' transforms back to β phase during heating and upon cooling, there's formation of newer α lamellae and α', along with the coarsening of the existing α lamellae.
- Region C: After a longer period, the layer's peak temperature drops below T_α, which is a region with temperature lower than that needed for any phase transformations to occur, leading to a stabilization of the as-deposited microstructure with a mix of α+β morphology and α'.

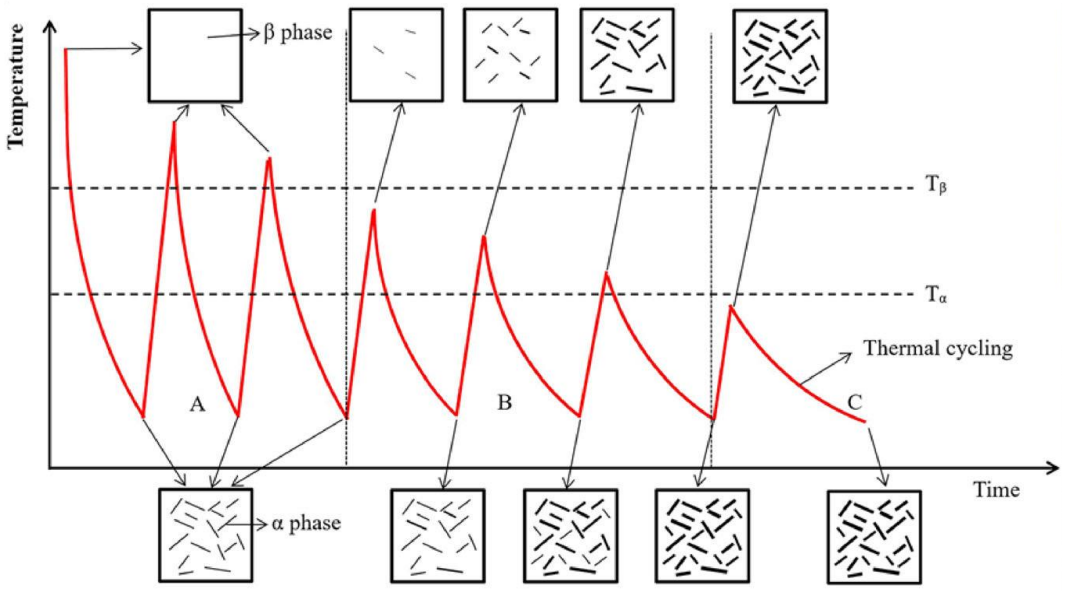


Figure 12. Schematic representation of the thermal history during LMD of Ti-6Al-4V [20]

Apart from these phases, Ahmed et al. [23] reported the formation of a massive α (α_m) when the cooling rates are between 20°C/s and 410°C/s. Lu et al. [24] reported and studied the formation of this α_m phase formation in Ti64 fabricated by EBM and characterized it to be a set of featureless patches when viewed under a SEM.

2.6.3 Microstructural features of LMD-p Ti-6Al-4V

After understanding the effect of the thermal history on the solid-state phase transformations and the resulting phases in the microstructure, the effect of the same on the microstructural morphology gives a holistic view of the as-built microstructural features. Figure 13 shows the schematic cross-sectional view of typical deposited layer during LMD of Ti64. Due to the high heat dissipation away from the melt pool by the substrate, the solidified β grains get elongated in a unidirectional manner giving it the typical columnar grain morphology. The fine equiaxed β grains region seen on the surface of the melt pool are the result of newly nucleated grains at heterogeneous sites provided by the partially melted or un-melted powder particles [20]. The β grain growth can be seen not to be so significant close to the fusion line or in the HAZ. This is due to the high thermodynamic stability of the as-deposited columnar and coarse prior β grains in this region [25]. As a result of the high cooling rates and rapid solidification, the newly deposited layer and the HAZ have acicular α' whereas the substrate microstructure remains unaffected.

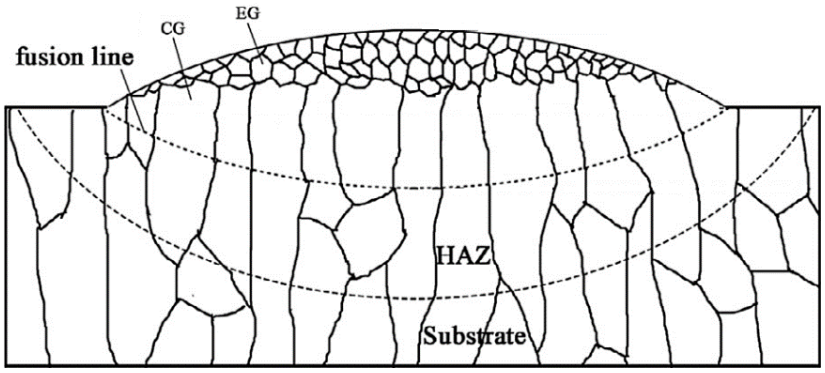


Figure 13. Schematic cross-section of an as-deposited layer during LMD of Ti-6Al-4V, showing the Heat Affected Zone (HAZ) and regions of Columnar Grains (CG) and Equiaxed Grains (EG). Adapted from [25]

2.6.4 Mechanical Properties of LMD Ti-6Al-4V

As a result of the non-uniform microstructures obtained from LMD in the as-built condition, there is an influence of this on its mechanical properties. It is therefore useful to understand the mechanical properties such as Ultimate Tensile Strength (UTS), Yield Strength (YS) and Elongation (El. %) of Ti64 parts fabricated by different AM techniques such as LMD, Selective Laser Melting (SLM) and EBM, and compare them to those of CM Ti64 parts. Liu et al. [26] reviewed this in their work and the tensile properties as reported by them are presented in Table 4.

Table 4. Tensile properties of Ti-6Al-4V manufactured by AM and CM techniques. Adapted from [26].

Process	Specimen Orientation	UTS, MPa	YS, MPa	El, %
DED	Longitudinal	984-1050	930-987	~4.8
	Horizontal	1033-1109	941-1029	~6.8
SLM	Longitudinal	1246 ± 134	1150 ± 67	1.4 ± 0.5
	Horizontal	1211 ± 31	1100 ± 12	6 ± 0.6
EBM	Longitudinal	928 ± 9.8	869 ± 7.2	9.9 ± 1.7
	Horizontal	978 ± 3.2	899 ± 4.7	9.5 ± 1.2
Forged	Mill annealed	1030	970	16
Cast	-	980	865	13.5

It is seen that the UTS and YS of all three AM techniques are generally higher than that of CM Ti64 but the elongation of AM parts is lower than those of CM Ti64. The same holds true for the comparison between LMD Ti64 and CM Ti64 as well. This gives rise to the need for post processing of AM Ti64, by means of heat treatment, to achieve the desired mechanical and microstructural properties based on the products' end application.

2.7 Heat Treatment of LMD-p Ti-6Al-4V

Heat treatment is the process of heating a metal to temperatures below the melting point, holding it at those temperatures for a certain amount of time and cooling it to intermediate temperatures or to room temperatures at certain cooling rates. Heat treatment is used to enhance both the mechanical and microstructural properties of metals based on the end application. Depending on how much the properties are to be altered, the four typical heat treatments given to metals are annealing (includes stress relieving, normalizing, recrystallization), hardening (includes quenching), tempering and ageing.

When it comes to the heat treatment of LMD-p Ti64, many of the conventional heat treatments applied to CM Ti64 such as stress relief treatments, annealing, solution treating and ageing, and HIP cannot be directly replicated for LMD Ti64 with the expectation of obtaining similar results. This is mainly due to the microstructures of parts processed by the conventional routes and the ones processed by the additive route are different and will not yield the same heat treatment results. Based on previous work reviewed on heat treatment of LMD Ti64 by Azarniya et al. [19], it can be concluded that similar heat treatments performed on parts with different process parameters yield different results in terms of mechanical properties – indicating the lack of a universally applicable heat treatment cycle for property enhancement of LMD Ti64 in general. It is therefore necessary to study the effect of different heat treatment parameters on the microstructural and mechanical properties, and their correlations, so as to tailor heat treatments specific to the LMD process parameters.

The key heat treatment parameters to be considered for LMD Ti64 are the heat treatment temperature, holding time and cooling rate.

The most important microstructural parameter that indicates the mechanical properties of Ti64 is the α-colony size [27][28][29][30]. An α-colony can be defined as a cluster of 3 or more parallel α-lamellae with same crystallographic orientation inside a prior β grain [31]. Smaller the α-colony size, smaller is the α-lamellae/lath thickness, and higher is the strength since it has a direct correlation to the material's slip length [29].

2.7.1 Influence of heat treatment temperature and holding time

In a general sense, the phases present at room temperature in an as-built LMD Ti64 are non-uniformly distributed α' and α+β in either widmanstätten or basketweave morphology. The review of the effect of heat treatment temperature and time on LMD Ti64 can be summarised in two parts: when the heat treatment temperature is at or above the $\beta_{transus}$ and when it is below the $\beta_{transus}$ temperature.

When LMD Ti64 parts are heat-treated to or above the $\beta_{transus}$ temperature, also known as super-transus, the columnar prior β grains present in the as-built state undergo a shearing mechanism and lose their columnar morphology and attain a more semi-equiaxed or globular morphology with quantifiable growth in grain size [19] [32] [33]. The primary as-built α' undergoes complete decomposition and the amount of transformed α', α+β phase fractions and morphology, thickness and length of α nucleated on the prior β grain boundary and α-lath thickness depends solely on the cooling rate during heat treatment. Brandl et al. [34] showed that holding LMD Ti64 parts during super-transus temperature for longer times did not have an effect on the microstructure and hardness, and that the cooling rates from this temperature had the only effect.

During heat treatments at temperatures below $\beta_{transus}$, also called sub-transus treatments, depending on the temperature and holding times the effect on the microstructure varies. The prior β grains have been shown to remain largely unaffected as a function of heat treatment temperature and time since the α phase resulting from the decomposition of α' inhibits β grain boundary movement [32] [35]. Mur et al. [36] studied the decomposition of α' as a function of heat treatment temperature and time. They showed that at temperatures below 600^{o}C, α' remains unaffected; between 600^{o}C and T2, there is partial decomposition of α' and at T2 and above, there is complete decomposition of α' to more stable α+β phases. This is useful in considering when tailoring heat treatments for increasing the ductility of LMD Ti64 as it is shown that heat treatments below T2 does not have a significant effect on ductility [26]. The influence of the sub-transus treatments of LMD Ti64 between heat treatment temperatures of T2 up to $\beta_{transus}$ is reported to be only on the amount of α' decomposition to α+β and the α-lath thickness, with both increasing as a function of temperature and time; and on the hardness, reported to be decreasing as a function of increasing temperature and time [19] [32] [36].

2.7.2 Influence of cooling rate during heat treatment

Similar to the effect of heat treatment temperature and time, the effect of cooling rates during heat treatment can also be summarised in two parts: for cooling from super-transus and from sub-transus temperatures.

When LMD Ti64 parts are heat-treated at super-transus temperatures, the cooling rate is the only factor that influences the phases present after cooling and the microstructural morphology. At high cooling rates, the transformation of the β-phase to α' through the diffusion-less process is preferred whereas a nucleation and growth controlled transformation to α+β phases is preferred at slow cooling rates. Reported literature on the critical or minimum cooling rate for the onset of α' is inconsistent. Ahmed et al. [23] reported it to be 410°C/s, as shown schematically in Figure 14, whereas Qazi et al. [37] and Boyer et al. [38] reported it to be around 16.5°C/s. It is therefore important to determine this critical cooling rate for this β to α' for the specific alloy composition during the heat treatment design stage either experimentally or by using simulation tools discussed in the following section. At cooling rates lower than this, lower the cooling rate, lesser will be the amount of α' formation, more will be the formation of α+β phases and bigger will be the α-colony size and α-lath thickness. This will consequently lead to the formation of more of the α-phase, resulting in higher α-phase fraction. Azarinya et al. [19] reviewed this coarsening of the α-lath to also correlate with a decrease in strength and increase in ductility. The exact morphology the α+β phases formed based on the rate of cooling is shown in Table 3 in section 2.4.1.

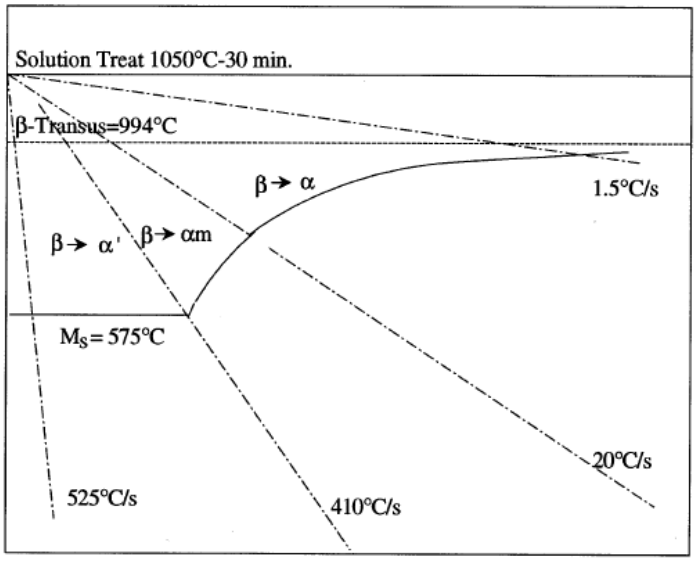


Figure 14. Schematic of phase transformations during cooling at different rates from super-transus temperatures [23].

When it comes to sub-transus heat treatments, the cooling rates have been reported to have the same effect as for the super-transus treatments but only when heat-treated at temperatures close to the $\beta_{transus}$ [39]. Research work carried out on the detailed effect of cooling rates during sub-transus heat treatments in LMD-p Ti64 is scarce. Vrancken et al. [39] studied the influence of cooling rates on sub-transus heat treatments on Ti64 fabricated by SLM AM technique which also uses powder as the starting material. They

reported their as-built conditions before heat treatment which are similar to the ones seen typically in LMD built samples in terms of both microstructure and mechanical properties. During heat treatments at T3 for 2 hours, and cooling at different rates by water, air, and furnace, they found very minimal difference in the resulting α-lath thicknesses in all three cases. When heat treating the samples at 950°C for 2 hours and cooling with the same three media, they found that the furnace cooled samples with the slowest cooling rates had the largest α-lath thickness and it decreased with increase in the cooling rates with air and water respectively.

It can thus be concluded from this review that the influence of cooling rates is highest at super-transus heat treatments and the influence decreases as the heat treatment temperature decreases.

2.8 Simulation tools for heat treatment design

2.8.1 JMatPro

JMatPro, an acronym for Java-based Materials Properties, is a software developed by Sente Software Ltd. designed to calculate and predict various microstructural and mechanical properties of multi-component alloys based on the materials' physical properties [40]. It covers material properties such as thermodynamic properties, solidification phases, mechanical properties like creep and strength, phase equilibria, TTT/CCT diagrams, martensite start and finish temperatures, tensile and yield stress, hardness, stress/strain diagrams, etc. Due to this wide-ranging property calculation feature embedded in the software, it can be used as an effective tool for the design of heat treatments for various alloys ranging from steels, nickel-based alloys to titanium alloys, to get a good understanding of what the resulting properties can be for the exact composition of the chosen alloy.

For the relevance of this thesis work, only the features of the software that predicts the volume fractions of the phase during isothermal heat treatments and cooling will be reviewed.

JMatPro uses a combination of theoretical models and property databases for its thermodynamic calculations and predictions of material properties. Sauders et al. [41] reviewed JMatPro's approach to calculating material properties exclusively for titanium alloys and postulated that the model used by the software for the calculation of TTT/CCT diagrams and the phase fraction evolution during solid-state phase transformations was the well-known Johnson-Mehl-Avrami (JMA) equation (1) which can be expressed as:

$$x = 1 - \exp(-kt^n) \quad (1)$$

Where x is the amount of material transformed in mole fraction, k is an empirically evaluated constant for the respective study temperature after time t and n is called the Avrami constant which is also an empirically evaluated constant which takes a value between 1 and 4.

During calculation of phases during cooling from isothermal conditions, JMatPro predicts the martensite start (Ms) temperature from the instantaneous β-phase composition, which changes during cooling in conjunction with the formation of the α-phase which is linked to the 'Step Temperature' calculation model. Once this Ms is reached, the remaining β-phase transforms to α'.

2.8.2 ThermoCalc

ThermoCalc is another software that calculates and predicts various material and mechanical properties of multi-component alloy systems. It has a wide range of dedicated databases for alloys of ferrous, nickel, aluminium, and titanium, among many others. It uses the CALculations of PHAse Diagrams (CALPHAD) approach for the calculation and prediction of thermodynamic properties such as phase equilibria and diffusion-controlled phase transformations as called Diffusion Controlled TRAnsformation (DICTRA) simulations in the software. The CALPHAD approach models material properties as a function of temperature, alloy composition and sometimes pressure. This is used to also generate material-specific databases which are of two types: thermodynamic database which includes properties like thermal conductivity, and mobility database which includes transformation kinetics.

Figure 15 is the schematic methodology of the CALPHAD method used by ThermoCalc. The first step is the collection of experimental data of the material system being analysed. Then comes the critical assessment of the collected data and pre-processing to select the best suitable model, based on critical thermodynamic properties such as the Gibbs free energy values, which is sometimes done by material experts manually. This selected model is then optimized using human knowledge and judgement at various stages so as to ensure that the extrapolated data is consistent with the data initially captured in the first step. Once the fitting of the calculated data with experimental data is complete, it is stored in a format accessible by the software. Finally, the predictions are validated against data from commercial multicomponent alloys. This then completes the formation of a database for the specific alloy system which is then used for further calculations of thermodynamic and kinetic properties of the input material [42].

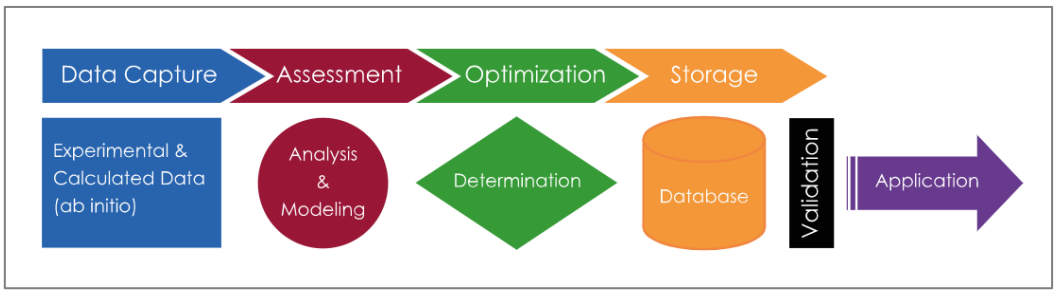


Figure 15. Schematic representation of the CALPHAD method used by ThermoCalc [42]

3 METHODS

3.1 Simulations

In both JMatPro and ThermoCalc, the $\beta_{transus}$ temperature of the exact Ti64 powder composition used in the LMD of experimental samples being studied (Table 5) was calculated. Then, with the powder composition pre-defined, to understand the phase fraction predictions of the α and β phases as a function of heat treatment temperature upon equilibrium cooling from the fully β-phase region above the $\beta_{transus}$, the 'Step Temperature' plot was generated in JMatPro and the 'One Axis Equilibrium' plot was generated in ThermoCalc.

3.1.1 JMatPro

All simulations made in JMatPro were done with the exact powder composition pre-defined. First the 'TTT/CCT Diagrams' were plotted from above the $\beta_{transus}$ to understand the prediction of the transformation kinetics during both heating and cooling during heat treatment. β grain size for the TTT/CCT diagrams were set to 200μm based on the reported average grain size for LMD-p Ti64 [27].

Using the 'Cooling Phases' tool in the software, the evolution of α, β and α' phases upon a set of cooling at rates of and during equilibrium cooling from heat treatment temperature above $\beta_{transus}$ was plotted. Further, using the same tool, the critical cooling rate for α' formation during cooling from different heat treatment temperatures of were studied for different β grain sizes of 50μm, 100μm, 200μm, 300μm, 400μm and 500μm. This set of β grain sizes were chosen since LMD-p Ti64 typically has varying individual grain sizes across the build in the longitudinal direction. For all these heat treatment temperatures and β grain sizes, JMatPro's predictions of the α' martensite start (M_s) and finish (M_f) temperatures were also studied and plots to understand the correlation between them were made.

3.1.2 ThermoCalc

The tool in ThermoCalc most relevant for this thesis work, apart from the 'One Axis Equilibrium' tool as mentioned in the start of this section, was the diffusion simulation tool called 'DICTRA'. This is basically a tool which predicts the phases upon cooling during heat treatment that are diffusion-controlled only, which are the α and β phases, and not the phases that are formed by diffusion-less transformation such as α'. Therefore, only the α-phase fraction formed during cooling from heat treatment temperature above $\beta_{transus}$ at different cooling rates A, B, C, D and during equilibrium cooling were simulated. The software predicts the remaining phase-fraction to be the β-phase.

At the start of the DICTRA simulation module, while defining the elements in the 'System Definer' segment, only Ti, Al and V were selected. This is because the simulation module is not yet fully developed

for simulations with more than three elements. All simulations were run using the TCTI3 database which is designed for titanium alloys.

Unlike JMatPro, ThermoCalc does not have a direct feature for the simulation of phases or material properties as a function of cooling rates during heat treatment. The cooling rates were hence defined in the 'Thermal Profile' section of the simulation module by choosing the 'non-isothermal' option and editing the thermal profile by setting the 'time' and 'temperature' values according to the desired cooling rate. For example, if the cooling rate being studied was X, then to simulate the α-phase fraction being formed during cooling from 1000°C at that cooling rate, the thermal profile set is shown in Figure 16. The start temperature of 1000°C, which is above $\beta_{transus}$, and end temperature of 600°C, below which negligible phase transformations occur, were kept constant for all simulations. Only the end time (48s in Figure 16) was changed for the different cooling rates.



Figure 16. Thermal profile set in ThermoCalc's DICTRA module for α-phase fraction simulations from heat treatment temperature of 1000°C at a cooling rate of X.

3.2 Experimental samples

Two sets of experimental samples were built in a TRUMPF TruLaser Cell 3000, using the same process parameters according to GKN Aerospace standards. As mentioned in the scope of the thesis, the process parameters and powder characteristics will not be discussed due to confidentiality. The samples were built on a forged Ti64 substrate and were then cut by waterjet cutting to the final experimental sizes, as shown schematically in Figure 17.

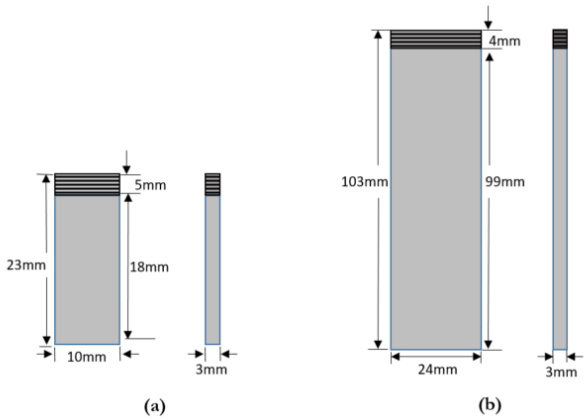


Figure 17. Schematic LMD-p Ti-6Al-4V samples with dimensions of (a) small sample and (b) big sample. The top shaded region of each sample indicates the build region and bottom unshaded region is the substrate.

The reason for using samples of different sizes was due to difficulties controlling the cooling rates during heat treatment of small samples. The cooling rates could be controlled much better with the big samples.

3.3 Heat treatment

3.3.1 Local heat treatment setup

All samples were locally heat-treated with an induction heating coil as schematically shown in Figure 18.

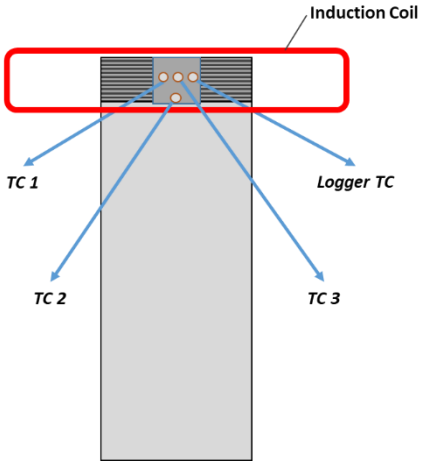


Figure 18. Schematic of local heat treatment setup.

Three thermocouples (TC) were attached to the samples to monitor the temperatures, namely TC 1, 2 and 3 as shown in Figure 18. The logger TC was attached to a National Instruments USB-TC01 temperature logger with 1 Hz (once per second) logging frequency connected to a separate computer. Temperature readings from this logger was used for calculating the exact cooling rates starting from the heat treatment temperature down to 550°C.

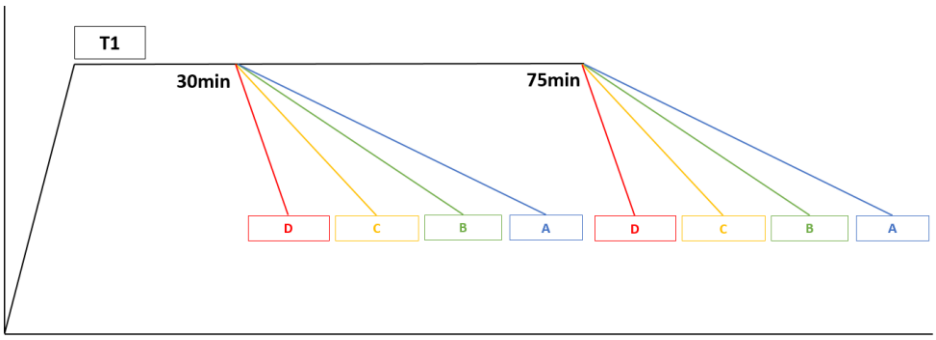
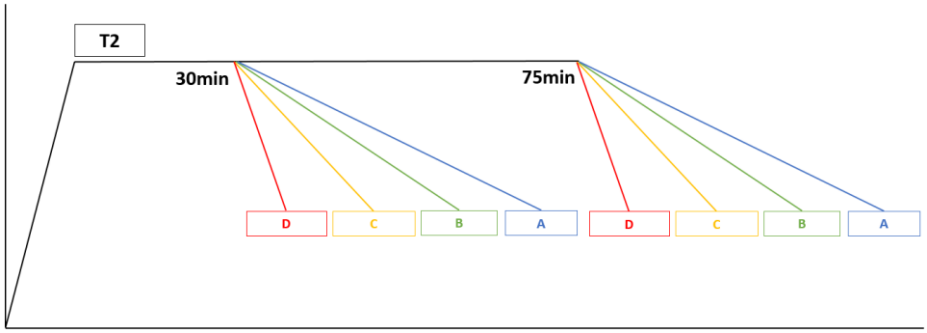
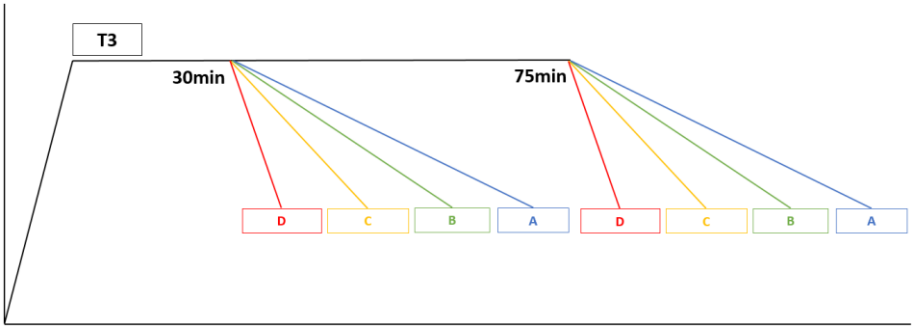
3.3.2 Heat treatment design

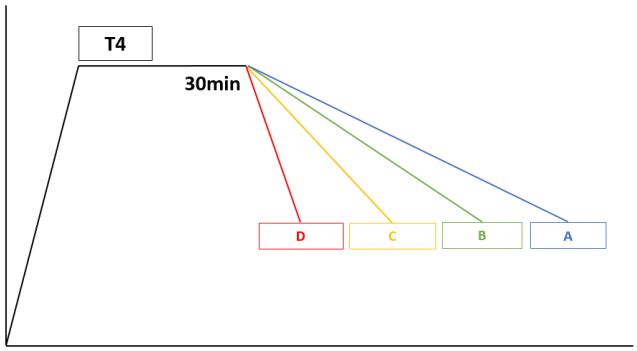
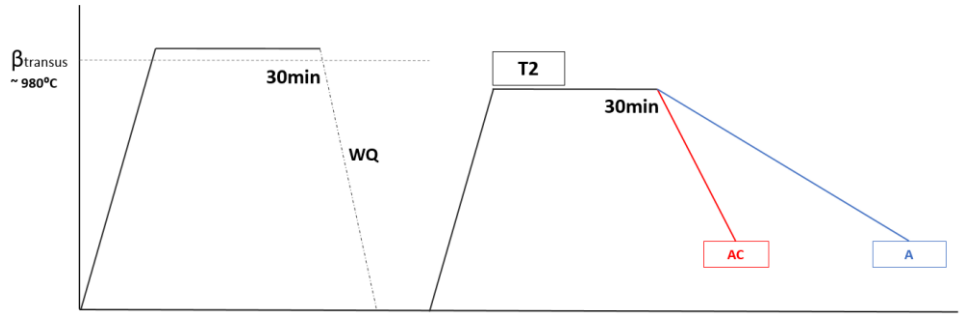
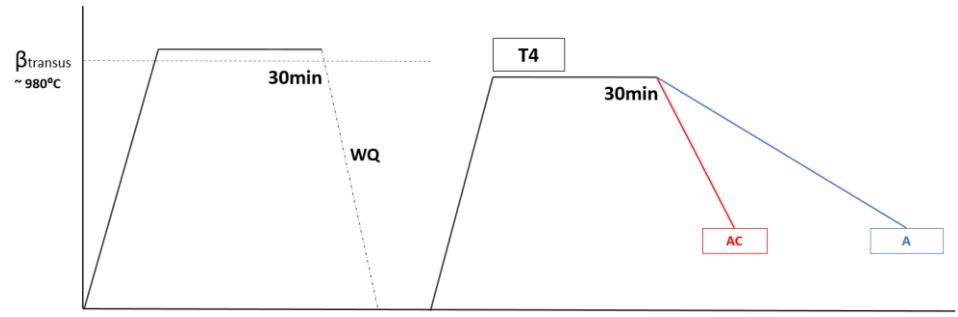
The heat treatments were carried out with a combination of four temperatures, T1, T2, T3 and T4, two holding times of 30 minutes and 75 minutes, for four cooling rates: A, B, C and D. It is important to note that the heat treatment temperatures are of the order T1<T2 <T3 <T4 and the cooling rates of the order A<B<C<D. As mentioned in the previous section, the cooling rates were calculated from the respective heat treatment temperature until the temperature dropped to 550°C as there is no significant phase transformations occurring in Ti64 below that temperature during cooling. The cooling rates of A, B and C were achieved in a controlled manner by programming the furnace to cool down from the heat treatment temperature to 550°C in a particular amount of time. The D cooling rate could not be achieved in such a controlled manner. Hence for this cooling rate, the furnace was shut-off and the sample was allowed to cool in air and the exact cooling rate from heat treatment temperature down to 550° was calculated.

The heat treatments were grouped into six categories as HT groups 1-6 as shown in Table 6 along with the schematics of each heat treatment cycle. HT groups 1-3 were performed at three heat treatment

temperatures, each for two holding times of 30 minutes and 75 minutes and for all four chosen cooling rates. This was designed to study the influence of cooling rates at each of those temperatures and holding times. HT group 4 was performed to study the influence of cooling rates from a higher temperature which is closer to the estimated $\beta_{transus}$ temperature of ~980°C, which was done based on the $\beta_{transus}$ predictions of the simulation tools which will be presented in section 4.1. HT groups 5 and 6 were designed to study the influence of cooling rates on samples pre-solutionized above $\beta_{transus}$, called β-solutionizing, and subsequently heat-treated at two heat treatment temperatures, T2 and T4 for 30 minutes each and cooled at two different rates each: A and air-cooled (AC).

Table 5. Heat treatment cycles with schematics

HT group 1	
HT group 2	
HT group 3	

HT group 4	
HT group 5	
HT group 6	

All samples in HT groups 1 to 4 were heat-treated locally. Samples subjected to HT groups 5 and 6 were first heat-treated in a closed Nabertherm muffle furnace for the β-solutionizing treatment and subsequently heat-treated locally for further heat treatments.

A reference sample was kept aside in the as-solutionized state, with the heat treatment schematically shown in Figure 19 without any further heat treatment and the analysis of this as-solutionized condition will also be presented and discussed.

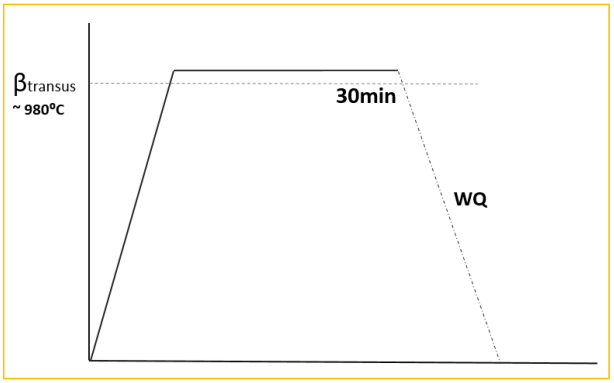


Figure 19. Schematic representation of the β-solutionizing heat treatment.

3.4 Sample preparation

3.4.1 Cutting and mounting

Heat-treated samples were cut and mounted as schematically shown in Figure 20, in both the longitudinal direction and transverse direction, in order to study the anisotropy, if any, after heat treatments.

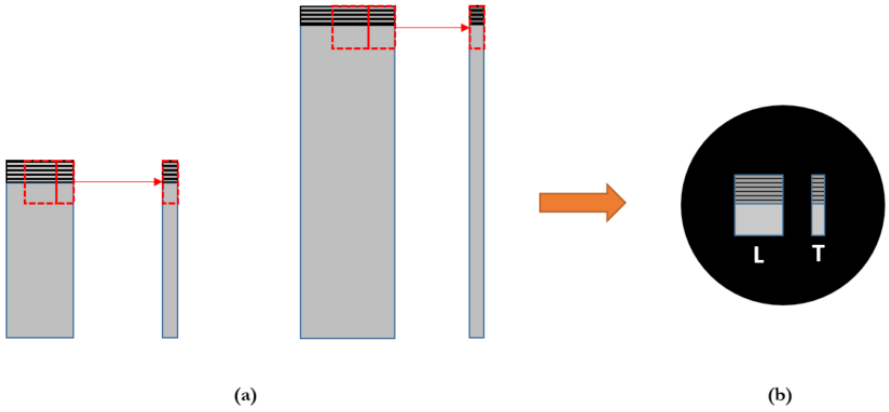


Figure 20. Schematic of the cutting and mounting of samples. Red lines in (a) indicate the cutting lines. In the mount (b), L and T indicate the Longitudinal and Transverse profiles respectively.

The cut samples were mounted with a Struers CitoPress-30 mounting machine according to the Struers' recommended settings, in 'Polyfast' mounting material which is conductive and allows for the mounts to be analysed under SEM.

3.4.2 Grinding, polishing, and etching

All mounts were ground and polished as per the steps listed in Table 6.

Table 6. Grinding and polishing steps.

Surface	**Suspension**	**Lubricant**	**Time** or **µm**
Grinding stone #150	-	Water	400 µm
Grinding stone #150	-	Water	00:30
Grinding plate #500	Diamond 9 µm	DP-lubricant	01:35
Grinding plate #1200	Diamond 9 µm	DP-lubricant	01:35
Polishing cloth	Fumed silica 0.25 µm	Water	03:15

After grinding and polishing, the samples were etched with Kroll's reagent (1% HF, 6% HNO_3, 93% H_2O) by swabbing with a cotton swab for 20-40 seconds.

3.5 Material Characterisation

3.5.1 Microscopy

All samples were analysed with a Zeiss Axioscope 7 Light Optical Microscope (LOM) both in the un-etched and etched condition.

In the un-etched condition, defects such as gas porosities and LoF pores were observed and measured. The LOM's in-built image processing software was used for manually measuring the size of pores and LoF pores.

In the etched samples, the general overall microstructure before, in the as-built condition, and after heat treatments were analysed, along with measurements of the α-case. Microstructural features such as regions of α' and α+β morphology were studied. The LOM imaging of etched samples was performed according to the methodology shown in Figure 21 (a) and (b). In order to cover the whole sample, images of magnifications 50X, 200X and 500X were captured in the top (T1-T3), middle (M1-M3) and bottom (B1-B3) of the build, across the interface (I1-I3) and in the substrate (S1). This was done on both the longitudinal and transverse profiles. As for the α-case, the in-built software was used for manually measuring the α-case thickness across the surface of the build and substrate, an example of which is shown in Figure 21(c).

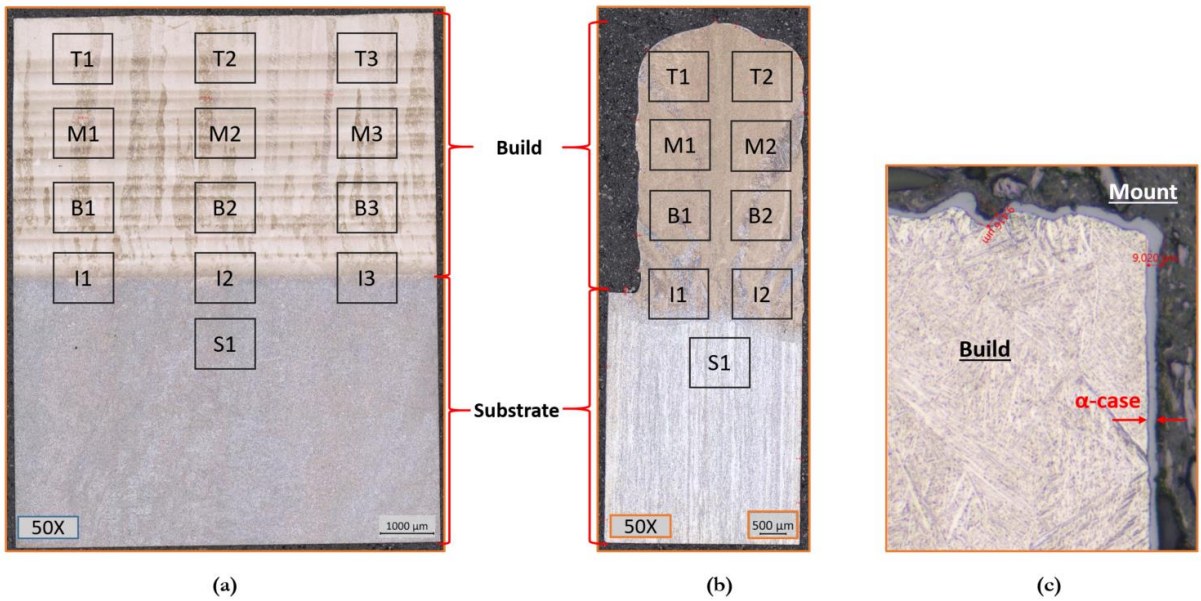


Figure 21. (a) and (b): LOM imaging methodology for overall microstructure analysis of etched samples. (c): α-case measurement.

Microstructural imaging was also done with a Field Emission Gun SEM (FEGSEM). A similar methodology used for LOM imaging was followed for capturing microstructure images in the SEM as well, but with higher magnifications such as 1kX, 2kX, 3kX and 5kX. In some samples, the gas porosities, LoF pores and α-case were also measured in the SEM, examples of which are shown in Figure 22.

In all samples, as-built and heat-treated, microstructural features such as α' regions, α+β morphology and α-lath thickness evolution were analysed under the SEM.



Figure 22. Images of (a) gas porosity as seen under SEM, (b) LoF pore seen under LOM and (c) α-case seen under SEM.

Further, an Energy Dispersive X-Ray Spectroscopy (EDS) was carried out in the SEM to determine the chemical composition of one of the heat-treated experimental samples, an example of which is shown in Figure 23.

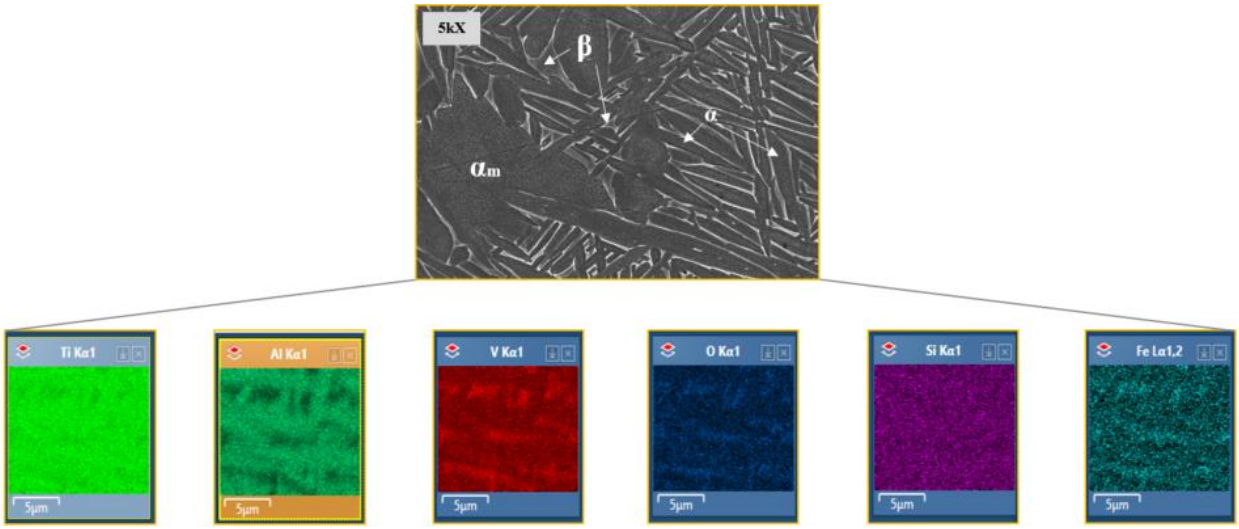


Figure 23. EDS analysis showing presence of Ti and allowing elements (BOTTOM: from left to right) Al, V, O, Si and Fe and the inspected regions of α, massive α (α_m) and β in the SEM image of sample (TOP).

3.5.2 Hardness measurement

All samples' micro-vickers hardness was tested according to ASTM E92-16 standard [43] in a LECO M-400DT Hardness Tester with a load of 300g and the hardness measurements were logged per sample in the Buehler OmniMet MHT 80 software. The method used for location of indents is shown in Figure 24. A total of 15 hardness indents from left to right: seven in the middle of the build, five at the interface and three in the substrate were measured in the longitudinal profile. 9 indents in total from left to right: four in the middle of the build, three at the interface and two in the substrate were measured in the transverse profile.

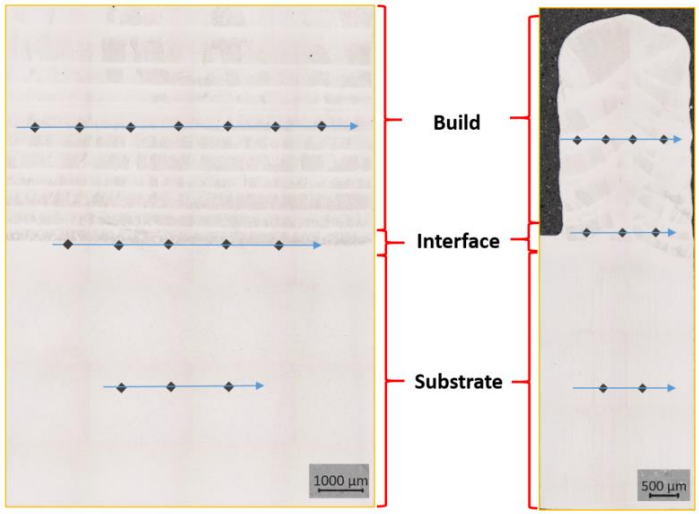


Figure 24. Microvickers (300g load) hardness measurement method of (a) longitudinal profile and (b) transverse profile

3.6 Microstructural image processing

3.6.1 MIPAR

MIPAR is an image processing and analysis software which can be used for measurement of microstructural features in images from either LOM or SEM. It can process images and convert them into two-shade binary images based on the contrast adjustment done manually by the user. The processed binary image can then be used to manually define each shade as a particular phase and calculate the desired features. An example of such an image processed is shown in Figure 25, where the black region is the α-phase, and the white region is the β-phase in Figure 25(b).

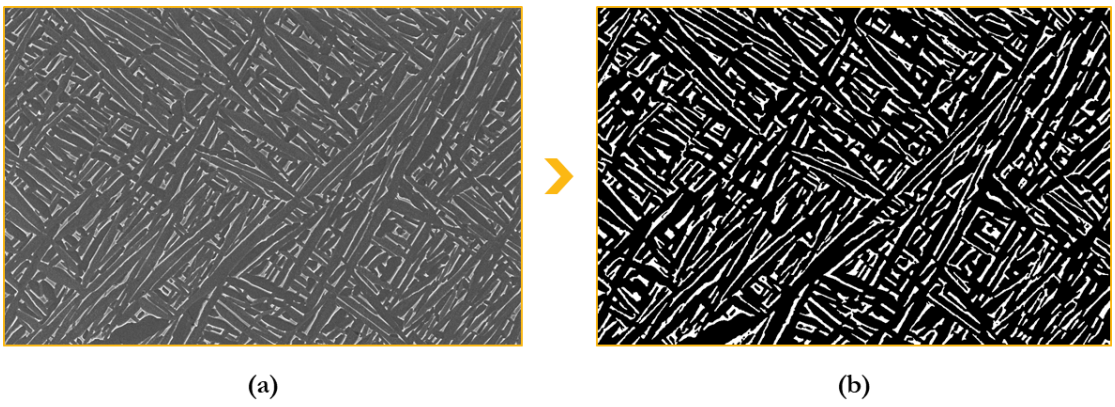


Figure 25. Example of the image processing feature in MIPAR. The input (a) SEM image of 3kX mag. and (b) the processed image by MIPAR. In (2): the black region is the α-phase and white region is the β-phase.

SEM images of magnifications 3k and 5k were used for MIPAR. For each sample, a minimum of three 3k and three 5k images were used for extracting the desired data such as α-lath thickness and α-phase fraction. As mentioned in section 2.7, the most important microstructural feature that correlates with the mechanical properties of heat-treated Ti64 is the α-lath thickness. The α-phase fraction was also measured in MIPAR in order to compare the results of the experimental values to those simulated by JMatPro and ThermoCalc.

3.6.1.1 α-lath thickness measurement

Measurement of α-lath thickness was performed based on the work done by Collins et al. [44]. Since the α-laths are typically distributed in different orientations based on the microstructural morphology, the most accurate way of obtaining the actual lath thickness is by using probability density functions. For this, an initial assumption that the α-laths are infinitely long in two directions and finite in one direction. Then, the actual mean lath thickness can be calculated by measuring the intercept of a line over the laths, across the plane captured by the SEM image, using equation (2) [44]:

$$thickness = \left[\frac{1}{1.5\left(\frac{1}{\lambda}\right)_{mean}}\right] \quad (2)$$

Where λ is the intercept measured over the laths.

In MIPAR, the measured intercepts in equation (2) were set to 1000 lines rotating at intervals of 10^{0} for 180^{0}. This measurement can be saved as a 'recipe' in MIPAR and can be used for the processing and measurement of α-lath thickness of many SEM images without having to adjust the settings repeatedly for each new image. Since the images processed were all not of the same heat treatment parameters, the size, distribution, and fractions of the α-phase varied for samples subjected to different heat treatments. Hence, the recipes were tweaked and saved for samples with different heat treatment temperatures and image magnifications, based on visual judgement of the quality and accuracy of the processed image to its original SEM image.

3.6.1.2 α and β phase fraction measurements

Once the selected SEM image was processed in MIPAR with the most suitable recipe, the α-phase fraction was measured as the mean area of the black region, as seen in Figure 25 (b), in the whole processed image. It is then assumed that the remaining mean area fraction, the white region, is the phase fraction of the β-phase, measured as in equation (3):

$$\beta_{phase\ fration}\ \% = \left(100 - \alpha_{\ phase\ fraction}\right)\% \quad (3)$$

3.6.2 NIS-Elements

NIS-elements is also an image analysis software used for editing and measuring microstructure images from either LOM or SEM. In this thesis work, it was used for the measurement of the prior β-grain sizes from LOM images of etched as-built and heat-treated samples. The β-grain size is another key microstructural feature since it has a limiting effect on the size of α-colonies that can be formed within the grain [31]. Hence, larger the β-grains, more is the potential for the formation of larger α-colonies, which in-turn affects the resulting mechanical properties; wherein larger the α-colony size, bigger will be the α-lath thickness and lower will be the strength [29].

3.6.2.1 β-grain size measurement

β-grain sizes of etched as-built and heat-treated samples were done in NIS-Elements AR version using LOM images of 50X magnification of the longitudinal profile. The measurements were done according to ASTM E112-13 standard using Heyn's Lineal Intercept method which is recommended for measuring elongated grains [45]. As seen in Figure 26, a total of five lines were manually drawn covering the whole build and the number of grains lying on each line, or the intercepts, were measured and the average grain size of the sample was then calculated using equation (4):

$$Average\ \beta_{grain\ size}\ (in\ \mu m) = \frac{Total\ length\ of\ lines}{Total\ no.\ of\ intercepts} \quad (4)$$

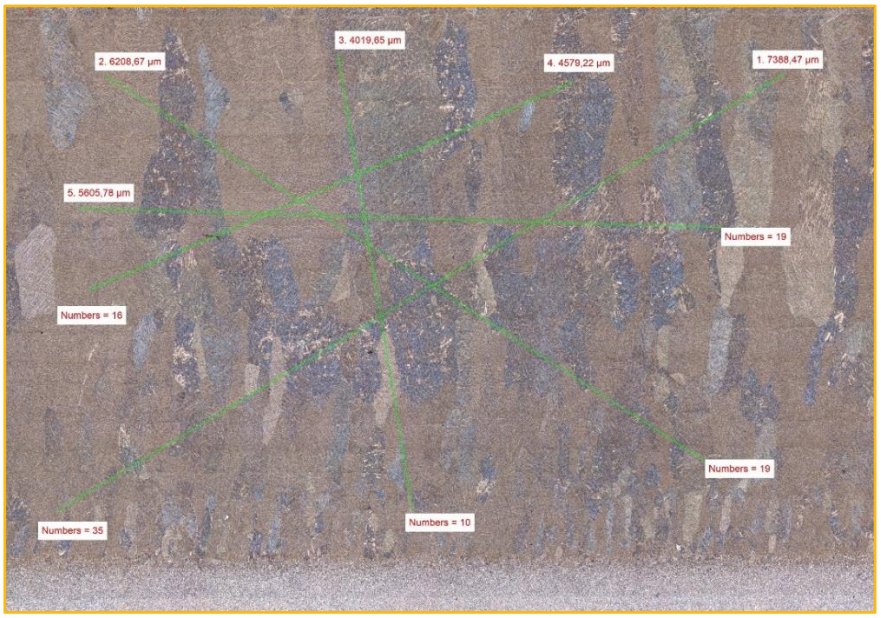


Figure 26. Example of β grain size measurement by ASTM E112-13 standard in NIS Elements AR. Green lines indicate the lines for measuring the intercepts, with the length of each line on one end and the number of intercepts on the other.

4 RESULTS AND DISCUSSION

4.1 Simulations

Results from simulations made in JMatPro and ThermoCalc will be presented in this section along with discussions on its interpretations.

4.1.1 JMatPro

JMatPro predicted the $\beta_{transus}$ to be 970°C. The step temperature plot for heat treatment above $\beta_{transus}$ at 1000°C is shown in Figure 27. This plot gives information on how much of what phases are present at different temperatures at equilibrium condition. The phases of interest are the α and β phases. The intermetallic 'Ti3Al' phase simulated here can be ignored since all of the chosen heat treatment temperatures in the experimental plan are above its complete dissolution point of 600°C. It can be seen that at increasing temperature, the α-phase fraction reduces and β-phase fraction increases, with the two phase fractions reaching 50% each around 890°C and the β-phase fraction reaching 100% at the $\beta_{transus}$ of 970°C.

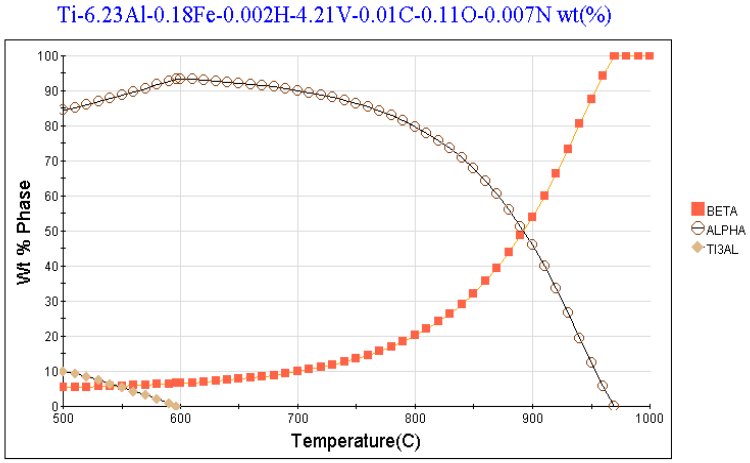


Figure 27. Step temperature plot from JMatPro showing the wt. % of phases formed as a function of heat treatment temperature from 1000°C during equilibrium cooling.

The TTT and CCT plots for 0.1% number and amount of phases transferred from 1000°C is shown in Figure 28 (a) and (b) respectively.

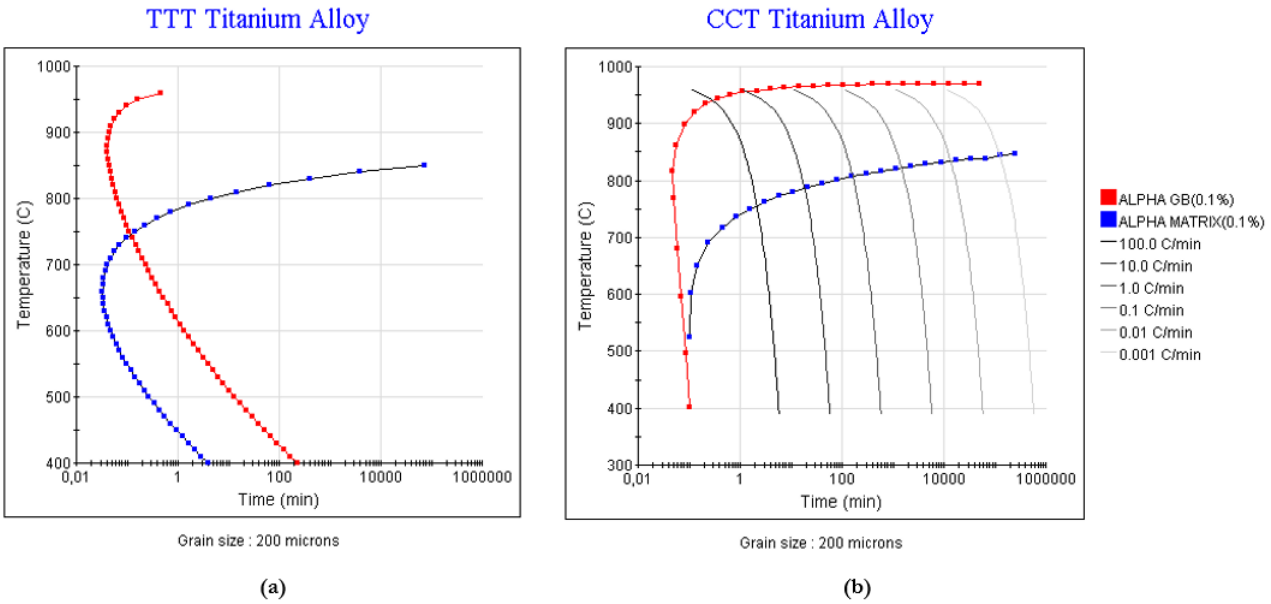


Figure 28. (a) TTT diagram and (b) CCT diagram from JMatPro for grain size 200μm and start temperature 1000°C.

Figure 29 shows the JMatPro simulation results for the amount of α-phase fraction formed during cooling from heat treatment temperature of 1000°C at different cooling rates. The Ms line indicates the α' start temperature for the cooling rates from 1000°C/min to B. JMatPro predicts no α' formation at equilibrium condition and for cooling rate of A, since this cooling rate is lower than the minimum rate required for its transformation. Further, the amount of α-phase fraction reduces as the cooling rate increases since the tendency for the formation of α' is preferred instead at high cooling rates.

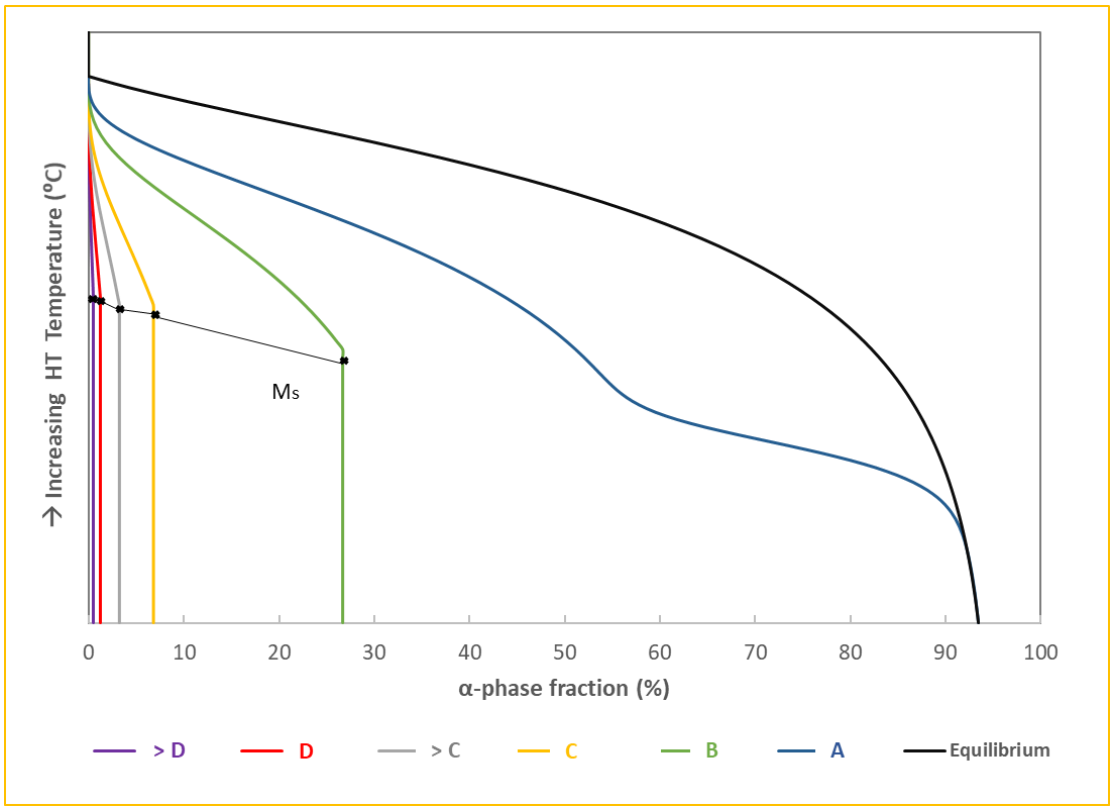


Figure 29. JMatPro simulation results showing the influence of cooling rates on α-phase fraction from heat treatment temperature of 1000°C.

The plots of critical cooling rate for α' formation during cooling from heat treatment temperatures of 1000°C down to T1 as a function of the varying β grain sizes are attached in Appendix A. At higher heat treatment temperatures, this critical cooling rate for α' is extremely sensitive to the β grain size, reducing with an increase in grain size. At heat treatment temperature above $\beta_{transus}$, at 1000°C, the critical cooling rate for α' reduces significantly with increasing grain size. At heat treatment temperatures below $\beta_{transus}$, between T4 and T1, the trend is similar, albeit not as significant. At the lowest chosen heat treatment temperature T1, the critical cooling rate for is constant for all grain sizes.

The M_S and M_f temperatures during cooling from the same five heat treatment temperatures at the respective critical cooling rate for α' for the varying β grain sizes were plotted to study the correlation between them. The plots are attached in Appendix B. At temperatures of 1000°C, T4 and T1 the M_S temperature increases with an increase in β grain size. For heat treatment temperature of T3, the M_S temperature remains constant for grain sizes 50μm, 100μm and 200μm and increases for grain sizes 300μm, 400μm and 500μm. For heat treatment temperature of T2, the M_S temperature shows a decreasing trend for grain sizes 50μm to 200μm and then an increasing trend for grain sizes 300μm to 500μm.

As reviewed in section 2.8.1, JMatPro simulates the α' phase from the instantaneous β-phase composition, which changes during cooling in conjunction with the formation of the α-phase. This α-phase is simulated as a combination of α-grain boundary (α_{GB}), which is the amount of α-phase nucleated on the β grain boundary, and α-matrix, which is the amount of α-phase inside the β grain. Varying the β grain size affects the amount of α_{GB} – higher the grain size, lesser will be the grain boundaries available for α_{GB} nucleation and vice-versa. Hence for large β grain sizes, the amount of total α-phase (α_{GB} + α-matrix) will be predicted to be lesser, favouring the transformation of the higher instantaneous β-phase to α' at much lower cooling rates.

Further, in JMatPro, the M_S temperature depends on the amount of β-phase stabilizing V. Factors such as low heat treatment temperatures, low cooling rates and small β grain sizes favour the formation of the α-phase, resulting in the remaining β-phase to become more stabilized by the enrichment of V, reducing the M_S temperature consequently.

4.1.2 ThermoCalc

The $\beta_{transus}$ predicted by ThermoCalc was 976°C. The One Axis Equilibrium plot is shown in Figure 30. Similar to JMatPro's Step Temperature simulation, at increasing temperatures, the α-phase fraction reduces and β-phase fraction increases. At around 890°C, the two phase fractions reach 50% each. At 976°C and above, only the β-phase is predicted to be present.

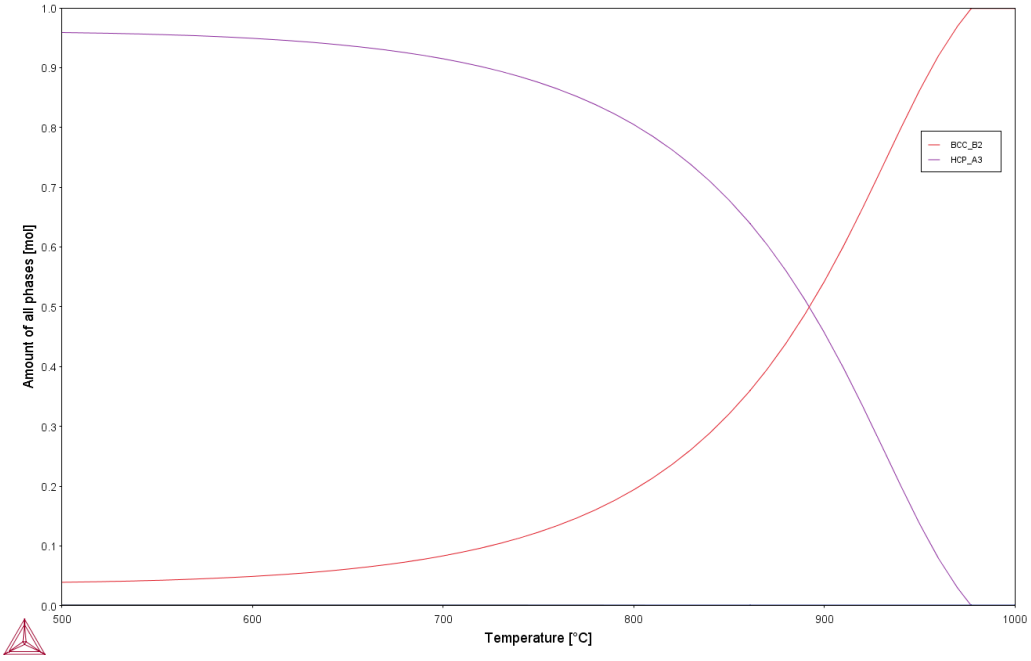


Figure 30. One axis equilibrium plot from ThermoCalc showing the amount of phases (in mol.) formed as a function of heat treatment temperature from 1000°C during equilibrium cooling. BCC_B2 is the β-phase and HCP_A3 is the α-phase.

The results of the DICTRA simulations performed for the amount of α-phase fraction formed from heat treatment temperature of 1000°C during cooling at different rates is shown in Figure 31. It is seen that the amount of α-phase fraction reduces with an increase in the cooling rate. This is because at higher cooling rates, the amount of α' formation from the remaining β-phase increases by the diffusion-less mechanism which is not predicted by ThermoCalc's DICTRA module.

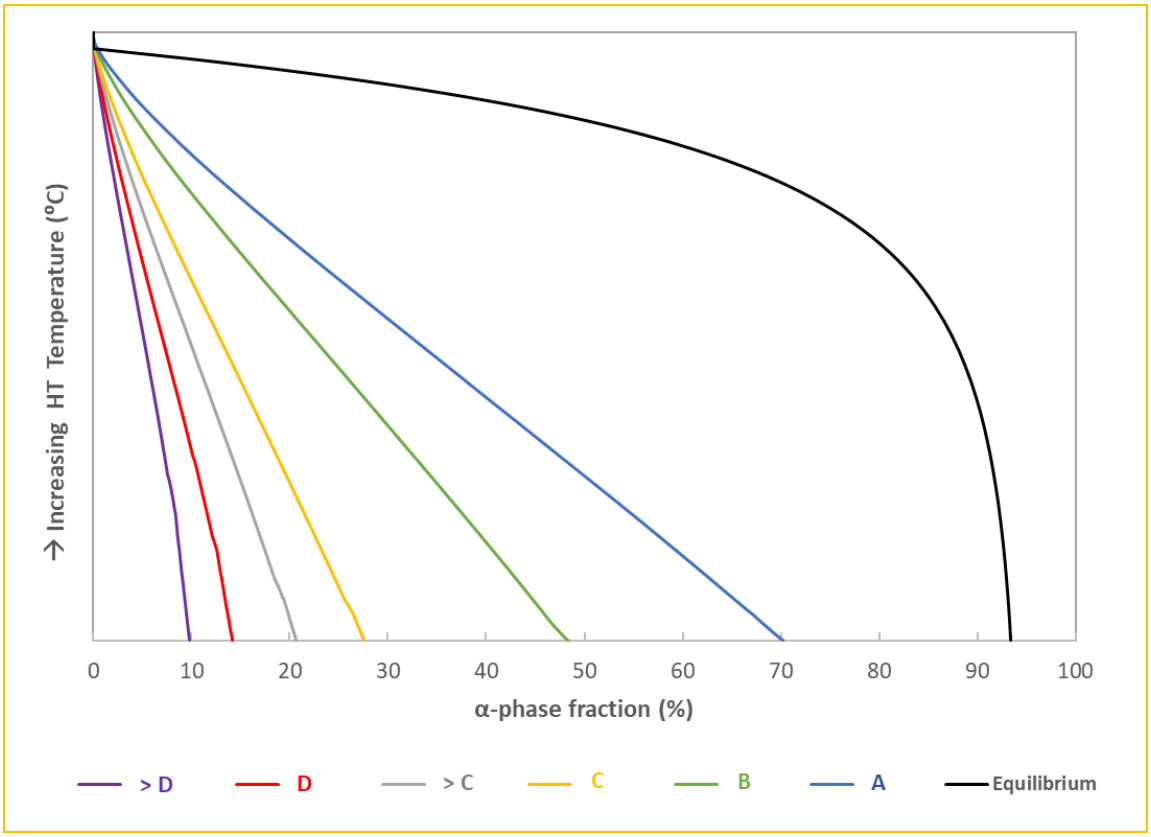


Figure 31. ThermoCalc simulation results showing the influence of cooling rates on α-phase fraction during cooling from heat treatment temperature of 1000°C.

4.1.3 JMatPro vs ThermoCalc

The prediction of the $\beta_{transus}$ temperature by both softwares for the powder composition was nearly the same: JMatPro predicted it to be 970°C and ThermoCalc, 976°C. In order to make a comparison between the simulation results of the α-phase fraction predicted by JMatPro and ThermoCalc during cooling from 1000°C at different cooling rates, a comparison plot was made as seen in Figure 32. It shows that both software predicts a decrease in α-phase fraction with an increase in cooling rate. Another noticeable similarity between them is that during equilibrium cooling, the amount of α-phase fraction at the lowest temperature is the same. In terms of the dissimilarities in the two software's predictions of the α-phase fraction for the non-equilibrium cooling rates can be attributed to their modelling capabilities. JMatPro has the in-built model for the prediction of the α' phase which is formed by the diffusion-less mechanism, whereas the diffusion-based DICTRA simulation tool in ThermoCalc does not show the formation of this α' phase and hence assumes that the transformed β-phase during heat treatment remains untransformed. Another possible reason behind the gaps in prediction by the two software could be that the JMatPro simulations were performed with the exact Ti64 powder composition including all alloying elements whereas the DICTRA simulations in ThermoCalc were performed with just three elements namely Ti, Al and V.

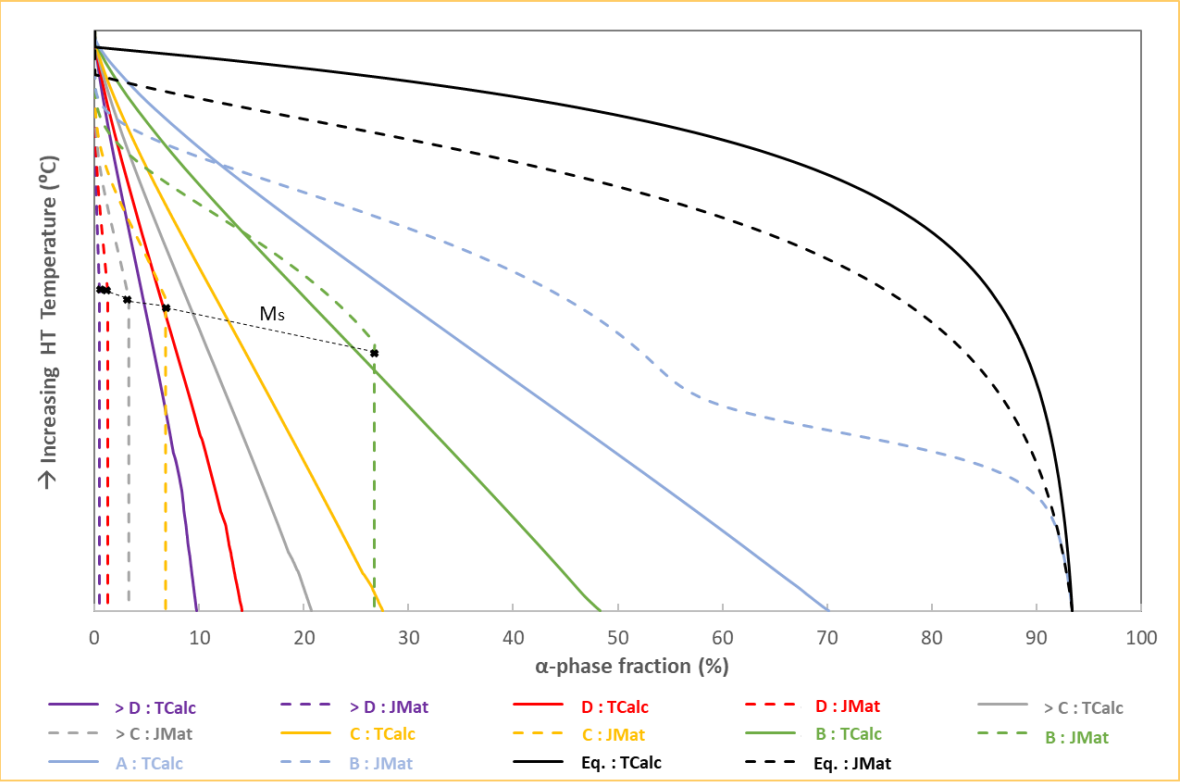


Figure 32. Comparison plot for JMatPro (dashed lines) and ThermoCalc (solid lines) simulation results showing the influence of cooling rates on α-phase fraction during cooling from heat treatment temperature of 1000°C. Ms indicates the α' start temperature from JMatPro shown by the small black dotted line.

4.2 Defects and As-built condition

Findings and analysis results of defects in the samples and β grain size, microstructure, and hardness their as-built condition will be presented in this section.

4.2.1 Defects

The defects observed in all experimental samples in the as-built condition were classified into Gas Porosities and LoF porosities.

4.2.1.1 Gas Porosities

Gas porosities found in all the mounted samples in both the longitudinal and transverse direction, is shown in Table 8.

Table 7. Gas porosities found in all experimental samples

Longitudinal Profile					
Pore size range	25-30 µm	31-35 µm	36-40 µm	41-45 µm	46-50 µm
Count	15	12	8	2	5
Transverse Profile					
Pore size range	25-30 µm	31-35 µm	36-40 µm	41-45 µm	46-50 µm
Count	4	2	1	1	0

4.2.1.2 LoF Porosity

Compared to the number of gas porosities, only two LoF pores were found, both in the longitudinal profile, of sizes 30 µm and 40 µm.

4.2.2 Prior β grain size

The prior β grain size of the as-built sample was measured to be 229±89 µm. This finding is not far from the average grain size reviewed in literature for LMD-p Ti64, which is 202 µm [27].

4.2.3 Microstructure

The as-built microstructure was seen to have elongated β grains in the build direction with a predominantly α' microstructure and very few regions of α+β in both basketweave and widmanstätten morphologies in the build. The LOM images are shown in Figure 33 and the SEM images in Figure 34.

As seen in Figure 33 (c), the interface region had a finer and mixed morphology of α+β. The substrate, as seen in Figure 33 (d) had an equiaxed α+β morphology which is typical of a forged Ti64 plate. Figure 34 (a) and (b) shows the build microstructure viewed under SEM having both α' and α+β regions.

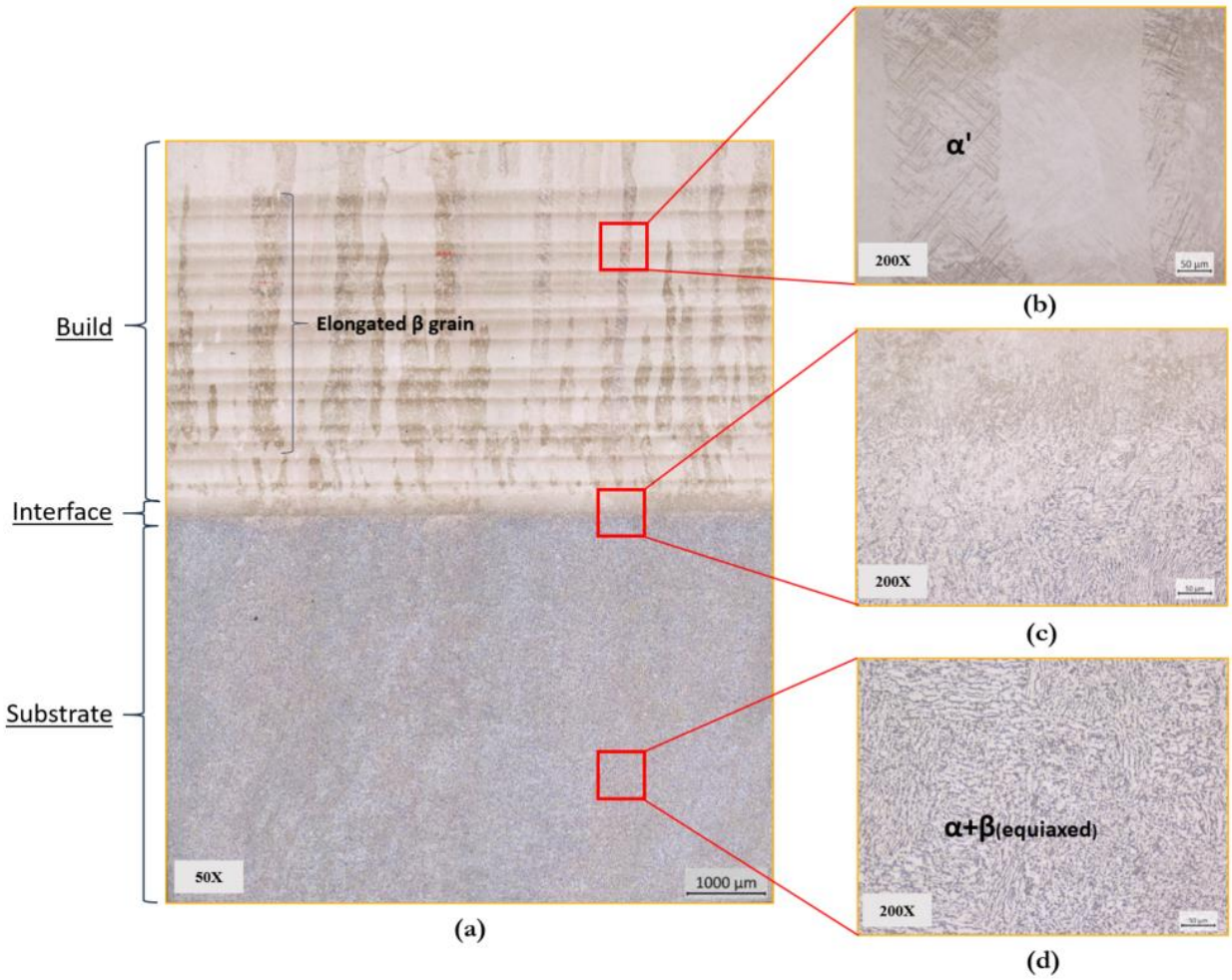


Figure 33. LOM images of the as-built microstructure showing (a) the whole sample with elongated β grains in the build in 50X mag., (b) α' in the build (c) in the substrate and (d) equiaxed α+β in the substrate. Red boxes are indicative of regions only, enlarged images are not to their scale.

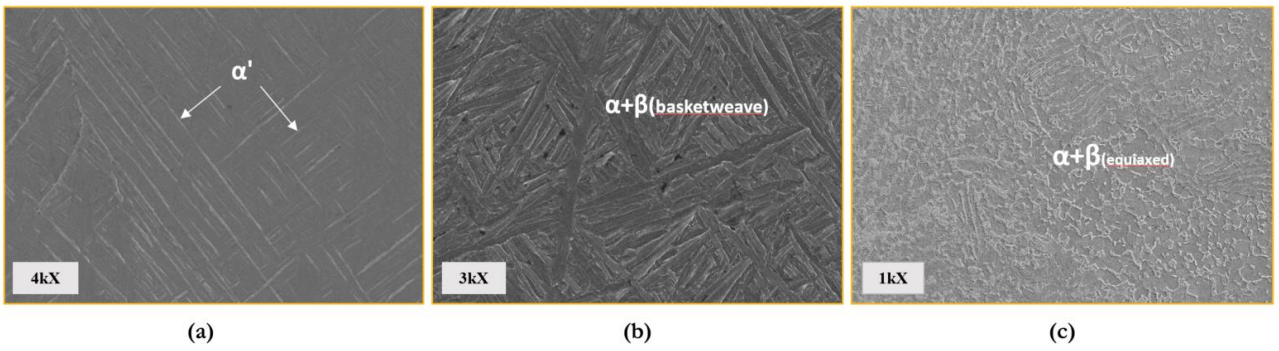


Figure 34. SEM images of the as-built microstructure showing (a) α' and (b) α+β basketweave morphology in the build, and (c) equiaxed α+β in the substrate. In (a), the white needles indicate α'. In (b) and (c), dark regions are α, bright regions are β.

4.2.4 Hardness

The as-built hardness in both the longitudinal and transverse direction at the build, interface and substrate is shown in Table 8.

Table 8. Hardness (in HV0.3) of as-built sample in longitudinal and transverse profile

Longitudinal direction			Transverse direction		
Build	Interface	Substrate	Build	Interface	Substrate
367 ± 2 HV	388 ± 1 HV	338 ± 5 HV	380 ± 1 HV	395 ± 2 HV	331 ± 6 HV

Two key observations can be made here. In both the longitudinal and transverse direction, the interface hardness is higher than the build hardness. This can be attributed to the presence of fine α+β morphologies observed in the interface region as shown in Figure 33(c), leading to higher resistance to deformation as reviewed in section 2.7. The fine α+β region in the interface is also usually accompanied by the presence of high amounts of α' as well, considering the thermal history in the LMD-p process as discussed in section 2.6.2. During the deposition of the first layer on the substrate, the substrate temperature is at its lowest, giving rise to extremely high temperature gradients and cooling rates compared to the deposition of the second layer on the hot first layer. These high cooling rates lead to the preferential formation and accumulation of α' mostly in the interface region separating the once cold substrate and the molten first layer.

The second key observation is the anisotropy of the build hardness in the longitudinal and transverse direction, with the latter having higher hardness. This is something that needs to be studied further in order to understand why. Anisotropy in general mechanical properties has been reviewed by Liu et al. [26] to be commonly found in additively manufactured Ti64 parts and in Ti64 processed by LMD as seen also in the typical mechanical properties shown in Table 4 in section 2.6.4.

4.3 Heat treatments: HT Groups 1 – 4

Findings and analysis results of all the samples subjected to HT groups 1 to 4 will be presented and discussed in this section. The heat treatment temperatures in all the experiments were controlled within ±14°C across all thermocouples and there were no deviations in the holding times. All cooling rates were measured to be the same as the desired values except for the D cooling rate. Since this was done by air cooling, the measured cooling rates were generally higher and could not be controlled. Further, there was no difference found in results between the small samples and big samples. This was verified by subjecting samples from each set to the same heat treatment parameters and comparing the results presented in this section. This rules out the need to mention which sample, small or big, was used in each of the experiments.

4.3.1 Chemical composition

Table 9 shows the chemical composition results from the EDS analysis carried out on one of the heat-treated samples. As discussed in section 2.3.4, the inspected regions of α, α_m and β regions, show high values of the respective α and β stabilizers. The α and α_m phases are both enriched in the α-stabilizer Al and the β-phase is enriched in the β-stabilizer V.

Table 9. Chemical composition of experimental sample from EDS analysis.

Wt. %	**Ti**	**Al**	**V**	**O**	**Si**	**Fe**
α-phase	88.10	6.24	1.49	4.17	-	-
Massive α	87.50	6.70	1.90	3.90	-	-
β-phase	78.04	3.49	13.56	3.51	-	1.40

4.3.2 α-case

The maximum α-case thickness measurements for all samples in both the longitudinal and transverse profiles, split by the measurements done on the build and substrate in each profile. Due to confidentiality agreements with GKN, the individual measurements for each heat treatment will not be discussed. In all heat-treated samples, the overall trend seen is an increase in the α-case thickness for higher heat treatment temperatures and holding times. The minimum α-case thickness measured in the build of samples heat-treated at the lowest heat treatment temperature was 3μm and the maximum, which was found in samples heat-treated at the highest heat treatment temperature, was 100μm. This information is essential for the allowance of appropriate machining after heat treatments in order to avoid the brittle surface affecting the product's in-service performance.

4.3.3 Influence of cooling rate on β grain size

The influence of cooling rates on the β grain size of samples heat-treated for 30 minutes is shown in Figure 35 and the same for samples heat-treated for 75 minutes is shown in Figure 36.

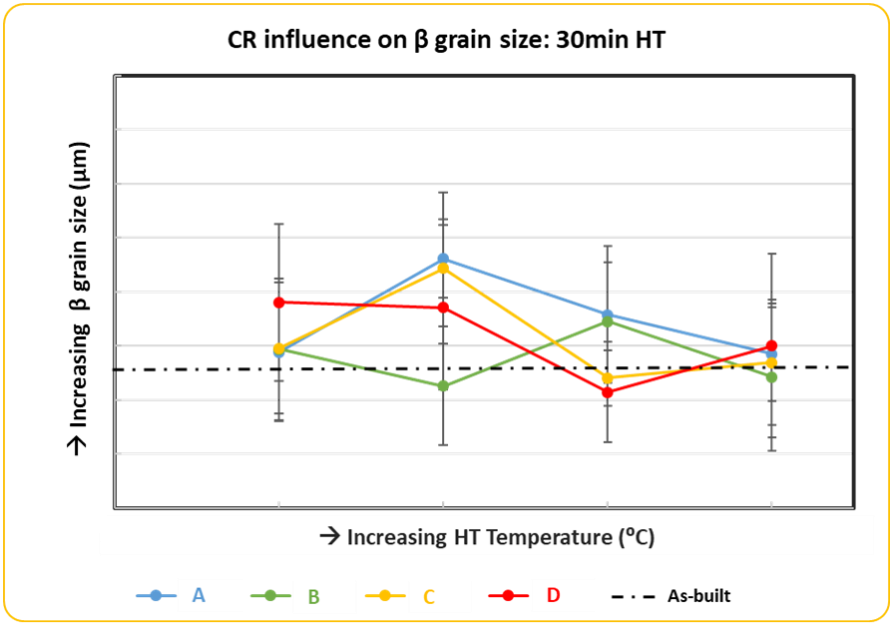


Figure 35. Influence of varying cooling rates on β grain size in the build of samples heat-treated for 30 min. Black dotted line shows the as-built β grain size value.

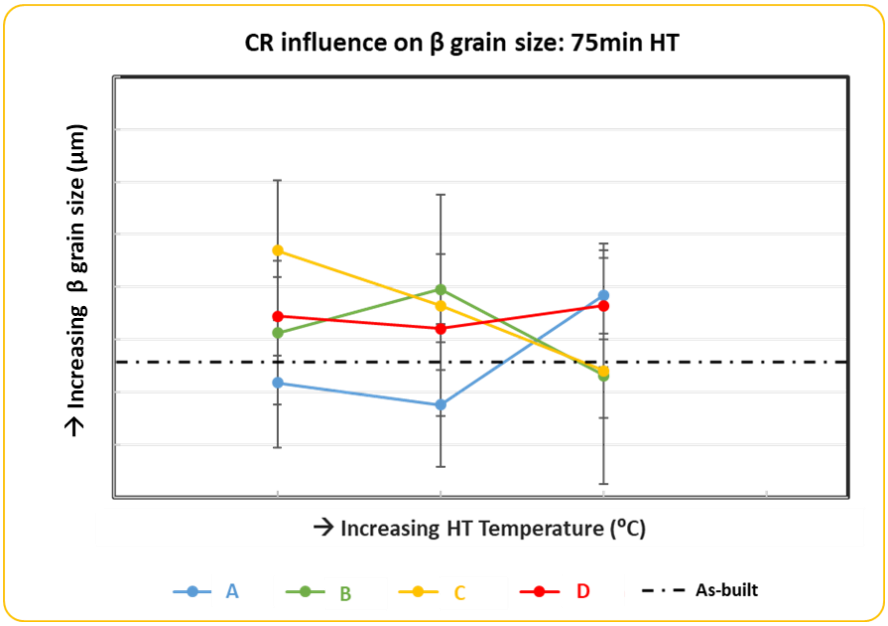


Figure 36. Influence of varying cooling rates on β grain size in the build of samples heat-treated for 75 min. Black dotted line shows the as-built β grain size value.

Upon analysis of the results, it can be inferred that no obvious correlation was found between the different cooling rates on the resulting β grain size of heat-treated samples. For example, for the 30 minutes heat treatment results shown in Figure 35, the B cooling rate gives low grain size for heat treatment at T1, high grain size at T2 and lower grain size at T3 and T4, compared to the other cooling rates, hence showing no particular trend. Similar inconclusiveness was observed in the other cooling rates for heat treatments for 75 minutes as well, as shown in Figure 36. This could be due to factors such as temperature differences in different regions of the sample heat-treated locally and needs further analysis to understand the reasons behind the lack of correlation.

4.3.4 Influence of cooling rates on build microstructure

The influence of cooling rate on the build microstructure when viewed under LOM and SEM was not very straightforward, especially in the samples subjected to HT groups 1 and 2 with the low heat treatment temperatures of T1 and T2 respectively. Only the effect of heat treatment temperature and time on the amount of α' decomposition was noticed in these samples. In samples from HT groups 3 and 4 with temperatures of T3 and T4 however, upon more decomposition of this α', the effect of cooling rates was noticeable, albeit only slightly, under LOM and SEM. As seen in Figure 37 of the LOM images of samples heat-treated at T3 for 75 min and cooled at A and D, there is only a slight noticeable decrease in the α-lath thickness in Figure 37 (b) with the faster cooling rate compared to Figure 37 (a) with the slow cooling rate. The SEM images of the same two samples are shown in Figure 38 (a) and (b), with the slower cooling rate, Figure 38 (a), having α-laths of slightly higher thickness. It can be concluded here that the qualitative observation of LOM and SEM images of samples heat-treated at the same temperature and time conditions but with different cooling rates indicate only slight differences and hence a more thorough quantitative analysis is needed by means of further image processing to fully understand the influence of cooling rates on the build microstructure and its features.

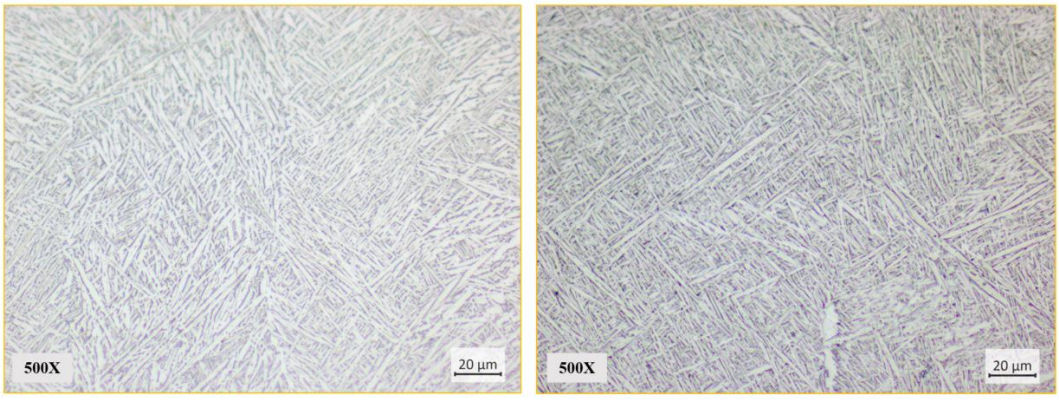


Figure 37. LOM images of the build in samples heat-treated at T3 for 75 min and cooled at rates of (a) A and (b) D. Bright regions are α and dark regions are β. Thickness of the bright laths indicates the α-lath thickness.

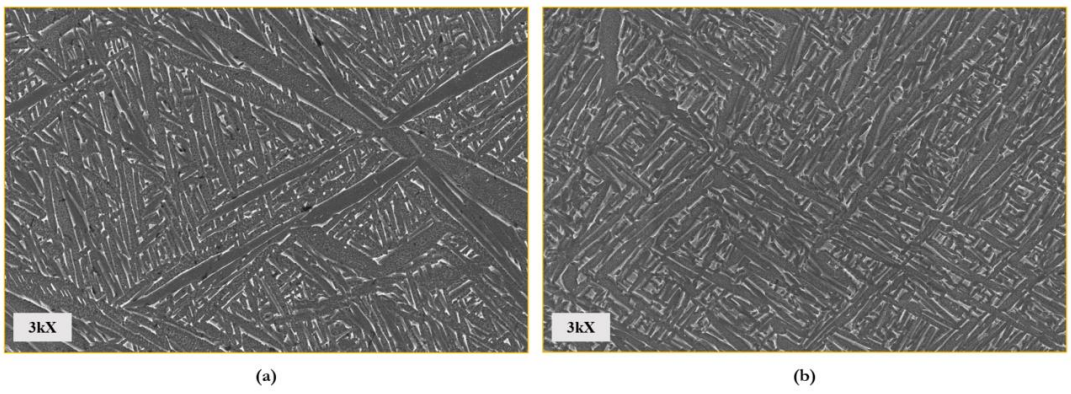


Figure 38. SEM images of the build in samples heat-treated at T3 for 75 min and cooled at rates of (a) A and (b) D. Dark regions are α and bright regions are β. Thickness of the dark laths indicates the α-lath thickness.

4.3.5 Influence of cooling rates on build hardness

The influence of cooling rates on the build hardness in the longitudinal direction of samples heat-treated for 30 minutes is shown in Figure 39 and of samples heat-treated for 75 minutes is shown in Figure 40.

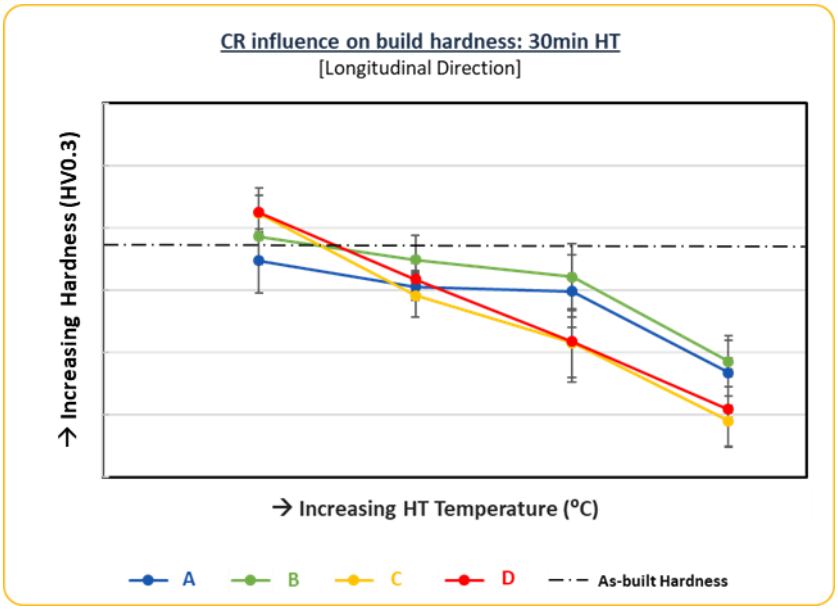


Figure 39. Influence of varying cooling rates on build hardness in the longitudinal direction in samples heat-treated for 30 min. Black dotted line indicates the average as-built build hardness.

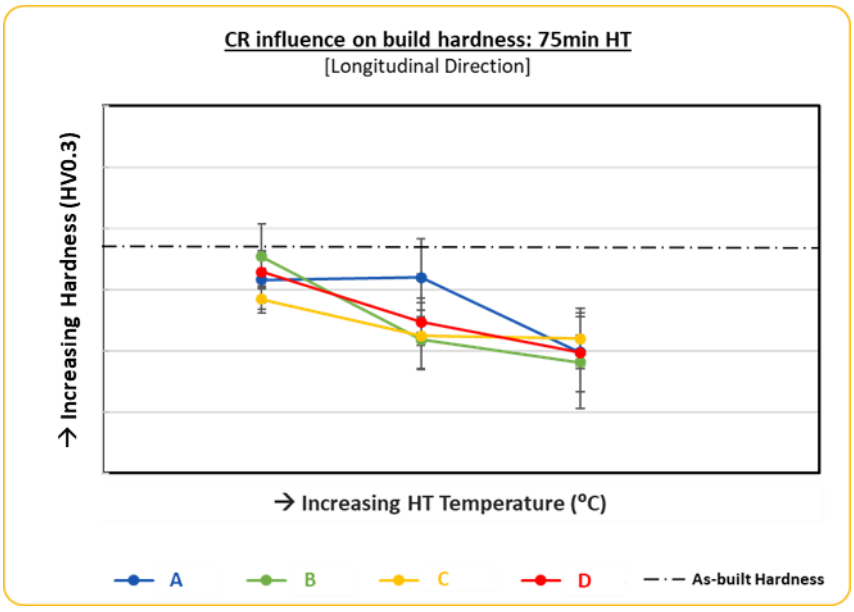


Figure 40. Influence of varying cooling rates on build hardness in the longitudinal direction in samples heat-treated for 75 min. Black dotted line indicates the average as-built build hardness

It can be seen that the overall build hardness of all samples shows a decreasing trend with an increase in heat treatment temperature and time. When it comes to the effect the different cooling rates have on the hardness, there is no such uniform trend seen for any of the four cooling rates in the samples heat-treated for either holding times. For example, in the 30 minutes heat treatment results shown in Figure 39, the C cooling rate gives the lowest hardness at heat treatment temperature of T1, low hardness at T2, higher hardness at T3 and T4, compared to the other cooling rates, indicating no particular trend. Similar lack in

trends were observed for the other cooling rates at heat treatments for 75 minutes shown in Figure 40 as well, giving inconclusive results in terms of a direct correlation between cooling rates and build hardness.

The hardness measurements across the whole sample, covering the build, interface and substrate regions are also studied. It was observed that the hardness at the interface for most samples were higher or the same as the build hardness, needing further study to understand the reason behind it.

As discussed earlier in section 2.7.1, the decrease in build hardness with an increase in heat treatment temperature and time can be correlated with the amount of α' decomposition. More the α' decomposition as a factor of temperature and time, lower should be the hardness, as was the case in the findings of this work.

A lack of a trend or direct correlation between the cooling rate and build hardness could also be an indication of the non-homogeneity in the build microstructure which is typical of LMD-p Ti64 as discussed in section 2.6.3 and it could also be noticed during LOM and SEM analysis of the microstructures. If the hardness indent is made on a region of fine α laths or an α' region, the hardness is bound to be higher than when the indent is on a region of coarse α+β.

4.3.6 Influence of cooling rates on α-lath thickness

The influence of cooling rates on the α-lath thickness in the build of samples heat-treated for 30 minutes is shown in Figure 41 and of samples heat-treated for 75 minutes is shown in Figure 42.

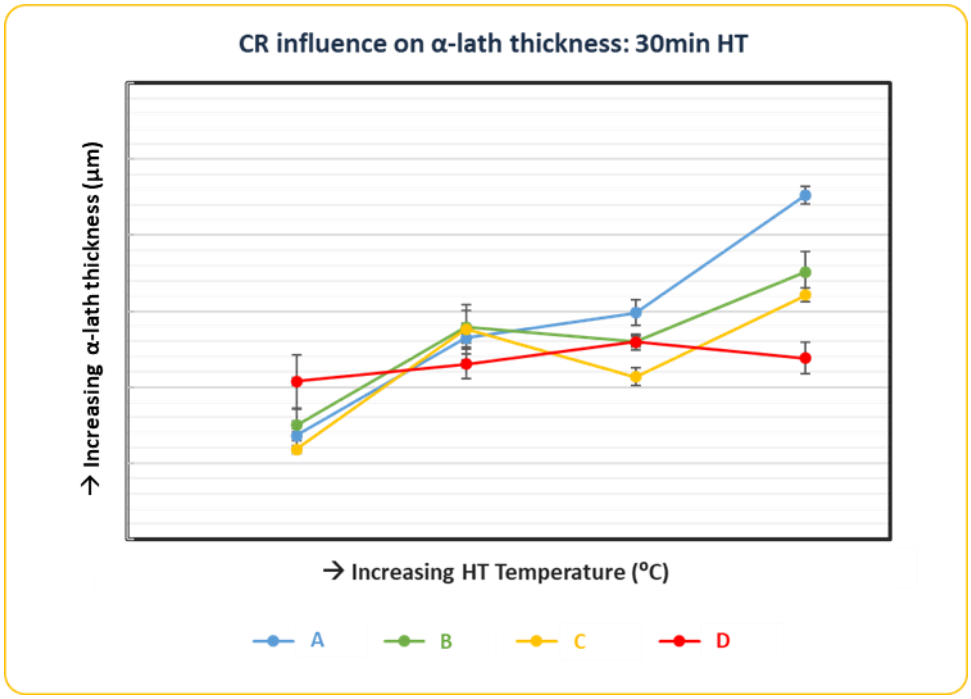


Figure 41. Influence of varying cooling rates on α-lath thickness in the build of samples heat-treated for 30 min.

It can be seen in Figure 41 that for samples heat-treated for 30 minutes, the overall influence and sensitivity of cooling rates is low for heat treatments at T1 and T2, higher for T3 and highest for T4. The lower cooling rates of A and B result in higher α-lath thickness whereas the higher cooling rate of C result in

lower α-lath thickness for all heat treatment temperatures above T2. However, the α-lath thickness for the highest cooling rate of D show a deviation from this trend. This can be attributed to the fact that controlling the cooling rate at exactly D during heat treatments proved to be tricky and the measured cooling rates were mostly higher. Further, during the heat treatment at T3 for 30 minutes, the measured cooling rate was higher than the desired C cooling rate, explaining the drop in α-lath thickness of that sample. The high sensitivity of cooling rates at high temperatures and trend of increasing α-lath thickness at lower cooling rates are in-line with the findings in literature from the work of Vrancken et al. [39].

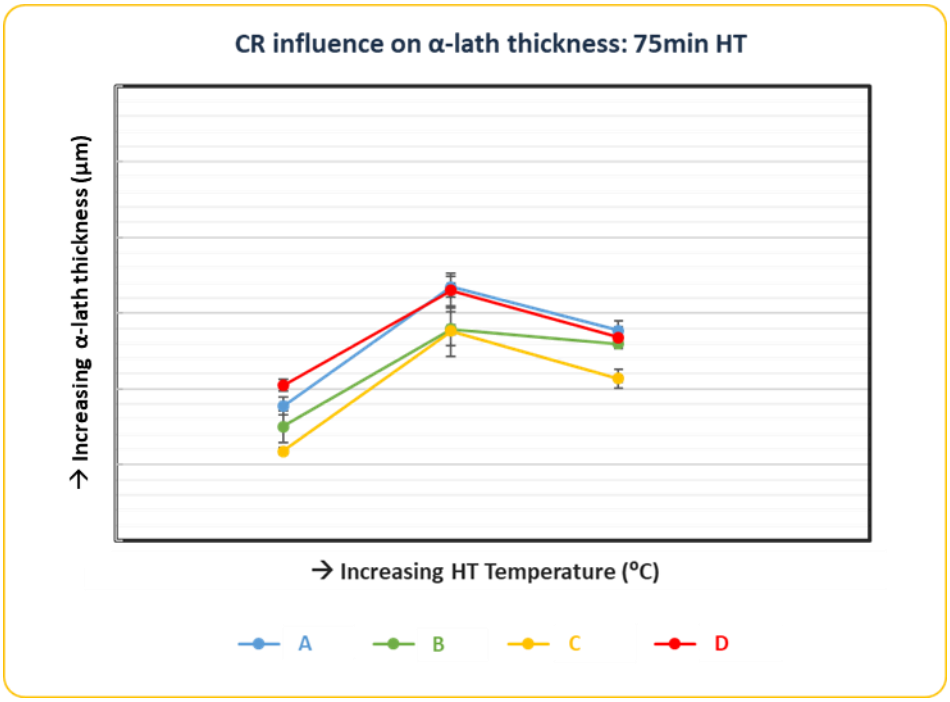


Figure 42. Influence of varying cooling rates on α-lath thickness in the build of samples heat-treated for 75 min.

In samples heat-treated for 75 minutes, results of which are shown in Figure 42, it is seen that for all heat treatment temperatures, with the exception of the D cooling rate, the α-lath thickness of the A cooled sample is the highest and C cooled sample is the lowest, similar to the trend seen in samples heat-treated for 30 minutes.

The overall findings of the influence of cooling rates on the α-lath thickness in this work, increasing α-lath thickness with a decrease in cooling rate, is similar to what was found in literature in the work of Vrancken et al. [39]. The authors discussed that this phenomenon arises from the fact that at high cooling rates, lower than that of water cooling, there exists a high undercooling which results in the nucleation of many α nuclei leading to smaller α colonies and finer α laths. At lower cooling rates, the undercooling is not as significant and the α nuclei have sufficient time to grow and coarsen.

Another key observation that can be made after studying the influence of cooling rates on the build hardness, presented in the previous section 4.3.5, and on the α-lath thickness presented here, is that at higher heat treatment temperatures, the build hardness reduces whereas the α-lath thickness increases. This correlation of reduction in build hardness with an increase in the α-lath thickness was found in

literature in the work of Azarinya et al. [19]. According to the authors, this reduction in strength with an increase in α-lath thickness is due to the weakened dislocation glide – when large α-laths precipitate along the β grain boundary and into the β grain, the dislocations can glide smoothly, reducing the strength of the material.

4.3.7 Influence of cooling rates on α and β phase fractions

The influence of cooling rates on the α and β phase fractions in the build of samples heat-treated for 30 minutes is shown in Figure 43 and of samples heat-treated for 75 minutes is shown in Figure 44.

In Figure 43, it can be seen that in samples heat-treated for 30 minutes, with the exception of the sample heat-treated at T1 and cooled at D, the cooling rate has the same influence on the α-phase fraction of samples: the lower the cooling rate, higher the α-phase fraction. The same trend can be seen in the samples heat-treated for 75 minutes as well, as shown in Figure 44.

These findings are also what was learnt during reviewing literature: with lower cooling rates, the diffusion-controlled transformation of the α-phase is preferred to the diffusion-less transformation to α'.

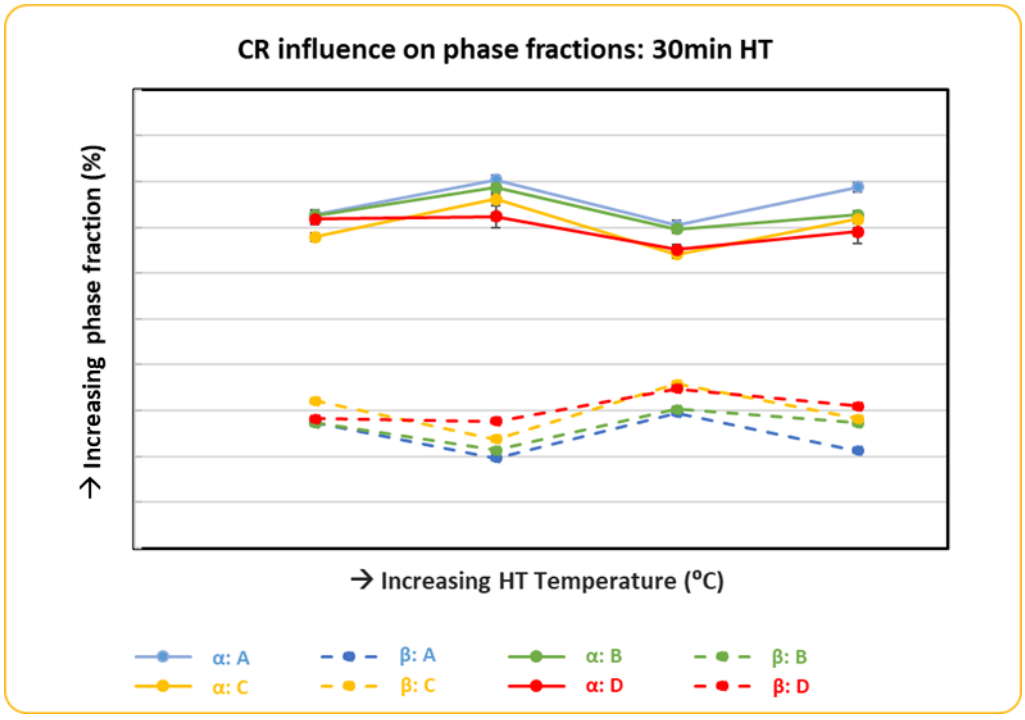


Figure 43. Influence of varying cooling rates on α and β phase fractions in the build of samples heat-treated for 30min. Solid lines indicate α-phase fraction and dashed lines indicate β-phase fraction.

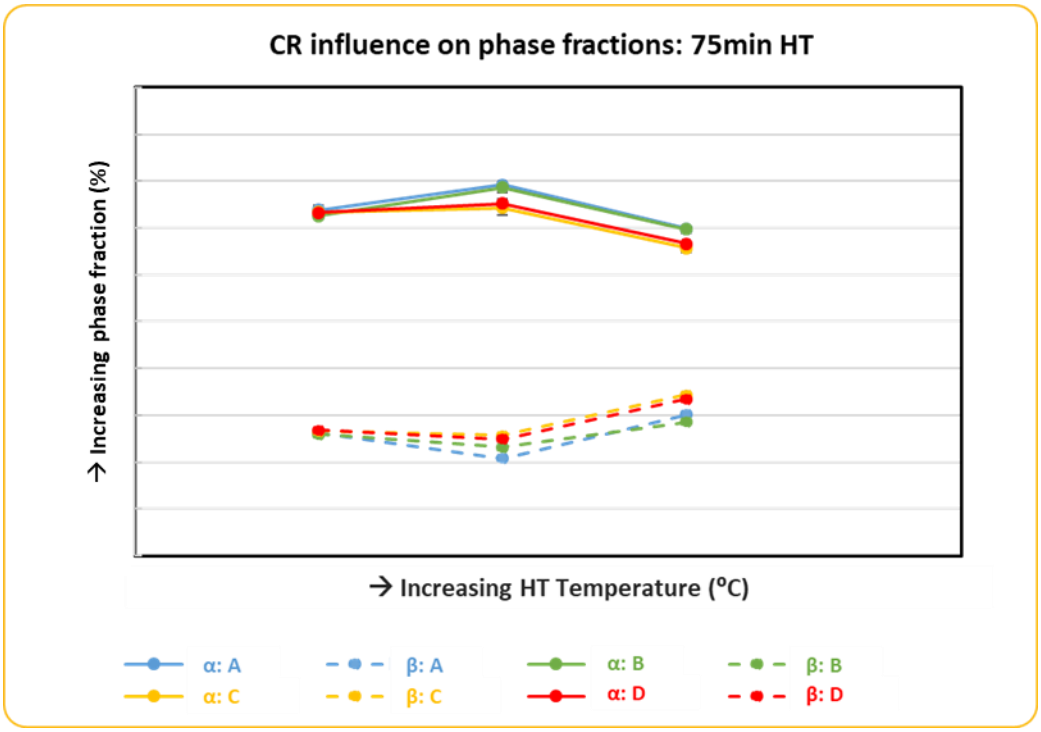


Figure 44. Influence of varying cooling rates on α and β phase fractions in the build of samples heat-treated for 75min. Solid lines indicate α-phase fraction and dashed lines indicate β-phase fraction.

It is important to note here that only the α-phase fraction was measured using MIPAR, as discussed in section 3.6.1.2, and the β-phase fraction was assumed to be remaining phase. The α' phase was not measured in this work and there exists potential for future work to be carried out with this measurement.

4.4 β-solutionized heat treatments: HT Groups 5 and 6

Results from the analysis of the as-solutionized condition and samples subjected to HT groups 5 and 6 will be presented and discussed in this section.

4.4.1 β-solutionized α-case

In samples subjected to heat treatment groups 5 and 6, pre-solutionizing followed by further heat treatments as shown in Table 5 in section 3.3.2, there was a noticeable blocky α-case penetration layer into the sample in both the build and substrate. An example of this is shown in Figure 45. The maximum thickness of this penetrated α-case layer measured in the β-solutionized sample was ~100µm. This thickness was found to increase with further local heat treatments as a function of temperature and holding time.

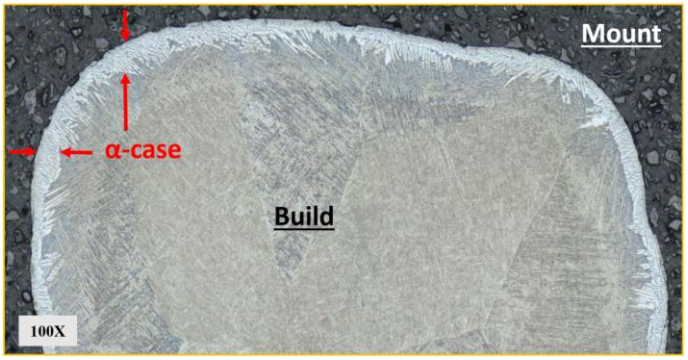


Figure 45. LOM image of the transverse profile of a β-solutionized sample showing the penetrated α-case layer into the build.

Comparing this with the samples heat-treated only locally, HT groups 1-4, the α-case layer observed was only on the surface or outside the sample as shown in Figure 21(c) in section 3.5.1. This penetration of the α-case into the sample could be attributed to the fact that the β-solutionizing was performed at a temperature above $\beta_{transus}$ for 30 minutes and then immediately quenched in water. Factors such as this high temperature making titanium extremely reactive, oxygen levels in the furnace during heat treatment, atmospheric oxygen during the transfer of the hot samples into the water container and the oxygen in the water until the sample cools down to below the 600°C reactive temperature limit; all play in important role in causing such a penetration of the brittle α-case into the samples.

It is therefore important to understand how deep the penetration of this undesired brittle α-case into the sample is, so as to know how much of the sample's surface needs to be machined off before being put into service. To that extent, an α-case penetration study was carried out and the results of which are shown in Figure 46. Hardness measurements were made in the transverse direction of the samples at close intervals starting from the top of the build moving towards the middle until the build's overall average hardness was reached.

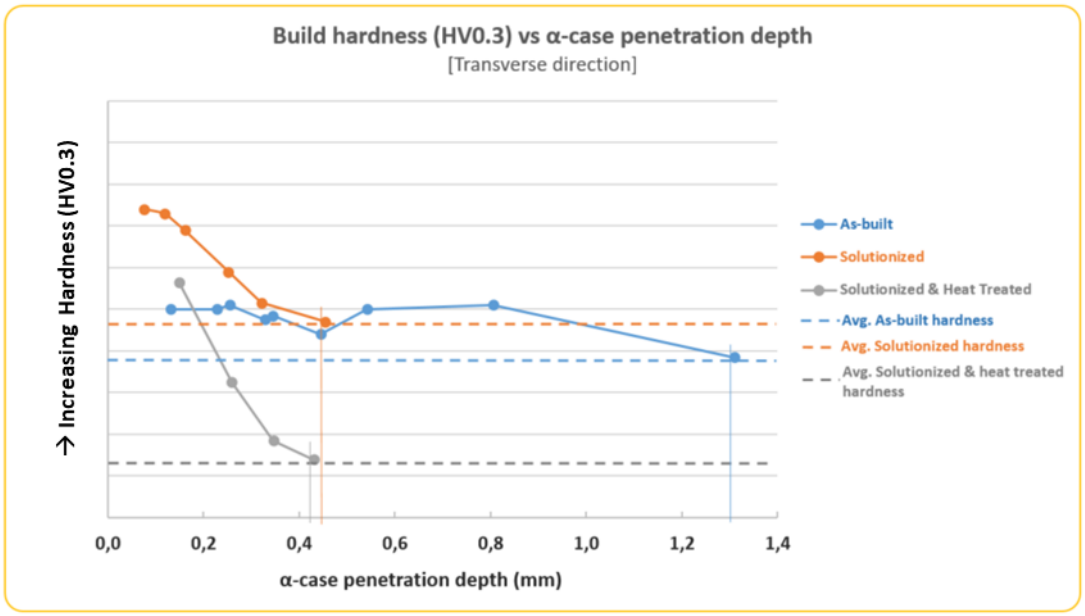


Figure 46. α-case penetration study showing the hardness measurements at different depths. Vertical lines are guidelines for the exact penetrated depth of α-case.

It can be seen in Figure 46 that in the as-built condition, the hardness variation from the surface towards the middle is not as high compared to the solutionized sample or a solutionized and heat-treated sample. This is because during the LMD-p process, the build chamber is filled with a protective inert gas to shield the build from any possible oxidation. Further, due to the non-homogeneity in the build microstructure in the as-built sample as discussed in section 4.2.3, the hardness measurements are highly dependent on the exact location of the indent and whether it is on a α' region or an α+β region, with the former giving a higher hardness than the latter. Hence, in case of the as-built sample, both factors, the comparatively lower hardness difference between the surface and middle, and the non-homogeneity of microstructure, should be taken into account for a more accurate study of the α-case penetration. In the solutionized sample, the hardness difference between the surface and middle of the build is higher due to the lack of any protection from oxidation during global heat treatment. In the solutionized and heat-treated sample, the hardness difference between the surface and the middle of the build is significantly more due to the additional oxidation the sample was subjected to during further local heat treatment.

4.4.2 β-solutionized β grain size

The β grain size of sample subjected to β-solutionizing was measured to be 484±43 μm. This is almost twice the grain size of the as-built sample, and more than the grain sizes measured in all heat-treated samples shown in section 4.3.3.

This is a clear indication of the grain growth at temperature above $\beta_{transus}$ discussed in section 2.7.1, where the columnar prior β grains present in the as-built state experience a growth in grain size after being heat-treated at above the β_{tranus} temperature.

4.4.3 β-solutionized microstructure

The microstructure of the β-solutionized sample is shown in Figure 47. In the stitched image of the whole mounted sample's longitudinal profile shown in Figure 47(a), the build and substrate regions cannot be differentiated, as was possible in all samples subjected to HT groups 1 to 4. The columnar β grains seen in the as-built condition have now taken a more semi-equiaxed morphology with measured grain growth from 229±89 μm to 484±43 μm. This phenomenon was reviewed in section 2.7.1, where the columnar prior β grains in the as-built state transform to a semi-equiaxed morphology by undergoing a shearing mechanism and losing their columnar morphology followed by a growth in grain size.

As shown in Figure 47(b), there were a lot of fine or acicular α' regions present in the overall build area. This is because of the water quenching the samples were subjected to which induces extremely high cooling rates, favouring the β to α' transformation.

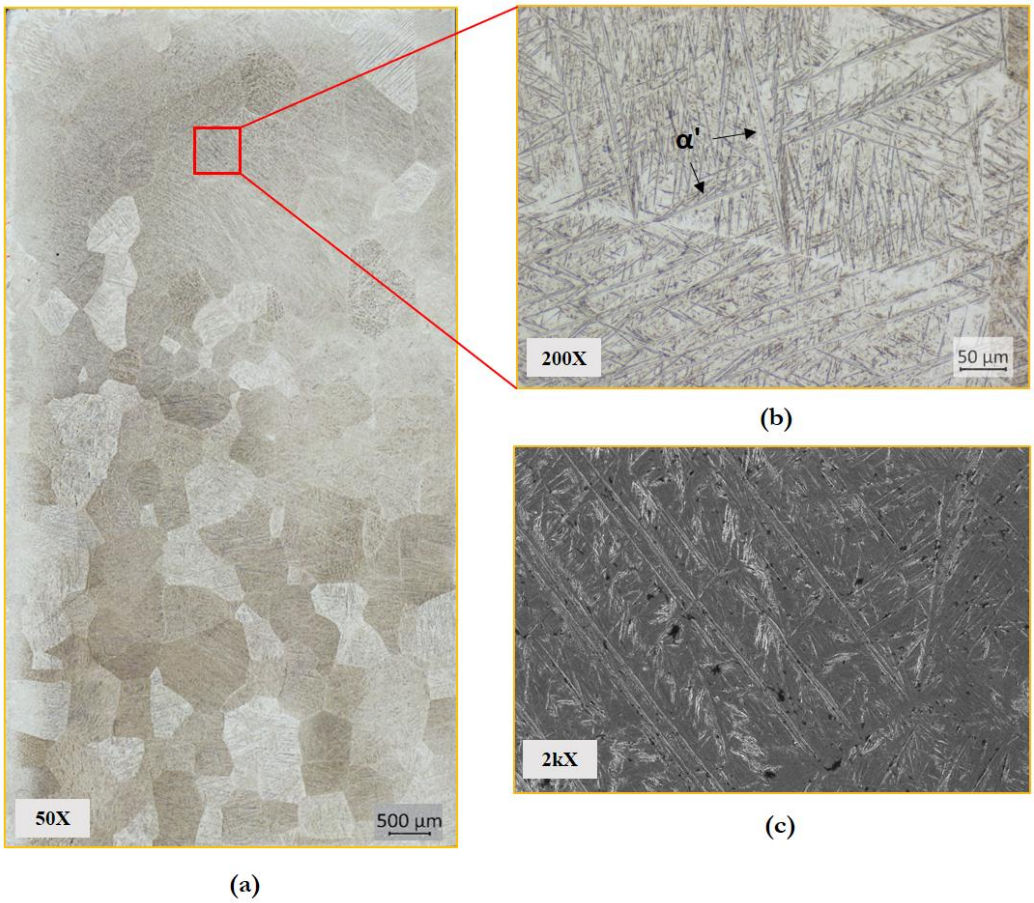


Figure 47. Microstructure of β-solutionized sample in the longitudinal profile: (a) LOM stitched image of build and substrate, (b) LOM image of build and (c) SEM image of build. Red box is indicative of region only, enlarged image is not to its scale.

4.4.4 Influence of cooling rate on β-solutionized β grain size

Figure 48 shows the effect of a low cooling rate of A and a high (air-cooled) cooling rate on the β grain size of β-solutionized samples heat-treated at T2 and T4 for 30 minutes compared with samples heat-treated with the same parameters but without the pre-solutionizing treatment. It can be seen that the pre-solutionizing does cause an overall increase in grain size compared to the as-built grain size. In the β-solutionized samples, heat treatments at both T2 and T4 result in bigger β grains when cooled at a high cooling rate than when cooled slowly. This increase in β grain size found with an increase in cooling rate after heat treatments of pre-solutionized samples needs further study for a more detailed understanding of the phenomenon.

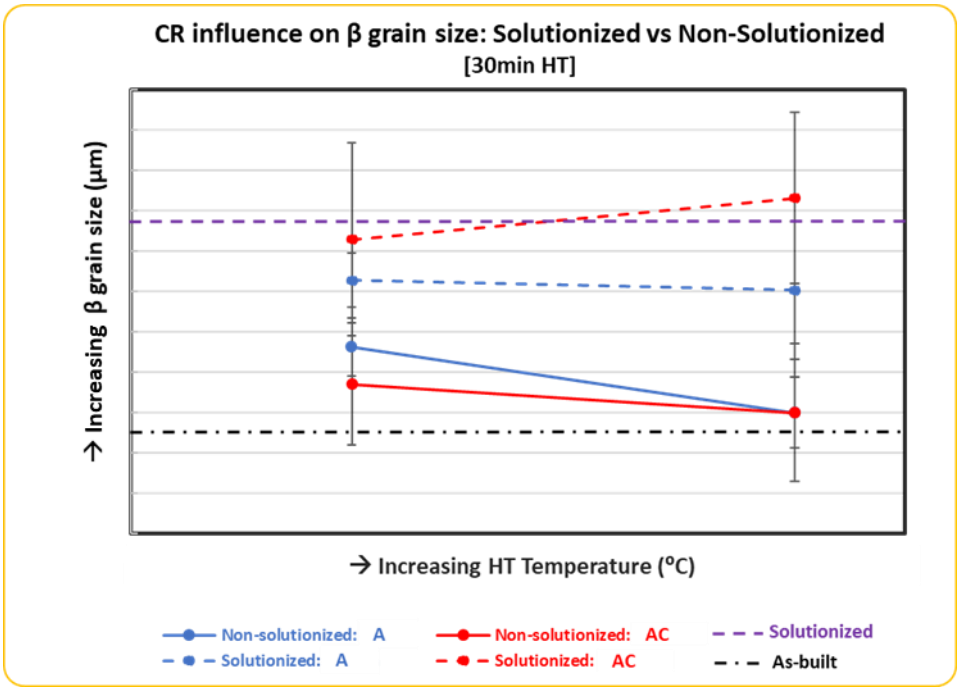


Figure 48. Influence of varying cooling rates on β grain size in the build of samples β-solutionized and heat-treated at T2 and T4 for 30 min (dashed lines) compared with those without prior β-solutionizing (solid lines). Purple dashed line indicates the solutionized β grain size. Black dotted line indicates the as-built β grain size.

4.4.5 Influence of cooling rate on β-solutionized microstructure

LOM images of the microstructure of a β-solutionized sample heat-treated at T4 for 30 minutes and air-cooled is shown in Figure 49 and of another sample subjected to the same heat treatment but cooled at a low cooling rate of A is shown in Figure 50.

In the air-cooled sample, there are regions of α' seen along with regions of fine α+β in different non-homogeneous mixtures of Widmanstätten and basketweave morphologies in the overall build microstructure shown in Figure 49(a). Zooming in on an area in the middle of the build, regions of continuous α-phase on prior β grain boundary, also called α-grain boundary (α_{GB}) [11], as shown in Figure 49(b), were also observed.

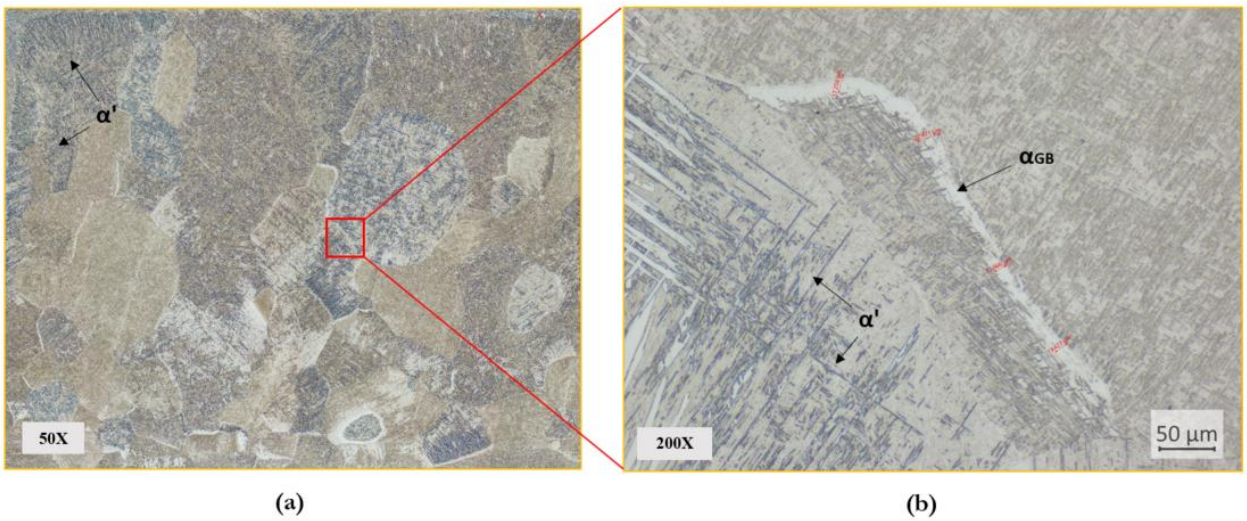


Figure 49. LOM images of β-solutionized sample heat-treated at T4 for 30 min and air-cooled, showing (a) stitched image of the entire build and (b) a zoomed-in region in the build. Red box is indicative of region only, enlarged image is not to its scale.

In the sample slow cooled from the same heat treatment temperature at T4 for 30 minutes, the microstructure of the whole build and that of an enlarged region in the build is shown in Figure 50(a) and (b) respectively. In the overall build microstructure, there was no α' seen and only a non-homogeneous structure with different morphologies Widmanstätten and basketweave of α+β was observed. There were also regions of equiaxed α+β, as shown in Figure 50(b) along with some coarse α-laths and some almost globular α phases. This is a clear indication of the complete decomposition of α' to α+β upon heating followed by nucleation and growth controlled phase transformations favoured by the slow cooling.

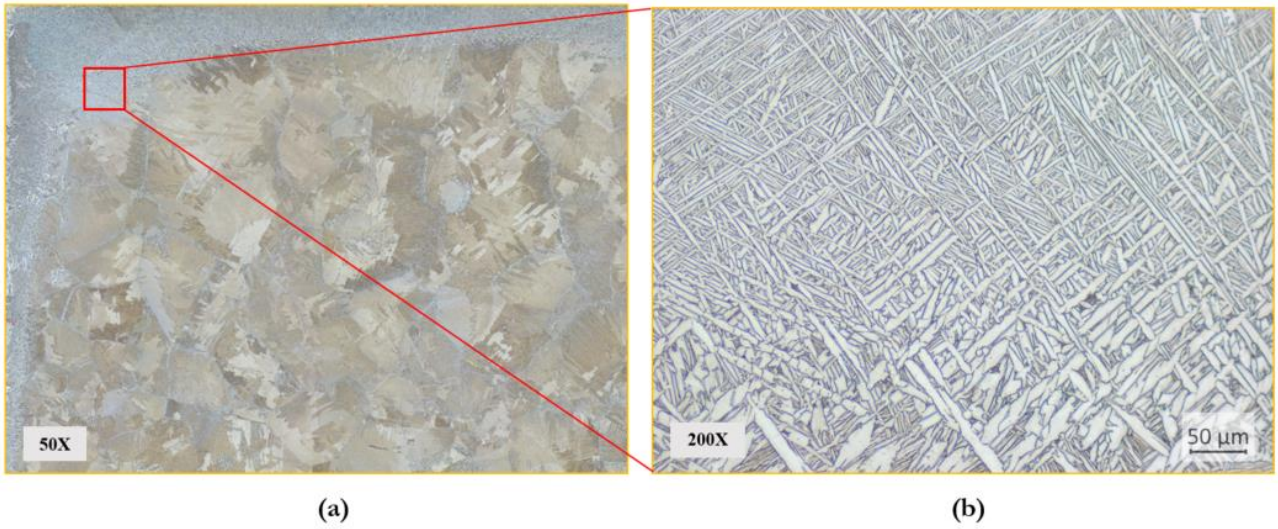


Figure 50. LOM images of β-solutionized sample heat-treated at T4 for 30 min and cooled at A, showing (a) stitched image of the entire build and (b) a zoomed-in region in the build. Red box is indicative of region only, enlarged image is not to its scale.

LOM images of the microstructure of a β-solutionized sample and heat-treated at a temperature T2, which is lower than T4, for 30 minutes and air-cooled is shown in Figure 51 (a) and (b), and of another sample subjected to the same heat treatment but cooled at a low cooling rate of A is shown in Figure 52 (a) and (b).

It can be seen from Figure 50(b) and Figure 51(b) that the microstructure of the two samples look similar with no α' regions, indicating a complete decomposition of the α' present in the as-solutionized state. Further, there is very little change in the resulting α-lath thickness in the same two images, with the slow cooled sample having more regions of slightly coarser α-laths. As was the case with the microstructure analysis of samples heat-treated in HT groups 1-4, discussed in section 4.3.4, in order to understand the influence of cooling rates on the build microstructure fully, further image processing by means of MIPAR is necessary.

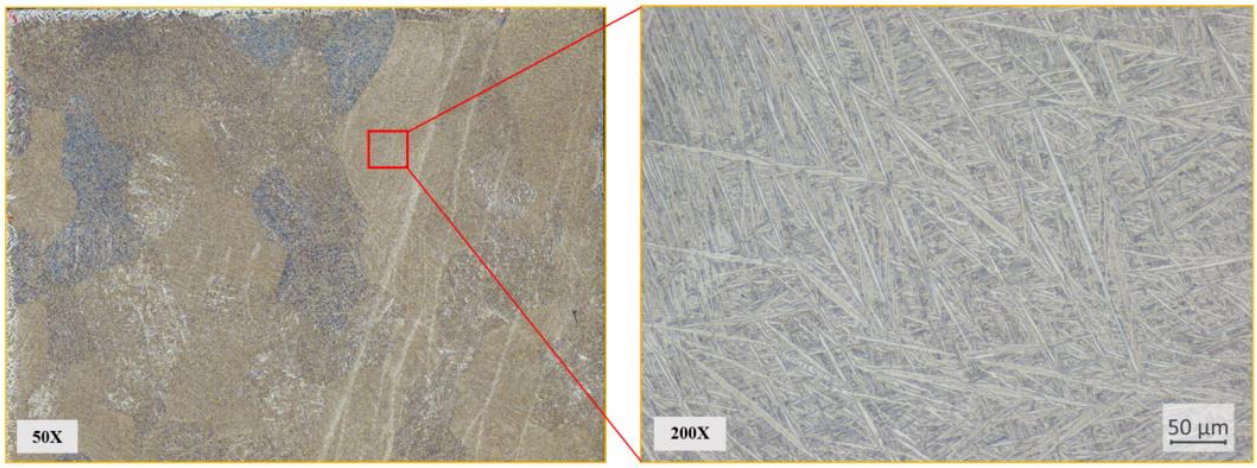


Figure 51. LOM images of β-solutionized sample heat-treated at T2 for 30 min and air-cooled, showing (a) stitched image of the entire build and (b) a zoomed-in region in the build. Red box is indicative of region only, enlarged image is not to its scale.

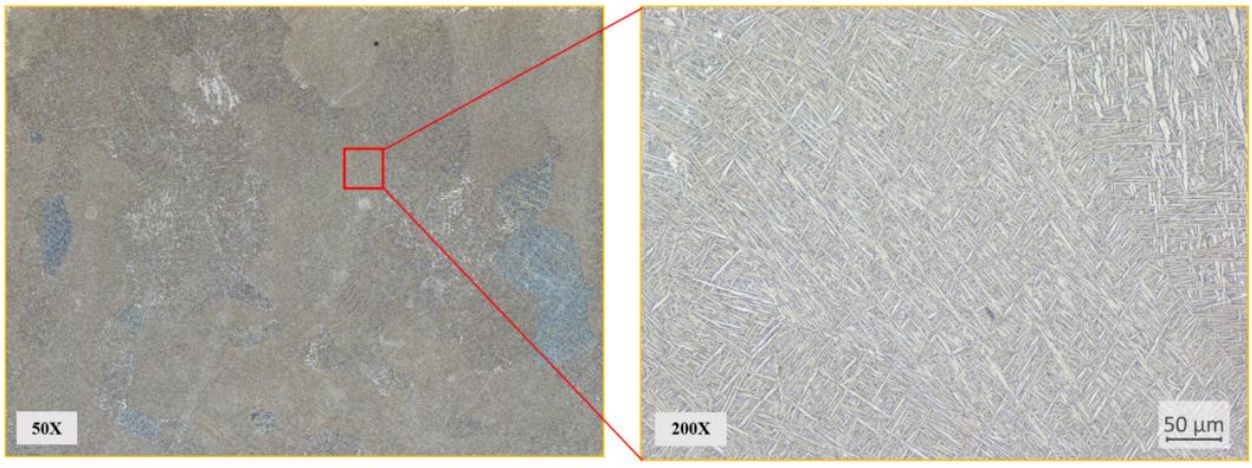


Figure 52. LOM images of β-solutionized sample heat-treated at T2 for 30 min and cooled at A, showing (a) stitched image of the entire build and (b) a zoomed-in region in the build. Red box is indicative of region only, enlarged image is not to its scale.

In the β-solutionized samples heat-treated at T4 and air-cooled, the resulting α' can be traced back to its transformation from the amount of transformed β-phase formed upon holding at this temperature for 30 minutes and is not the pre-existing α' found in the as-solutionized state. This is because of two factors. Firstly, the measured cooling rate for this air-cooled sample was extremely high and the highest measured cooling rate among all of the experiments conducted, which was high enough for α' formation during cooling. Since the samples used for these β-solutionizing heat treatments were from the smaller set, the measured cooling rates during air-cooling these samples were generally much higher compared to the ones measured for the big samples. Second, since it is seen that the pre-existing α' undergoes complete decomposition even at a lower heat treatment temperature of T2, there ought to be complete α' decomposition at the higher temperature T4, further indicating that the α' found is the amount transformed upon cooling from T4 rather than what was left over from incomplete decomposition of the pre-existing α'. Further, as seen in the JMatPro plots of Ms and Mf temperatures for heat treatments at T2 and T4 attached in Appendix B, it can be seen that for β grain size of 500µm, which is the closest to the

measured grain size of 484±43 μm in the β-solutionized sample, the M_s in the case of T4 heat treatment is much higher, 686°C compared to 66°C in the case of T2 heat treatment. This means that the onset of α' in the T4 heat-treated sample happens much earlier during cooling than in the sample heat-treated at T2, which was observed in this work.

Another inference that can be drawn from the microstructural analysis of samples heat-treated after β-solutionizing is that the influence of cooling rates is much more significant when the heat treatment temperature is higher and closer to $\beta_{transus}$ than when it is lower and far below it, similar to the findings of the work done by Vrancken et al. [39].

4.4.6 Influence of cooling rate on β-solutionized build hardness

Figure 53 shows the effect of a high and low cooling rate on the build hardness of samples heat-treated at T2 and T4 for 30 minutes with a pre-solutionizing treatment compared to samples without the pre-solutionizing treatment. In the pre-solutionized samples, both heat treatments result in hardness values below the as-built condition, with the slow cooling rate giving higher hardness than the air-cooled sample after both heat treatments.

This phenomenon of a decrease in hardness in the case of slow cooling compared with faster cooling during heat treatments of β-solutionized samples in the temperature range of T2 and T4 was reported by Vilaro et al. [32] as well. The authors concluded this to be resulting from the increase in the α-lath thickness which is typically seen in slow cooling rates during heat treatments, as reviewed in section 2.7.2. According to them, the high hardness in the samples cooled rapidly was due to the formation of the soft orthorhombic α" phase which gives a more softening effect than a hardening effect. Their heat treatments, however, were carried out after a pre-solutionizing treatment similar to this work, followed by heat treatments at T2 and T4 and cooled by furnace cooling and air cooling, similar to the cooling rates of this work, but for a holding time of two hours instead of the 30 minutes in this work. This time factor needs to be taken into account while making this comparison with their work and moreover, they do not discuss how they identified or differentiated between the α' and α" phases. This observation hence needs further study to understand the phenomenon in detail.

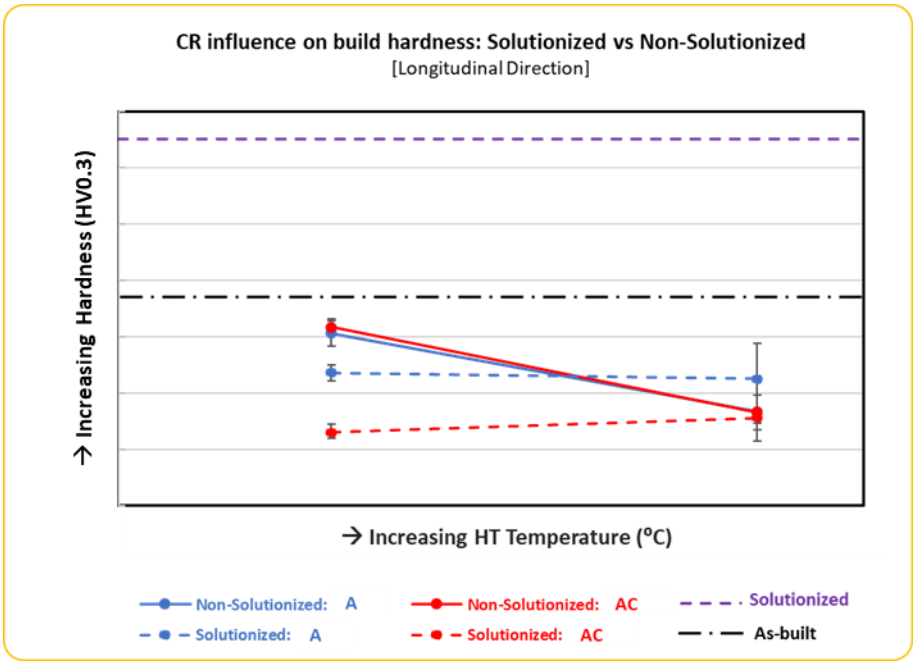


Figure 53. Influence of varying cooling rates on build hardness of samples β-solutionized and heat-treated at T2 and T4 for 30 min (dashed lines) compared with those without prior β-solutionizing (solid lines). Purple dashed line indicates the average build hardness of solutionized sample. Black dotted line indicates average build hardness of as-built sample.

4.4.7 Influence of cooling rate on β-solutionized α-lath thickness

Figure 54 shows the influence of fast and slow cooling on the resulting α-lath thickness in the build of samples heat-treated at T2 and T4 for 30 minutes with pre-solutionizing treatment compared to samples without pre-solutionizing treatment. In the solutionized and heat-treated samples, the low cooling rate of A gives larger α-lath thickness compared to the air-cooled cooling rate, at both heat treatment temperatures. The same trend is seen for the samples heat-treated with the same parameters without the pre-solutionizing as well.

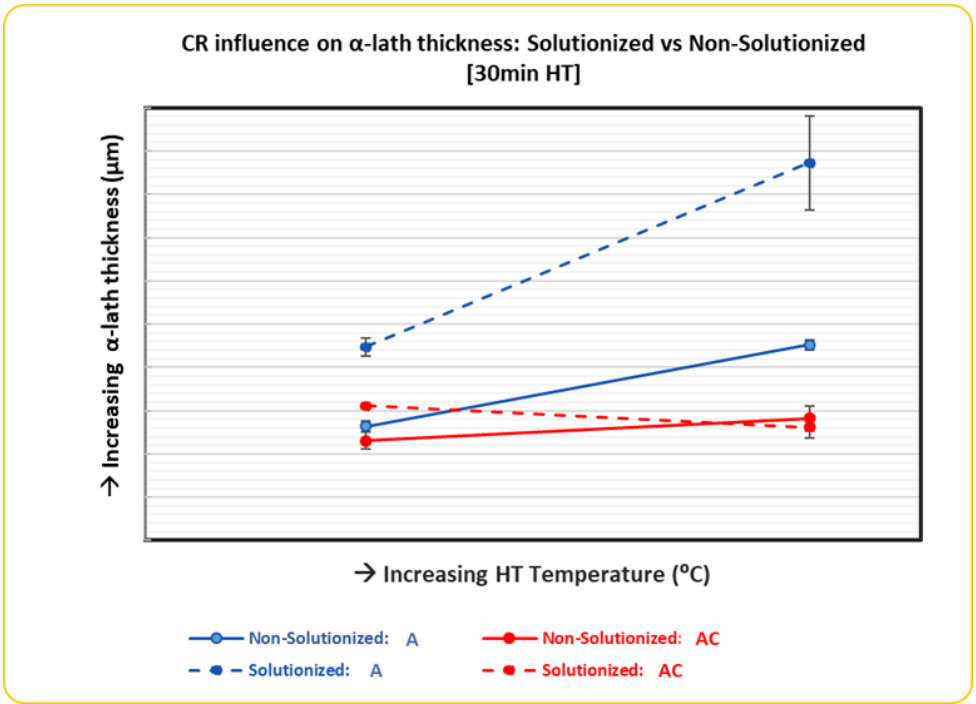


Figure 54. Influence of varying cooling rates on α-lath thickness of samples β-solutionized and heat-treated at T2 and T4 for 30 min (dashed lines) compared with those without prior β-solutionizing (solid lines).

These findings and the overall influence of the cooling rate on α-lath thickness in pre-solutionized samples are the same as what was found in the case of all heat treatments in HT groups 1-4 as well, which were not pre-solutionized, as discussed in section 4.3.6, where an increase in the cooling rate resulted in a decrease in the α-lath thickness.

4.4.8 Influence of CR on β-solutionized α phase fraction

Figure 55 shows the influence of fast and slow cooling on the resulting α-phase fraction in the build of samples heat-treated at T2 and T4 for 30 minutes with pre-solutionizing treatment compared to samples without. For heat treatment at T2, the α-phase fraction of the sample pre-solutionized was found to be lower than that of the non-solutionized sample for both cooling rates. After heat treatment at T4 however, the α-phase fraction of the solutionized sample was found to be higher for both cooling rates. In both cases however, pre-solutionized and non-solutionized, the effect the two cooling rates had is the same: the low cooling rate gave higher α-phase fraction whereas the high cooling rate gave lesser α-phase fraction.

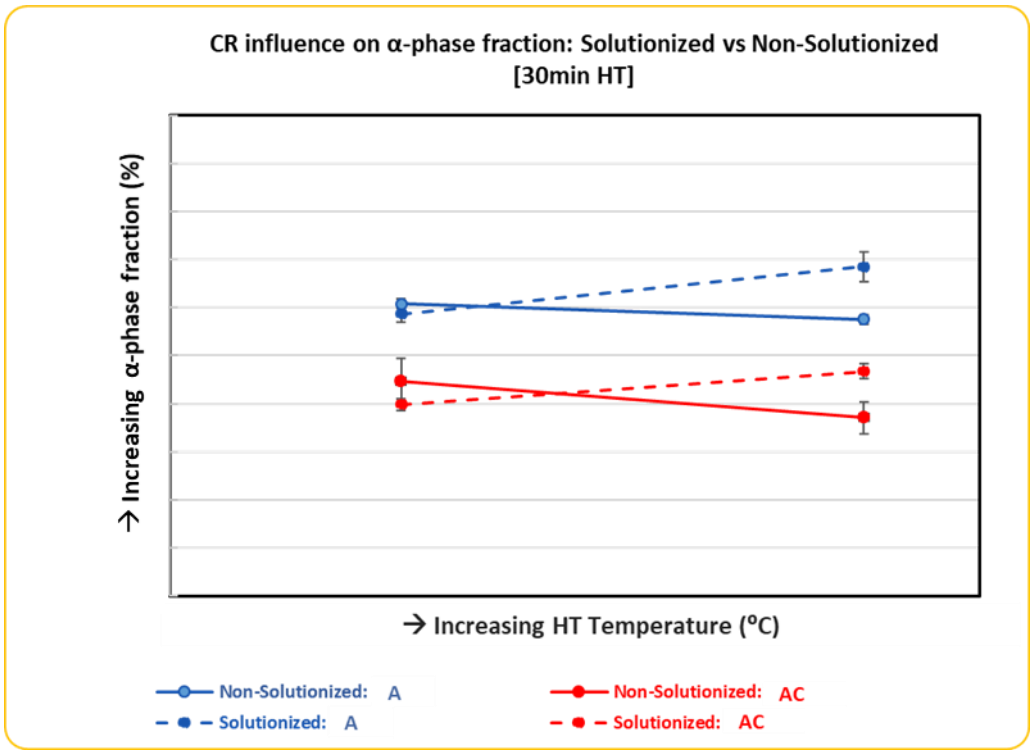


Figure 55. Influence of varying cooling rates on α-phase fraction of samples β-solutionized and heat-treated at T2 and T4 for 30 min (dashed lines) compared with those without prior β-solutionizing (solid lines).

These findings on the influence of cooling rates on the on the α-phase fraction in pre-solutionized samples are the same as what was found in the case of all heat treatments in HT groups 1-4 as well, as discussed in section 4.3.7, that with lower cooling rates, the diffusion-controlled transformation of the α-phase is preferred to the diffusion-less transformation to α'.

4.5 Simulations vs Experimental results

In order to make a comparison between the simulation results of the α-phase fraction predicted by JMatPro and ThermoCalc with that observed in experimental results, Figure 56 is shown with the black dotted boxed area being the region of heat treatment temperatures and cooling rates that were in common between the two. This basically means that the region of interest in the simulation results that can be compared with experimental observations is limited to heat treatment temperatures of T1 to T4 and cooling rates of D to A.

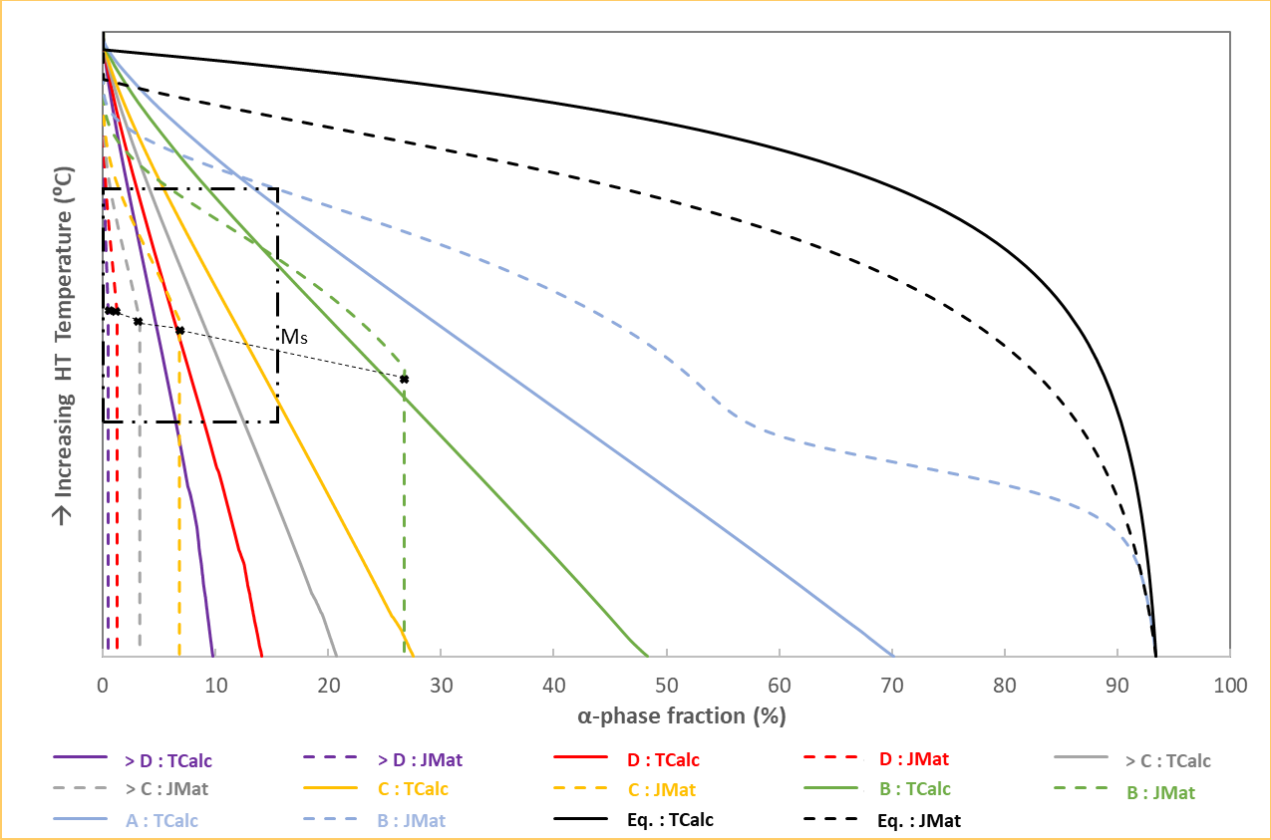


Figure 56. Comparison plot for JMatPro and ThermoCalc simulation results showing the influence of cooling rates on α-phase fraction during cooling with the black dotted box marking the region which is experimentally relevant and comparable.

For the purposes of a better visualization of the comparison in a common format, 2D surface plots or heat maps of the α-phase fraction results of both the simulations and experiments are shown in Figure 57, where the top two plots are of the simulation results and the bottom two are of the experimental results.

It can be seen that the overall trend in terms of an increase in the α-phase fraction at lower cooling rates predicted by the two simulation tools is the same as what was observed in experimental results, more specifically for heat treatments between the temperature range T1 and close to T3. Another accurate prediction trend observed in the simulation trends is the reduction in the α-phase fraction with an increase in heat treatment temperatures and cooling rates.

When it comes to why there still exists gaps between the simulation tool predictions and experimental observations in terms of the exact values of α-phase fractions, the following could be possible factors worth understanding:

- Both simulation tools base all their predictions with the assumption that the material data input is in a conventionally processed condition and do not yet have a feature to either input the additively manufactured state as the starting point. The differences in both microstructural and mechanical properties that differ between the conventionally processed route and AM has been reviewed in section 2.6. For example, JMatPro does not take into account the pre-existing α' in the as-built condition at the start of its simulations and instead assumes an equiaxed state with only α+β phases which is commonly found in CM Ti64.
- Another important factor that simulation tools are not yet designed to consider during their simulations is the thermally induced stresses that heat treatments are bound to induce and the influence these stresses have in causing some preferential phase transformations or recrystallization of phases. For example, as discussed in section 4.4.3, in the β-solutionized experimental sample, the columnar β grains were observed to be converted to more globular or semi-equiaxed grains by a thermally induced shearing mechanism which then has an influence on the resulting α-phase fraction.
- Both simulation tools use thermodynamic models like the JMAK model for the prediction of phases. Although this has been shown to be an effective way of predicting phase fractions, the calculated results will always be data which has been extrapolated in accordance with a set of previously known or observed information updated in their respective databases. In case of data resulting from a more interpolation approach where the exact start, intermediate and end conditions are known, the predictions can be more accurate and be relied upon.
- This extrapolated data could potentially be much less accurate when it comes to predicting phase formation upon cooling from a certain heat treatment temperature since there existed a lack of sufficient literature and research on understanding the exact influence of cooling rates during heat treatment of additively manufactured Ti64. Moreover, for instance, the discrepancy found in literature on the exact critical cooling rate for M_S is another sign that this important parameter in the heat treatment of Ti64 needs more attention in future research.
- Experimental results of the α-phase fraction were calculated by the means of processing of microstructural SEM images in MIPAR. This might not be the most accurate measurement method since a lot of the image processing quality depends on how well the samples' microstructural features are revealed depending on the etching technique and quality. Moreover, it is not easy to differentiate between the α-phase and α' phase in SEM images and there is a possibility that even the α' phase is being considered as α-phase in the final MIPAR calculations.

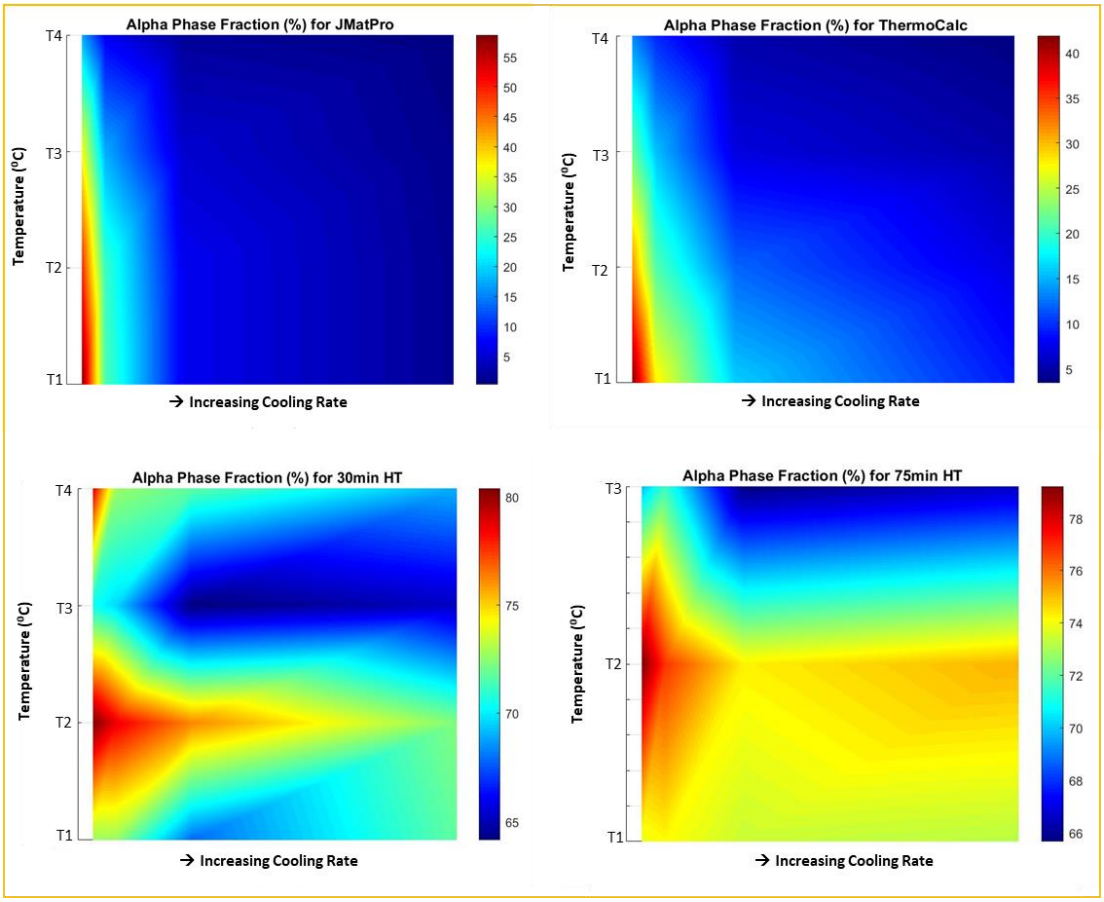


Figure 57. 2D surface plots for simulation results (top two) and experimental results (bottom two) showing the influence of cooling rates on α-phase fraction during cooling at different rates.

It is important to know the underlying theory behind the prediction of data by simulation tools and to compare these predictions with actual experimental observations so that their capabilities and shortcomings can be fully understood. This is a holistic approach to realizing the full potential of simulation tools for the effective understanding of microstructural changes influenced by varying the cooling rates during heat treatment, which was one of the aims this thesis work intended on achieving.

5 CONCLUSIONS

- Simulation tools predict the trend of increasing α-phase fraction with a reducing cooling rate similar to experimental observations. There exist gaps in the exact values of the α-phase fraction between the simulation and experimental results, with the experimental results showing much higher values.
- Low cooling rates reduce the Ms temperature thereby delaying the onset of α' upon cooling, consequently reducing the chances of α' formation, whereas high cooling rates increase the Ms temperature causing an earlier onset of α', thereby increasing the chances of α' formation.
- Cooling rates during heat treatments have minimal or no influence on the β grain size and α case thickness. Heat treatment temperature and time have a more significant influence on both.
- Cooling rates have less influence on the build hardness of heat-treated samples owing to the overall non-homogeneity of the microstructure.
- Cooling rates have an influence on the overall microstructure and its key features such as α-lath thickness, α and β phase fractions, as follows:
    - High cooling rates result in small α-lath thickness; lower the cooling rate, higher the α-lath thickness
    - High cooling rates result in low α-phase fraction; low cooling rates give higher α-phase fraction
- This overall influence of cooling rates is more significant at higher heat treatment temperatures close to βtransus or above, than at temperatures far below βtransus.
- Cooling rates have the same influence on the α-lath thickness, α and β phase fractions in samples heat-treated after a β-solutionizing heat treatment.

6 FUTURE WORK

- A system to ensure more accurate control of heat treatment cooling rates of D or higher can result in a more effective understanding of high cooling rates on microstructural changes in Ti64.

- For a more complete overview of the exact microstructural evolution of LMD-p Ti64 throughout the heat treatment process, it is important to consider the influence of the heat treatment temperature and holding time as well. Hence, a model combining the influence of those parameters and the results of this thesis work could prove to be more effective tool for designing a thorough heat treatment.

- There is room for improvement in the measurement techniques of experimental results from the microstructural images using MIPAR. By feeding MIPAR with lots of LOM images of the build highlighting the α' regions, its 'deep learning' tool can be 'taught' to better detect the α' phase which can then be compared to and adjusted with the α phase fraction measurements. This could also be done for more efficient measurements of β grain sizes.

7 REFERENCES

[1] Singamneni, S., Yifan, L.V., Hewitt, A., Chalk, R., Thomas, W., Jordison, D. (2019) Additive Manufacturing for the Aircraft Industry: A Review. *J Aeronaut Aerospace Eng 8*, 214. https://doi.org/10.35248/2168-9792.19.8.215

[2] Liu, R., Wang, Z., Sparks, T., Liou, F., Newkirk, J. (2017). Aerospace applications of laser additive manufacturing. Woodhead Publishing, 351-37. http://dx.doi.org/10.1016/B978-0-08-100433-3.00013-0

[3] Najmon, J. C., Raeisi, S., Tovar, A. (2019). Review of additive manufacturing technologies and applications in the aerospace industry. Elsevier. 7-31. https://doi.org/10.1016/B978-0-12-814062-8.00002-9

[4] Website (industrytoday.com). (April 28, 2021). Global 3D printing products and services market size from 2020 to 2026 (in billion U.S. dollars) [Graph]. In Statista. Retrieved July 01, 2021, from https://www.statista.com/statistics/315386/global-market-for-3d-printers/

[5] Aainsqatsi, K. (2008) Turbofan operation. Wikimedia Commons. CC BY 2.5. Available online: https://commons.wikimedia.org/wiki/File:Turbofan_operation.svg

[6] Shaw, R. J., (2021). Engines. NASA. Available online: https://www.grc.nasa.gov/www/k-12/UEET/StudentSite/engines.html

[7] Han, P. (2017). Additive Design and Manufacturing of Jet Engine Parts. Engineering, 1(5), 648-652. https://doi.org/10.1016/J.ENG.2017.05.017.

[8] National Research Council (US) Committee on Air Quality in Passenger Cabins of Commercial Aircraft. The Airliner Cabin Environment and the Health of Passengers and Crew. Washington (DC): National Academies Press (US); 2002. 2, Environmental Control. Available from: https://www.ncbi.nlm.nih.gov/books/NBK207472/

[9] Mouritz, A. P. (2012). *Introduction to aerospace materials*. Woodhead Publishing.

[10] Cervenka, M. (2000). The Rolls-Royce Trent Engine [PowerPoint slides], Rolls-Royce. Available online: https://slidetodoc.com/the-rollsroyce-trent-engine-michael-cervenka-technical-assistant/

[11] Lutjering, J., Williams, J. C. (2007) *Titanium* (2nd ed.). Springer.

[12] Boyer, R. R. (1996). An overview on the use of titanium in the aerospace industry. Materials Science and Engineering, Boeing Commercial Airplane Group Seattle, 103-114.

[13] Banerjee, S. and Mukhopadhyay P. (2010) *Phase transformations: examples from titanium and zirconium alloys*. Elsevier.

[14] Totten, G. E. (2016). *Heat Treating of Nonferrous Alloys*. ASM International. https://doi.org/10.31399/asm.hb.v04e.9781627081696

[15] Zhong, C., et al. (2020). Laser Metal Deposition of Ti6Al4V—A Brief Review. Applied Sciences 10(3), 764. https://doi.org/10.3390/app10030764

[16] Wells, M. G. H., Roopchaud B., Montgomery J. S., Gooch W. S. (1998) Non-Aerospace Applications of Titanium, TMS, 289.

[17] Herzog, D., Seyda, V., Wycisk, E., Emmelmann, C. (2016). Additive manufacturing of metals. Acta Materialia, 371-392.

[18] Bourell, D.L., Leu M.C., Rosen D.W. (1994) Roadmap for Additive Manufacturing, University of Texas.

[19] Azarniya, A., et al., (2019). Additive manufacturing of Ti-6Al-4V parts through laser metal deposition (LMD): Process, microstructure, and mechanical properties. Journal of Alloys and Compounds 804, 163-191. https://doi.org/10.1016/j.jallcom.2019.04.255

[20] Liu, Z., He, B., Lyu, T. et al. (2021). A Review on Additive Manufacturing of Titanium Alloys for Aerospace Applications: Directed Energy Deposition and Beyond Ti-6Al-4V. JOM 73, 1804–1818. https://doi.org/10.1007/s11837-021-04670-6

[21] Thaheri, H., et al, (2017). Powder-based additive manufacturing – a review of types of defects, generation mechanisms, detection, property evaluation and metrology. IJASMM 1(2). https://doi.org/10.1504/IJASMM.2017.088204

[22] Barua, S., Liou, F., Newkirk, J. and Sparks, T. (2014). Vision-based defect detection in laser metal deposition process. Rapid Prototyping Journal, V20 No. 1, 77-85. https://doi.org/10.1108/RPJ-04-2012-0036

[23] Ahmed, T., Rack, H. J. (1998). Phase transformations during cooling in α+β titanium alloys. Materials Science and Engineering A243, 206-211.

[24] Lu, S.L., et al. (2016). Massive transformation in Ti–6Al–4V additively manufactured by selective electron beam melting, Acta Materialia 104, 303-311. https://doi.org/10.1016/j.actamat.2015.11.011

[25] Wang T., et al. (2015) Grain morphology evolution behavior of titanium alloy components during laser melting deposition additive manufacturing. Journal of Alloys and Compounds 632, 505-513. http://dx.doi.org/10.1016/j.jallcom.2015.01.256

[26] Liu, S., Shin, Y. C. (2019). Additive manufacturing of Ti6Al4V alloy: A review. Materials & Design 164. https://doi.org/10.1016/j.matdes.2018.107552

[27] Neikter, M., et al. (2017). Microstructure characterisation of Ti-6Al-4V from different additive manufacturing processes. IOP Conference Series: Materials Science and Engineering 258.

[28] Neikter, M. (2017). Microstructure and Texture of Additive Manufactured Ti-6Al-4V (Licentiate dissertation, Luleå University of Technology).

[29] Lutjering, G. (1998). Influence of processing on microstructure and mechanical properties of (α+β) titanium alloys. Technical University Hamburg.

[30] Yao, J., et al. (2016). Influence of heat-treatment on the dynamic behavior of 3D laser-deposited Ti–6Al–4V alloy. Materials Science and Engineering: A 677, 153-162. http://dx.doi.org/10.1016/j.msea.2016.09.036

[31] Bermingham, M.J., et al. (2018). Optimising the mechanical properties of Ti-6Al-4V components produced by wire + arc additive manufacturing with post-process heat treatments. Journal of Alloys and Compounds 753, 241-255. https://doi.org/10.1016/j.jallcom.2018.04.158

[32] Vilaro, T., Colin, C., Bartout, J. D., (2011). As-Fabricated and Heat-Treated Microstructures of the Ti-6Al-4V Alloy Processed by Selective Laser Melting. The Minerals, Metals & Materials Society and ASM International. DOI: 10.1007/s11661-011-0731-y

[33] Zhang, S., Lin, X., Chen, J., Huang, W. (2009). Heat-treated microstructure and mechanical properties of laser solid forming Ti-6Al-4V alloy. Rare Metals 28, https://doi.org/10.1007/s12598-009-0104-5

[34] Brandl, E., Greitemeier, D., (2012). Microstructure of additive layer manufactured Ti–6Al–4V after exceptional post heat treatments. Materials Letters 81, 84-87. https://doi.org/10.1016/j.matlet.2012.04.116

[35] Brandl, E., Schoberth, A., Leyens, C., (2012). Morphology, microstructure, and hardness of titanium (Ti-6Al-4V) blocks deposited by wire-feed additive layer manufacturing (ALM). Materials Science and Engineering: A 532, 295-307. https://doi.org/10.1016/j.msea.2011.10.095

[36] Mur, G. F. X., Rodriguez, D., Planell, J.A. (1996). Influence of tempering temperature and time on the ed-Ti-6Al-4V martensite. Journal of Alloys and Compounds 234, 287-289.

[37] Qazi, J. I., Senkov, O. N., Rahim, J., Genc, A., Froes, F. H. (2001). Phase transformations in Ti6Al4V- x H alloys. Metallurgical and Materials Transactions A 32(10), 2453-2463.

[38] Boyer, R., Welsch, G., Collings, E. W. (1994) *Materials Properties Handbook: Titanium Alloys*, ASM International.

[39] Vrancken, B., et al. (2012). Heat treatment of Ti6Al4V produced by Selective Laser Melting: Microstructure and mechanical properties. Journal of Alloys and Compounds 541, 177-185. http://dx.doi.org/10.1016/j.jallcom.2012.07.022

[40] Saunders, N., Guo, U.K.Z., Li, X. et al. (2003) Using JMatPro to model materials properties and behavior. JOM 55, 60–65. https://doi.org/10.1007/s11837-003-0013-2

[41] Saunders, N., et al. (2003). An Integrated Approach To The Calculation Of Materials Properties For Ti-Alloys. Ti-2003: Proc 10th World Conference.

[42] Andersson, J.O., Helander, T., Höglund, L., Shi, P.F., Sundman, B., (2002). Thermo-Calc and DICTRA, Computational tools for materials science. Calphad 26, 273-312.

[43] ASTM International. (2016). E92-16: Standard Test Methods for Vickers Hardness and Knoop Hardness of Metallic Materials. West Conshohocken, PA: American Society for Testing and Materials.

[44] Collins, P.C. et al. (2009). Development of methods for the quantification of microstructural features in α+β-processed α/β titanium alloys. Material Science and Engineering A 508. 174-182.

[45] ASTM International. (2013). E112-13: Standard Test Methods for Determining Average Grain Size. West Conshohocken, PA: American Society for Testing and Materials.

8 LIST OF ABBREVIATIONS AND SYMBOLS

AM……Additive Manufacturing
BCC……Body-Centred Cubic
CAD……Computer-Aided Design
CCT……Continuous Cooling Transformation
CH……...Cold Hearth Melting
CM……...Conventional Manufacturing
CP……....Commercially Pure
CR……....Cooling Rate
DED……....Directed Energy Deposition
EBM……....Electron Beam Melting
EDS……...Energy Dispersive X-Ray Spectroscopy
El. %……....Percentage Elongation
HAZ……....Heat Affected Zone
HCP……....Hexagonal Closed Packed
HIP……Hot Isostatic Pressing
HT……..…..Heat Treatment
JMA……..…Johnson-Mehl-Avrami
LBM……....Laser Beam Melting
LMD……...Laser Metal Deposition
LMD-p……....Laser Metal Deposition-powder
LoF……..……Lack Of Fusion
LOM……..…..Light Optical Microscope
Mf……..……....Martensite Finish
$MgCl_2$……..…….Magnesium Chloride
MRO……..…..Maintenance, Repair and Overhaul
Ms……..…..Martensite Start
OEM……..…….Original Equipment Manufacturer
PBF……..……....Powder Bed Fusion
SEM……..……...Scanning Electron Microscope
SLM……..……...Selective Laser Melting
TC……..……Thermocouple
Ti……...……..Titanium
Ti3Al……..……Titanium Aluminide
Ti64……..…...Ti-6Al-4V
$TiCl_4$……..……..Titanium Chloride
TiO_2……..……..Titanium Oxide
TTT……..……...Time Temperature Transformation
UTS……..……...Ultimate Tensile Strength
VAR……..……..Vacuum Arc Remelt
YS……..……Yield Strength
α……Alpha
α'……....Alpha Prime
α_m……..Massive Alpha
β……Beta

9 LIST OF FIGURES

Figure 1. Schematic representation of the roles of critical entities in the aerospace industry and the typical interactions between them [1] 9

Figure 2. Schematic of a Turbofan engine [5]. 10

Figure 3. Publication trends related to AM in aerospace industry [1] 11

Figure 4. Schematic plot of specific strength as a function of service temperature for titanium, nickel, steel and aluminium alloys. Adapted from [10]. 12

Figure 5. Schematic crystal structure of titanium (a) α-phase and (b) β-phase [11] 14

Figure 6. Schematic phase diagrams of titanium alloys showing the effect of different alloying elements. [11] 15

Figure 7. Titanium alloy classification based on a β isomorphous phase diagram [11] 16

Figure 8. Thermomechanical processing route for obtaining equiaxed microstructures in Ti-6Al-4V [11] 20

Figure 9. The classification of AM techniques according to ISO 17296e2:2015 [n18] 21

Figure 10. Schematic of the LMD-p processing of Ti64 [20] 22

Figure 11. (a) Gas porosity seen under SEM; (b) Lack of Fusion seen under LOM [21] 23

Figure 12. Schematic representation of the thermal history during LMD of Ti-6Al-4V [20] 24

Figure 13. Schematic cross-section of an as-deposited layer during LMD of Ti-6Al-4V, showing the Heat Affected Zone (HAZ) and regions of Columnar Grains (CG) and Equiaxed Grains (EG). Adapted from [25] 25

Figure 14. Schematic of phase transformations during cooling at different rates from super-transus temperatures [23] 28

Figure 15. Schematic representation of the CALPHAD method used by ThermoCalc [42] 30

Figure 16. Thermal profile set in ThermoCalc's DICTRA module for α-phase fraction simulations from heat treatment temperature of 1000ºC at a cooling rate of X. 32

Figure 17. Schematic LMD-p Ti-6Al-4V samples with dimensions of (a) small sample and (b) big sample. The top shaded region of each sample indicates the build region and bottom unshaded region is the substrate. 32

Figure 18. Schematic of local heat treatment setup. 33

Figure 19. Schematic representation of the β-solutionizing heat treatment. 35

Figure 20. Schematic of the cutting and mounting of samples. Red lines in (a) indicate the cutting lines. In the mount (b), L and T indicate the Longitudinal and Transverse profiles respectively. 36

Figure 21. (a) and (b): LOM imaging methodology for overall microstructure analysis of etched samples. (c): α-case measurement. 37

Figure 22. Images of (a) gas porosity as seen under SEM, (b) LoF pore seen under LOM and (c) α-case seen under SEM. 38

Figure 23. EDS analysis showing presence of Ti and allowing elements (BOTTOM: from left to right) Al, V, O, Si and Fe and the inspected regions of α, massive α (α_m) and β in the SEM image of sample (TOP). 38

Figure 24. Microvickers (300g load) hardness measurement method of (a) longitudinal profile and (b) transverse profile.. 39

Figure 25. Example of the image processing feature in MIPAR. The input (a) SEM image of 3kX mag. and (b) the processed image by MIPAR. In (2): the black region is the α-phase and white region is the β-phase. 39

Figure 26. Example of β grain size measurement by ASTM E112-13 standard in NIS Elements AR. Green lines indicate the lines for measuring the intercepts, with the length of each line on one end and the number of intercepts on the other. 41

Figure 27. Step temperature plot from JMatPro showing the wt. % of phases formed as a function of heat treatment temperature from 1000ºC during equilibrium cooling. 42

Figure 28. (a) TTT diagram and (b) CCT diagram from JMatPro for grain size 200μm and start temperature 1000ºC. 43

Figure 29. JMatPro simulation results showing the influence of cooling rates on α-phase fraction from heat treatment temperature of 1000ºC. 43

Figure 30. One axis equilibrium plot from ThermoCalc showing the amount of phases (in mol.) formed as a function of heat treatment temperature from 1000ºC during equilibrium cooling. BCC_B2 is the β-phase and HCP_A3 is the α-phase. 45

Figure 31. ThermoCalc simulation results showing the influence of cooling rates on α-phase fraction during cooling from heat treatment temperature of 1000ºC. 45

Figure 32. Comparison plot for JMatPro (dashed lines) and ThermoCalc (solid lines) simulation results showing the influence of cooling rates on α-phase fraction during cooling from heat treatment temperature of 1000ºC. Ms indicates the α' start temperature from JMatPro shown by the small black dotted line. 46

Figure 33. LOM images of the as-built microstructure showing (a) the whole sample with elongated β grains in the build in 50X mag., (b) α' in the build (c) in the substrate and (d) equiaxed α+β in the substrate. Red boxes are indicative of regions only, enlarged images are not to their scale. 48

Figure 34. SEM images of the as-built microstructure showing (a) α' and (b) α+β basketweave morphology in the build, and (c) equiaxed α+β in the substrate. In (a), the white needles indicate α'. In (b) and (c), dark regions are α, bright regions are β. 48

Figure 35. Influence of varying cooling rates on β grain size in the build of samples heat-treated for 30 min. Black dotted line shows the as-built β grain size value. 51

Figure 36. Influence of varying cooling rates on β grain size in the build of samples heat-treated for 75 min. Black dotted line shows the as-built β grain size value. 51

Figure 37. LOM images of the build in samples heat-treated at T3 for 75 min and cooled at rates of (a) A and (b) D. Bright regions are α and dark regions are β. Thickness of the bright laths indicates the α-lath thickness. 52

Figure 38. SEM images of the build in samples heat-treated at T3 for 75 min and cooled at rates of (a) A and (b) D. Dark regions are α and bright regions are β. Thickness of the dark laths indicates the α-lath thickness. 52

Figure 39. Influence of varying cooling rates on build hardness in the longitudinal direction in samples heat-treated for 30 min. Black dotted line indicates the average as-built build hardness. 53

Figure 40. Influence of varying cooling rates on build hardness in the longitudinal direction in samples heat-treated for 75 min. Black dotted line indicates the average as-built build hardness 53

Figure 41. Influence of varying cooling rates on α-lath thickness in the build of samples heat-treated for 30 min 54

Figure 42. Influence of varying cooling rates on α-lath thickness in the build of samples heat-treated for 75 min 55

Figure 43. Influence of varying cooling rates on α and β phase fractions in the build of samples heat-treated for 30min. Solid lines indicate α-phase fraction and dashed lines indicate β-phase fraction 56

Figure 44. Influence of varying cooling rates on α and β phase fractions in the build of samples heat-treated for 75min. Solid lines indicate α-phase fraction and dashed lines indicate β-phase fraction 57

Figure 45. LOM image of the transverse profile of a β-solutionized sample showing the penetrated α-case layer into the build 58

Figure 46. α-case penetration study showing the hardness measurements at different depths. Vertical lines are guidelines for the exact penetrated depth of α-case. 58

Figure 47. Microstructure of β-solutionized sample in the longitudinal profile: (a) LOM stitched image of build and substrate, (b) LOM image of build and (c) SEM image of build. Red box is indicative of region only, enlarged image is not to its scale. 60

Figure 48. Influence of varying cooling rates on β grain size in the build of samples β-solutionized and heat-treated at T2 and T4 for 30 min (dashed lines) compared with those without prior β-solutionizing (solid lines). Purple dashed line indicates the solutionized β grain size. Black dotted line indicates the as-built β grain size. 61

Figure 49. LOM images of β-solutionized sample heat-treated at T4 for 30 min and air-cooled, showing (a) stitched image of the entire build and (b) a zoomed-in region in the build. Red box is indicative of region only, enlarged image is not to its scale. 61

Figure 50. LOM images of β-solutionized sample heat-treated at T4 for 30 min and cooled at A, showing (a) stitched image of the entire build and (b) a zoomed-in region in the build. Red box is indicative of region only, enlarged image is not to its scale. 62

Figure 51. LOM images of β-solutionized sample heat-treated at T2 for 30 min and air-cooled, showing (a) stitched image of the entire build and (b) a zoomed-in region in the build. Red box is indicative of region only, enlarged image is not to its scale. 63

Figure 52. LOM images of β-solutionized sample heat-treated at T2 for 30 min and cooled at A, showing (a) stitched image of the entire build and (b) a zoomed-in region in the build. Red box is indicative of region only, enlarged image is not to its scale. 63

Figure 53. Influence of varying cooling rates on build hardness of samples β-solutionized and heat-treated at T2 and T4 for 30 min (dashed lines) compared with those without prior β-solutionizing (solid lines). Purple dashed line indicates the average build hardness of solutionized sample. Black dotted line indicates average build hardness of as-built sample. 65

Figure 54. Influence of varying cooling rates on α-lath thickness of samples β-solutionized and heat-treated at T2 and T4 for 30 min (dashed lines) compared with those without prior β-solutionizing (solid lines). 65

Figure 55. Influence of varying cooling rates on α-phase fraction of samples β-solutionized and heat-treated at T2 and T4 for 30 min (dashed lines) compared with those without prior β-solutionizing (solid lines). 66

Figure 56. Comparison plot for JMatPro and ThermoCalc simulation results showing the influence of cooling rates on α-phase fraction during cooling with the black dotted box marking the region which is experimentally relevant and comparable. 67

Figure 57. 2D surface plots for simulation results (top two) and experimental results (bottom two) showing the influence of cooling rates on α-phase fraction during cooling at different rates. 69

10 LIST OF TABLES

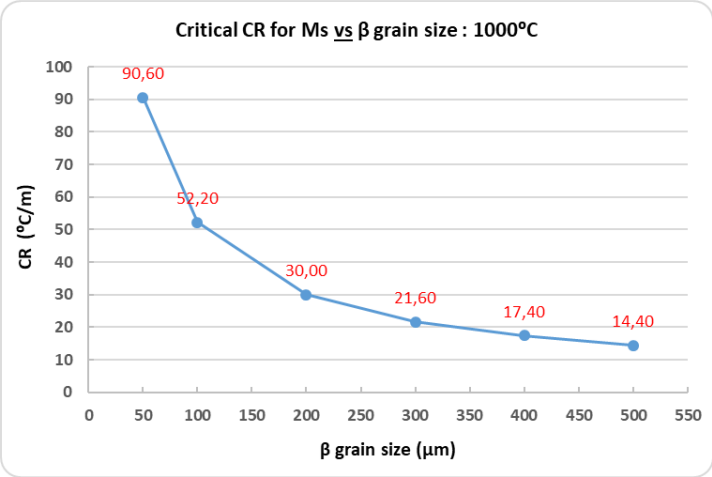
Table 1. Chemical composition of Ti-6Al-4V [13] 16
Table 2. Phases of Ti-6Al-4V and the reasons behind their formation. 17
Table 3. Typical Ti-6Al-4V microstructure morphologies, reasons behind their formation and their features. Adapted from [15] 17
Table 4. Tensile properties of Ti-6Al-4V manufactured by AM and CM techniques. Adapted from [26]. 26
Table 5. Heat treatment cycles with schematics 34
Table 6. Grinding and polishing steps. 36
Table 7. Gas porosities found in all experimental samples 47
Table 8. Hardness (in HV0.3) of as-built sample in longitudinal and transverse profile 49
Table 9. Chemical composition of experimental sample from EDS analysis. 50

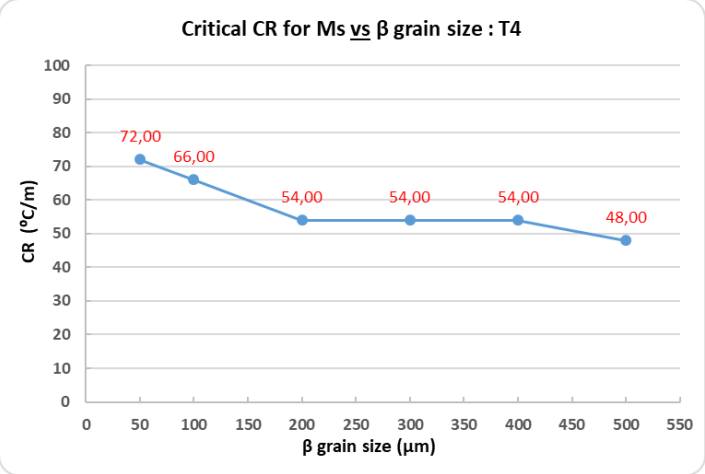
11 LIST OF APPENDICES

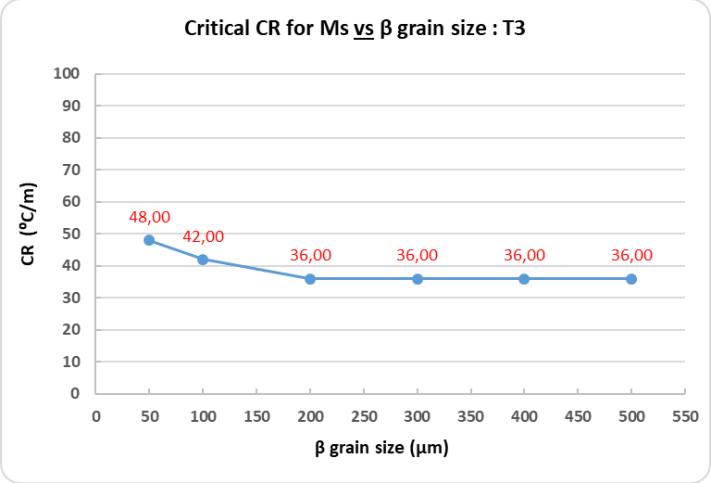
APPENDIX A: Plots of critical cooling rates for α' formation from JMatPro simulations 81
APPENDIX B: Plots of Ms and Mf temperatures based on β grain size from JMatPro simulations 82

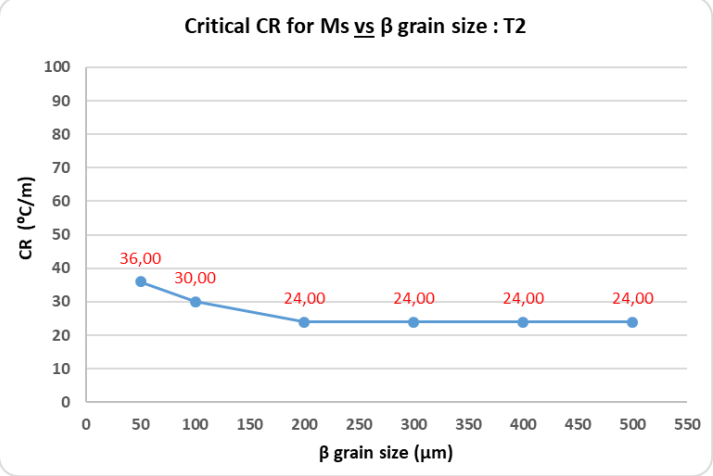
APPENDIX A

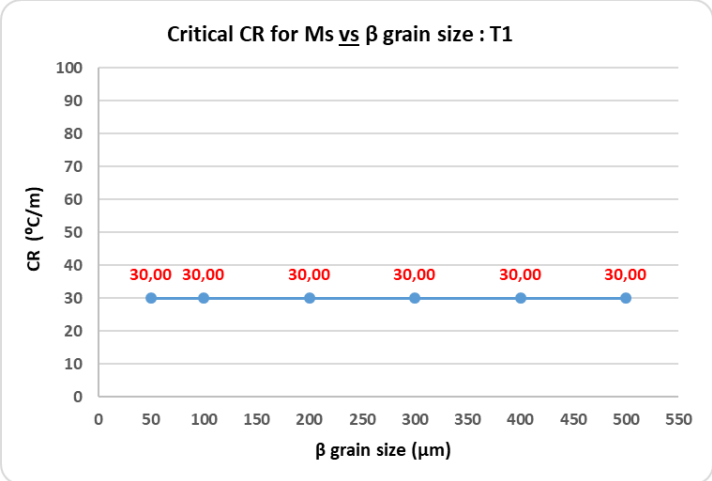
Appendix A: Plots of critical cooling rates for α' formation from JMatPro simulations











APPENDIX B

Appendix B: Plots of Ms and Mf temperatures based on β grain size from JMatPro simulations

